NTNU

Norwegian University of
Science and Technology

Pitting Corrosion of Super Duplex Stainless Steel

Effect of Isothermal Heat Treament

Christian Rene Lauritsen

Chemical Engineering and Biotechnology
Submission date: June 2016
Supervisor: Ida Westermann, IMTE
Co-supervisor: Roy Johnsen, IPM

Norwegian University of Science and Technology
Department of Materials Science and Engineering

NTNU
Norwegian University of
Science and Technology

Pitting Corrosion of Super Duplex Stainless Steel
Effect of Isothermal Heat Treatment

Christian Lauritsen

TMT4900 Materials Chemistry and Energy Technology, Master's Thesis
Supervisor: Professor Roy Johnsen
Co-supervisor: Professor Ida Westermann
Spring 2016

Norwegian University of Science and Technology
Department of Materials Science and Engineering

Preface

This thesis has been written in the course TMT4900 Materials Chemistry and Energy Technology, Master's thesis at the Department of Materials Science and Engineering at NTNU. Professor Ida Westermann and Professor Roy Johnsen have supervised the work. In addition, this work has been in collaboration with Mariano Iannuzzi in GE Oil and Gas. The experimental work has been performed at the SINTEF and NTNU Corrosion Laboratory.

I would thank both my supervisors, Ida Westermann and Roy Johnsen, for good guidance during this project. A special thanks goes to Roy Johnsen for always being available. I would also thank Cristian Torres for help with the experimental work.

Further, I would like to thank Marte Mrkve for her help throughout the semester.

Abstract

The objective with this work was to investigate the effect of isothermal heat treatment on the pitting corrosion properties of a super duplex stainless steel containing more than 2 wt% tungsten, called UNS S39274. The effect of σ - phase, χ - phase, secondary austenite and chromium nitrides were emphasized.

Two electrochemical measurements were performed in this work, a modified method of the ASTM G48 standard and ASTM G61 anodic cyclic potentiodynamic polarization (CPP). Prior to electrochemical measurements, the samples were heat treated. The solution annealing was performed 1110°C for 15 minutes, and the isothermal heat treatment temperatures used in this work were 820°C, 870°C and 940°C. The modified ASTM G48 standard method was used to determine the critical pitting temperature (CPT) by open circuit potential (OCP) and temperature measurements in a 6 wt% ferric chloride electrolyte. Anodic CPP curves were recorded to obtain the parameters OCP, critical pitting potential (E_p), repassivation potential (ERP) and passive current density (i_p), at three electrolyte temperatures, 40°C, 60°C and 80°C. The anodic CPP was recorded in a 3,56 wt% sodium chloride electrolyte. After electrochemical measurements, some samples were surface characterized by optical microscope (OM), 3D OM and scanning electron microscope (SEM). All tests were performed at the SINTEF and NTNU corrosion laboratory.

The average CPT for solution annealed samples was found to be 77,5°C. For samples isothermal heat treated at 870°C, 820° and 940°C for 4 minutes, the average CPT was reduced by 32,5°C, 22,5°C and 15°C relative to solution annealed condition, respectively. CPT was found to decrease with increasing isothermal heat treatment time at a given heat treatment temperature. The critical heat treatment time was observed to be between 2 and 4 minutes, based on a significant reduction in CPT as a function of isothermal heating time (IHt). E_p was generally decreased with increasing isothermal heat treatment time at a given isothermal heat treatment temperature, and was also generally decreased with increasing electrolyte temperature. Values of E_p also indicated that the critical heat treatment time was between 2 to 4 minutes, which was in accordance with the results from CPT measurements.

The solution annealed samples contained no intermetallic precipitates and secondary phases, and the pitting corrosion was mainly initiated and propagated inside grains. For isothermal heat treated samples, the pitting corrosion was found to mainly initiate and propagate along grain boundaries. The number of pits observed on the sample surface increased with increased isothermal heat treatment time. Selective dissolution of ferrite was observed on some samples

without pitting corrosion after anodic CPP.

Sammendrag

Formlet med denne oppgaven var underske effekten av isoterm varmebehandling p gropkorrosjonsegenskapene til super dupleks rustfritt stl, som inneholder mer enn 2 vekt% wolfram, UNS S39274. Effekten av σ fase, χ fase, γ_2 og kromnitrider ble fokusert p.

To elektrokjemiske mlinger ble utfrt i dette arbeidet, en mofifisert metode av ASTM G48 standard of ASTM G61 anodic syklisk potensiodynamisk polarisasjon (CPP). Fr elektrokjemiske mlinger, ble prvene varmebehandlet. Lsningsherding ble utfrt ble utfrt ved 1110°C i 15 minutter, og isoterme varmebehandlingstemperaturer brukt i dette arbeidet var 820°C, 870°C og 940^{circ}C. Den mofiserte ASTM G48 standard metoden ble brukt til bestemme den kritiske groporrosjonstemperaturen (CPT) ved mle pen krets potensial (OCP) og temperatur i en 6 vekt% jernkloridlsning. Anodiske CPP kurver ble tatt opp for bestemme parameterene OCP, kritisk groporrosjonspotensial (E_p) og repassiveringspotensial (E_{RP}, ved tre elektrolytt temperaturer 40°C, 60°C og 80°C. Anodiske CPP kurver ble tatt opp i en 3,56 vekt% natriumklorid elektrolytt. Etter elektrokjemiske mlinger, ble noen prver overflatekarakterisert ved optisk mikroskopi (OM), 3D OM og scanning elektronmikroskop (SEM). Alle testene ble utfrt p SINTEF og NTNU korrosjonslaboratorium.

Gjennomsnittsverdien av CPT for lsningsherdet prver ble funnet til vre 77,5°C. For prver som ble isotermt varmebehandlet ved 870°C, 820°C og 940°C i 4 minutt, ble gjennomsnittsverdien av CPT redusert med henholdsvis 32,5°C, 22,5°C og 15°C i forhold til lsningsherdet tilstand. CPT ble funnet til avta med kende isoterm varmebehandlingstid for en gitt varmebehandlingstemperatur. Den kritiske varmebehandlingstiden ble observert til vre mellom 2 og 4 minutter, basert p en betydelig reduksjon i CPT som funskjon av isoterm varmebehandlingstid (IHt). E_p ble generelt redusert med kende isoterm varmebehandlingstid, og ogs ved kende elektrolytt temperatur. Verdier for E_p viste ogs at den krisitke varmebehandlingstiden var mellom 2 og 4 minutter, som er i samsvar med resultatet fra CPT mlingene.

Selektiv opplsning av ferritt ble observert p prveoverflater uten gropkorrosjon etter anodisk CPP. Prver som var lsningsherdet inneholdt ingen intermetalliske utfeller og sekundre faser, og gropkorrosjon ble hovedsakelig initiert og propagert inni kornene i mikrostrukturen. For prver som var isoterm varmebehandlet, ble gropkorrosjon hovedsakelig funnet til intitiere og propagere langs korngrensene. Antall groper observert p prveoverflaten kte med kende isoterm varmebehandlingstid.

Contents

Abbreviations and symbols

	Unit	Explanation
α	-	Iron rich ferrite
α'	-	Chromium rich ferrite
A	cm^2	Area
APF	-	Atomic packing factor
b	mm	Width
BCC	-	Body centered cubic
BCT	-	Body centered tetragonal
BSE	-	Backscattered electron
CPP	-	Cyclic potentiodynamic polarization
CPT	°C	Critical pitting temperature
d	nm	Grain size
DSS	-	Duplex stainless steels
E_{corr}	V	Corrosion potential
E_{Flade}	V	Flade potential
E_p	V	Pitting potential
E_{RP}	V	Repassivation potential
ϵ_f	%	Minimum elongation to failure
EBSD	-	Electron backscattered diffraction
EDS	-	Energy dispersive spectroscopy
FCC	-	Face centered cubic
FZ	-	Fusion zone
HAZ	-	Heat affected zone
i	$\frac{A}{cm^2}$	Current density
i_{corr}	$\frac{A}{cm^2}$	Corrosion current density
i_p	$\frac{A}{cm^2}$	Anodic passive current density
i_{red}	$\frac{A}{cm^2}$	Reduction current density
I	A	Current
IPM	-	Department of engineering design and materials

	Unit	Explanation
IHt	min	Isothermal heating time
IHT	°C	Isothermal heating temperature
N(t)	-	Number of nuclei per unit volume as a function of time
OCP	V	Open circuit potential
OM	-	Optical microscope
PREN	-	Pitting resistance equivalent number
$PREN_W$	-	Pitting resistance equivalent number including tungsten
r(t)	nm	Radius of a sphere as a function of time
R_M	MPa	Tensile strength
$R_{p0,2}$	MPa	Yield strength
SCE	-	Standard calomel electrode
SCC	-	Stress corrosion cracking
SDSS	-	Super duplex stainless steels
SEM	-	Scanning electron microscope
t	min	Time
T	°C	Temperature
TTT	-	Temperature - time - transformation
σ	-	Sigma - phase
σ_y	MPa	Yield strength
σ_0	MPa	Yield strength for a one - crystal
γ	-	Austenite
γ_2	-	Secondary Austenite
χ	-	χ - phase
X_e	-	Volume fraction of σ - phase

Chapter 1

Introduction

1.1 Background

Duplex stainless steels (DSS) and super duplex stainless steels (SDSS) with chromium contents of 22 and 25 wt% respectively, are widely used in the industry. The duplex microstructure consists of ferrite and austenite, which gives a combination of high strength and high corrosion resistance in both oxidizing and reducing environments [1]. When comparing DSS and SDSS with low alloyed austenitic stainless steels, several advantages are apparent, for instance higher mechanical strength, superior resistance against corrosion and a lower price due to a lower nickel content [1, 2].

A combination of high corrosion resistance and mechanical properties in the temperature range of -50 to 250°C is offered by DSS and SDSS. Outside this temperature range, austenitic stainless steels are more suitable, due to the brittle behaviour of ferrite [2]. The performance of materials, including SDSS, is highly affected by the alloying elements, microstructure and fabrication processes. Due to this, it is important to control processing parameters that affect the microstructure during manufacturing of DSS and SDSS. This may for instance be heat treatments or welding procedures.

DSS and SDSS are prone to formation of intermetallic precipitates and secondary phases during isothermal heat treatment [2]. Detrimental phases, such as σ - phase, the χ - phase, secondary austenite (γ_2) and chromium nitrides can form in the temperature range of 700 - 950°C. These phases can form during welding or due to improper heat treatment, and affect localized corrosion resistance and mechanical properties of SDSS [3]. To assure safe use of DSS and SDSS in the industry, it is important to quantify the precipitation kinetics of these phases, and to understand the effect on corrosion properties of DSS and SDSS.

1.2 Aim of work

In this work, the pitting corrosion properties of a super duplex stainless steel containing more than 2 wt% tungsten, UNS S39274 will be investigated based on available literature and results from experimental work. The evaluation of experimental results will include critical pitting temperature (CPT), critical pitting potential (E_p) and properties of corroded surfaces. This will be performed by a modified ASTM G48 method, ASTM G61 anodic cyclic potentiodynamic polarization (CPP) and surface characterization.

The main objective with this work is to understand the effect of isothermal heat treatment on pitting corrosion properties of UNS S39274. The work will especially focus on the effect of σ - phase, χ - phase, γ_2 and chromium nitrides on the corrosion properties of UNS S39274. The volume fraction of these will not performed in this work.

Chapter 2

Theory

2.1 Super duplex stainless steels

Stainless steels are iron alloys containing a minimum of approximately 11% chromium [1]. Chromium is added to prevent corrosion, by forming a very thin stable oxide film on the surface. Chromium favours the formation of ferrite (α) and is an α stabilizer. Nickel is another alloying element in stainless steels, which favours the formation of austenite (γ) and is a γ stabilizer [1]. Stainless steels can be divided into austenitic steels with a face centered cubic (FCC) crystal structure, ferritic steels with a body centered cubic (BCC) crystal structure and martensitic steels with a body centered tetragonal (BCT) crystal structure [1]. Between the α - and γ - phase in phase diagrams of stainless steels there is a $(\alpha + \gamma)$ - region which can be used to obtain two - phase or duplex structures in stainless steels, giving duplex stainless steels (DSS) or super duplex stainless steels (SDSS).

2.1.1 Microstructure

DSS are chromium - nickel - molybdenum alloys that are balanced to contain a mixture of austenite and ferrite [4]. The duplex microstructure in stainless steels can be produced by a correct balance between the α - and γ - forming elements [1]. Chromium, molybdenum, titanium and silicon are often used as α - forming elements, while nickel, manganese, carbon and nitrogen are often used as γ - forming elements. The volume fraction of each phase in DSS depends on the chemical composition and heat treatment [5]. The ferrite content can vary between 35 and 55 %, but manufacturers balance the steels close to the ideal 50 - 50 % ferrite/austenite ratio [6]. A typical duplex microstructure is shown in Figure 2.1.

DSS can be defined as ferritic/austenitic stainless steels containing minimum 22 wt% chromium, with similar corrosion resistance as austenitic stainless steels containing equal amounts of chromium [6]. SDSS are high alloyed versions of DSS and are defined not only based on the chromium content, but also on the pitting resistance equivalent number (PREN) [7]. According to this, SDSS are defined as ferritic/austenitic stainless steels with minimum 25 wt%

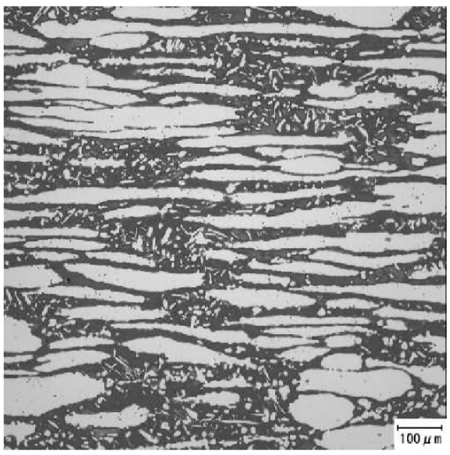

Figure 2.1: A typical duplex microstructure showing the austenite and the ferrite phase, from the material data sheet of UNS S39274 in Appendix A. The dark phase is ferrite and the bright phase is ferrite.

chromium and a PREN equal or larger than 40 [8]. Pitting corrosion and PREN will be further described in Section 2.6. Some common SDSS, with names and chemical compositions, are given in Table 2.1 [6, 7].

Table 2.1: Chemical compositions of some common SDSS [6, 7].

UNS	**wt% Cr**	**wt% Ni**	**wt% Mo**
UNS S32550	25	5,5	3,5
UNS S32750	25	7	3,5
UNS S32760	25	7	3,5
UNS S39274	25	6,5	3,5

The effect of nickel on the austenite area in iron - chromium - nickel alloys is illustrated in the phase diagram for a 24 % chromium stainless steel, shown in Figure 2.2 [9]. The $\alpha + \gamma$ area of the phase diagram can be used to obtain DSS and SDSS.

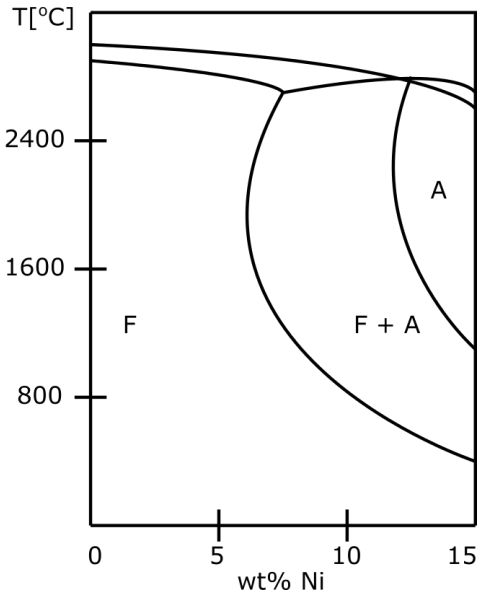

Figure 2.2: Effect of nickel on the austenite area of iron - chromium - nickel alloys. In SDSS the phase diagram will also be affected by other alloying elements, but this phase diagram shows the effect of austenite stabilizers and ferrite stabilizers together in a stainless steel [9]. The $\alpha + \gamma$ (represented by F and A, respectively) area can be used to obtain DSS and SDSS.

2.1.2 Mechanical properties

SDSS are stronger than several autenitic steels as a result of the two - phase structure and the refinement of the grain size [1]. Ferrite is the major source of strengthening, while austenite provide ductility and toughness [5]. By thermomechanical treatment between 900 and 1000 °C, it is possible to obtain fine microduplex structures. The microduplex structures can exhibit high ductilities at high temperatures for strain rates less than a critical value [1]. The duplex structure increases the toughness and ductility of stainless steels, compared with ferritic stainless steels. SDSS have improved stress corrosion cracking (SCC) resistance compared to some low alloyed austenitic stainless steels (for instance AISI 304 and AISI 316), due to the ferrite phase in the duplex structure [9].

The yield strength of SDSS can be in the range of 550 to 690 MPa, and can be twice as high as for austenitic stainless steels [4, 9]. One of the reasons for the high strength of SDSS is solid solution strengthening. If the solute and the solvent atoms are roughly similar in size, the solute atoms will occupy lattice points in the crystal lattice of the solvent atoms [10, 11]. This is called substitutional solid solution. If the solute atoms are significantly smaller than the solvent atoms, they will occupy interstitial positions in the solvent atoms lattice [10, 11]. This is called interstitial solid solution. SDSS contain both of these solid solution strengthening mechanisms, where chromium and nickel are examples of atoms that form substitutional solid solution, and nitrogen is an example of an atom that forms interstitial solid solution. Since ferrite has a BCC crystal structure, which is less close packed than a FCC crystal structure, it dissolves more interstitial atoms than austenite, having a FCC crystal structure. The crystal structures of ferrite, austenite and some alloying elements in SDSS are given in Table 2.2,

with the fraction of solid sphere volume in a unit cell (the atomic packing factor (APF)).

Table 2.2: Crystal structure and atomic packing factor (APF) for α - and γ - iron and some alloying elements in SDSS [11].

Iron	**Crystal structure**	**APF**
Ferrite (α - iron)	BCC	0,68
Chromium	BCC	0,68
Molybdenum	BCC	0,68
Tungsten	BCC	0,68
Austenite (γ - iron)	FCC	0,74
Nickel	FCC	0,74

The reduction in grain size from the duplex structure also affects the yield strength of SDSS, and depends on processing and heat treatments of the steel. Adjacent grains can have different crystallographic orientations. During plastic deformation, slip or dislocation motion must take place across this common boundary [11]. A fine grained material is harder and stronger than a coarse grained material, because the former has a greater total grain boundary area to impede dislocation motion. The yield strength, σ_y, varies with the grain size according to Equation 2.1 [11]:

$$\sigma_y = \sigma_0 + k_y d^{-1/2} \tag{2.1}$$

where σ_0 is the yield strength for a one - crystal, d is the grain size and k_y is a constant. This expression is called the Hall - Petch equation.

The mechanical properties of DSS containing 22 wt% chromium and SDSS containing 25 wt% chromium, are compared to the mechanical properties of one austenitic stainless steel and one nickel alloy in Table 2.3. This illustrates the advantages of SDSS compared to other commonly used alloys in the oil and gas industry [6].

Table 2.3: Mechanical properties of DSS and SDSS compared to an austenitic stainless steel (UNS S31603) and a nickel alloy (UNS N06625), to illustrate some advantages of SDSS [6]. σ_y, R_M and ϵ_f are yield strength, tensile strength and minimum elongation to failure, respectively.

Property	**DSS**	**SDSS**	**UNS S31603**	**UNS N06625**
σ_y [MPa]	450	550	205	415
R_M [MPa]	620	750	515	825
ϵ_f [%]	25	25	35	30

The mechanical properties of SDSS are highly affected by the heat treatment and aging temperature. Precipitation of intermetallic compounds in small volume fractions in ferrite leads to a reduction in toughness [5]. The different intermetallic precipitates and secondary phases, and their effect on corrosion and mechanical properties will be further described in Section 2.2.

2.1.3 Effect of alloying elements in SDSS

The major alloying elements in DSS and SDSS are chromium, nickel, molybdenum, manganese, nitrogen, copper and tungsten. One of the most convenient ways of representing the effect of various elements on the microstructure of chromium - nickel stainless steels is the Schaeffler diagram, given in Figure 2.3 [1]. The Schaeffler diagram can be used to predict solidification modes and structures obtained during welding, based on nickel and chromium equivalents and alloying compositions [5].

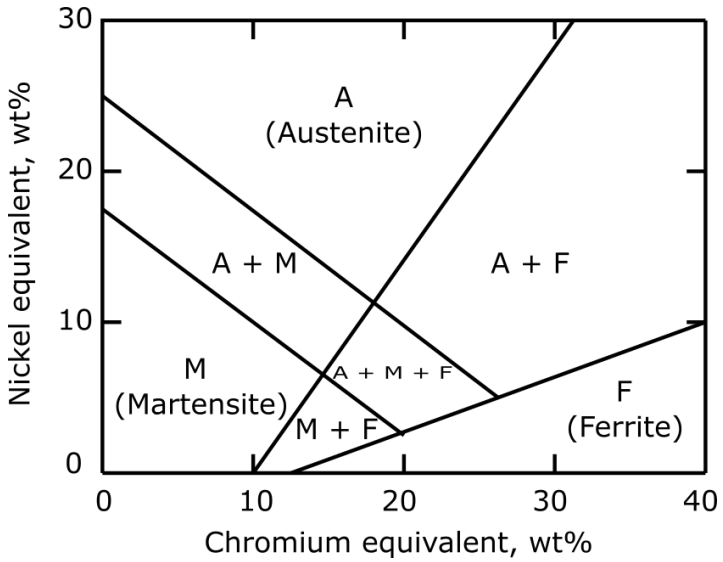

Figure 2.3: Schaeffler diagram, which gives the effect of alloying elements on the structure of chromium - nickel stainless steels [1]. F, A and M represent ferrite, austenite and martensite, respectively.

Ferrite stabilizers contract the γ - field in the phase diagram and encourages the formation of ferrite over wider compositional limits, while austenite stabilizers expand the γ - field and encourages the formation of austenite over wider compositional limits [1]. The relative strength of the alloying elements, as ferrite and austenite formers, are shown in Figure 2.4 [1]. The alloying elements affect SDSS in several ways and some of this elements are further described below.

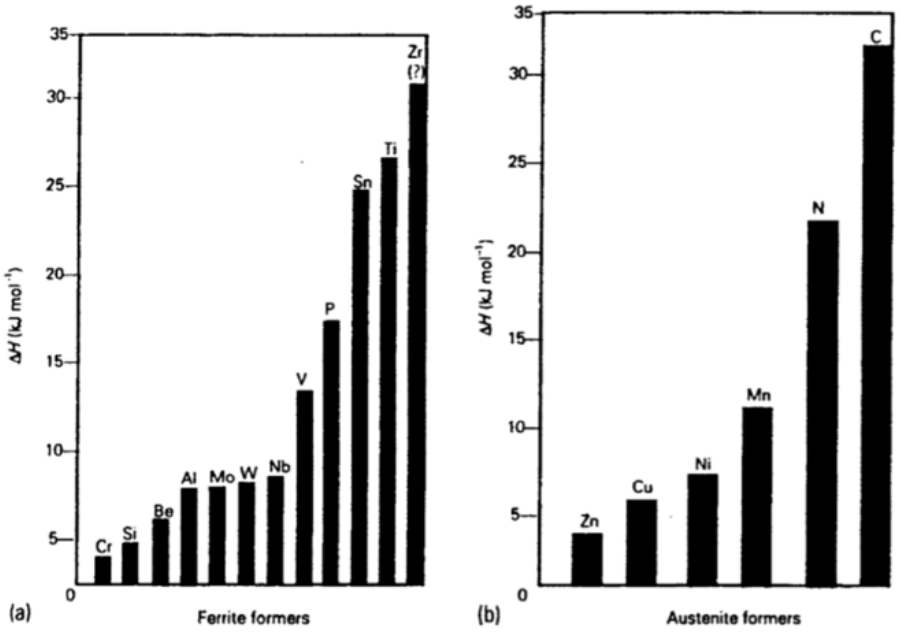

Figure 2.4: Relative strength of alloying elements as ferrite and austenite stabilizers [1].

Ferrite stabilizers

Chromium

Chromium is a α stabilizer and forms a protective oxide film, which improves corrosion resistance of SDSS. The amount of chromium should be controlled and has a maximum limit due to the formation of detrimental intermetallic precipitates if the content is too high [3]. Chromium also increases the pitting corrosion resistance of SDSS [12]. Since chromium promotes the formation of the embrittling sigma (σ) - phase, the amount is usually kept in the range 22 - 26% in stainless steels [13]. The chromium equivalent, used in the Schaeffler diagram in Figure 2.3, is given by Equation 2.2 [1]:

$$\%Cr\ \ equivalent = \%Cr + 2 \cdot \%Si + 1,5 \cdot \%Mo + 5 \cdot \%V + 5,5 \cdot \%Al + 1,75 \cdot \%Nb + 1,5 \cdot \%Ti + 0,75 \cdot \%W \tag{2.2}$$

where the concentration of elements are given in wt%.

Molybdenum

Molybdenum increases the corrosion resistance of SDSS, as for instance against pitting and crevice corrosion. Molybdenum forms oxy - hydroxide layers, which stabilizes the oxide film. This leads to slower degradation and protection against corrosion [9]. Molybdenum is 3,3 times more effective than chromium against pitting corrosion resistance in SDSS [14]. Molybdenum improves the resistance of stainless steels in several mediums, particularly in nonoxidizing acids [13]. In combination with nickel, molybdenum gives acid resistant stainless steels, which are resistant to corrosion in sulfuric acid and salt water.

High contents of molybdenum may, due to its high diffusion rate in ferrite, form secondary phases, such as σ - and chi (χ) - phase, during exposure to elevated temperatures between 400 and 1000 °C [15]. Molybdenum is also known to increase the range of stability of the σ - phase towards higher and lower temperatures [2, 13]. Studies have shown that molybdenum accelerates the formation of σ - phase and shifts the maximum rate of formation to higher temperatures [13]. The content of molybdenum is limited to 3 or 4 wt% in SDSS because it is a strong ferrite stabilizer, and because it promotes precipitation of secondary phases [5].

Tungsten
Tungsten gives resistance against pitting corrosion of SDSS. Addition of tungsten in place of molybdenum has been found to suppress formation of σ - phase without reducing the corrosion resistance [16]. The effect of tungsten on pitting corrosion properties of SDSS will be further described in Section 2.6.4.

Austenite stabilizers

Nickel
To obtain austenite in the duplex structure, nickel is added in sufficient amounts, due to the high content of ferrite stabilizers [9]. This element has a beneficial influence on crevice corrosion resistance [5]. The mechanical properties of SDSS are optimized with a ferrite volume fraction of about 50%, which leads to an optimal nickel content of 5 - 8%. Higher amounts of nickel can increase σ - phase formation. Nickel shifts the stability range of the intermetallic σ - phase to lower chromium contents and higher temperatures [13]. The nickel equivalent, used in the Schaeffler diagram in Figure 2.3, is given by Equation 2.3 [1]:

$$\%Ni\ \ equivalent = \%Ni + \%Co + 30 \cdot \%C + 25 \cdot \%N + 0,5 \cdot \%Mn + 0,3 \cdot \%Cu \qquad (2.3)$$

where the concentration of elements are given in wt%.

Manganese
Manganese increases the wear and abrasion resistance of SDSS. It also gives higher tensile strength without loss of ductility [3]. A high amount of manganese leads to a wider temperature range where the intermetallic precipitates and secondary phases can form and increases the rate of formation of them. Formation of MnS can decrease pitting resistance as it can act as an initiation site for formation of pits [3].

Nitrogen
Nitrogen improves the mechanical properties and increases corrosion and wear resistance of SDSS [17]. One possible reason for the increased corrosion resistance is the formation of ammonium beneath the oxide surface film. Ammonium has been found in solutions during corrosion, which results in an increase in pH and increased rate of formation of an oxide film. Nitrogen is a strong austenite former and expands the γ - field of the iron alloy phase diagram [1]. However, the range of expansion is short due to compound formation. Nitrogen gives

interstitial solid solution strengthening and increased resistance against pitting corrosion [10]. A higher content of nitrogen has been found to increase the pitting potential for all pH [17]. Concentrations of nitrogen up to 0,25 wt% can nearly double the proof stress of a Cr - Ni austenitic steel. It has been found that nitrogen contributes significantly to sliding wear and cavitation erosion resistance of stainless steels [18]. In DSS and SDSS nitrogen may, with high contents of chromium and molybdenum, delay the formation of intermetallic precipitates and secondary phases due to their decreasing effect on the activity of chromium [18].

Copper
Copper additions improve corrosion resistance of SDSS in many not oxidizing acids, but the amount is limited to 2 wt% due to a reduction in hot ductility with higher amounts [3]. Higher amounts of copper in SDSS will also lead to formation of epsilon phase, which reduces the pitting resistance [3].

2.2 Heat treatment of SDSS

The optimal microstructure of DSS and SDSS contain approximately equal amounts (50%) of ferrite and austenite, and offer good combinations of mechanical properties and corrosion resistance [6, 19]. This can be obtained by solution annealing at 1050 - 1150°C followed by rapid cooling [20]. The temperature of this solution annealing heat treatment is a parameter that affects the corrosion properties of the steel [20]. SDSS are prone to the formation of intermetallic precipitates and secondary phases, which may form in the temperature range of 300 - 1000 °C, during isothermal aging or incorrect heat treatment [2]. Residence times in the range of 700 - 950 °C should be as short as possible in order to limit the risk of formation of the most undesirable intermetallic precipitates and secondary phases [21]. The resistance against pitting corrosion of the base material can be optimized by selecting diffusion annealing temperatures, which lead to concentrations of alloying elements that gives equal pitting resistance in ferrite and austenite [6]. The recommended annealing temperature is about 1100°C for DSS and SDSS containing molybdenum, since the formation of intermetallic precipitates and secondary phases is possible up to about 1050°C [21]. The situation in a welded part of SDSS is more complex [22]. The balance of alloying elements can be disturbed, either by formation of intermetallic precipitates and Cr_2N, or by excessive precipitation of secondary austenite (γ_2). Redistribution of alloying elements may lead to local reductions in pitting resistance [22]. This can happen either in regions that are depleted with respect to crucial alloying elements or in precipitates.

Pitting corrosion resistance can be improved by additions of chromium, molybdenum and nitrogen [22]. However, these elements may also promote the formation of intermetallic precipitates and secondary phases, which are detrimental for the corrosion resistance. For this reason, there is limitation regarding the amount of alloying elements in SDSS. The mechanical and corrosion performance of SDSS can be degraded by undesired phases, such as extensive precipitation from melting and rapid solidification in fusion welding processes [23].

The annealing temperature affects the structure of each phase and the associated corrosion behavior of SDSS. Research has been done to determine optimal annealing temperatures where SDSS exhibits the best pitting corrosion resistance [24]. The results of the precipitation of different phases in SDSS can be summarized in a temperature - time - transformation (TTT) diagram. A TTT diagram of the SDSS grade UNS S32750 is shown in Figure 2.5, where the most common precipitates in SDSS are illustrated [2].

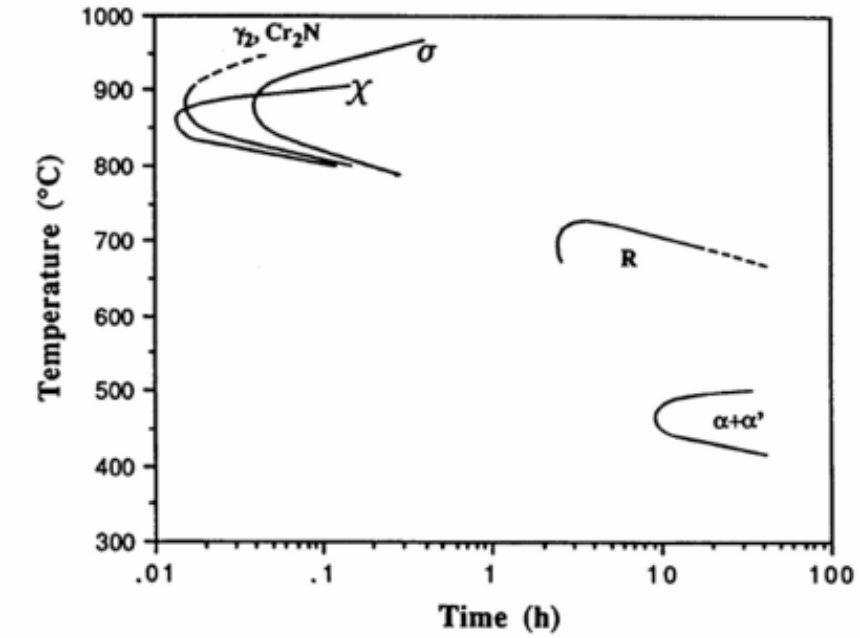

Figure 2.5: TTT diagram of UNS S32750 (SAF 2507), showing the precipitation kinetics of intermetallic precipitates and secondary phases [2].

Intermetallic precipitates and secondary phases, such as the σ - and χ - phase, form in the temperature range of 600 - 1000 °C as a result of too slow cooling. Many of them have an adverse effect on corrosion resistance and toughness, but less or no effect on fatigue properties [18]. In addition, the formation of γ_2, nitrides and carbides takes place in this temperature range. Phase separation of ferrite into regions of chromium - rich α' and iron - rich α can occur in the temperature range of 300 - 500 °C. This phase separation embrittles the ferrite and appears to be due to the decomposition of ferrite [18]. Possible intermetallic precipitates and secondary phases in SDSS are described in the next section.

One heat treatment procedure is welding operations, where some procedures can lead to lower amounts of austenite and precipitations of intermetallic and secondary phases. According to the Norsok M601, a standard for welding and piping inspection, a minimum content of 30% austenite in the last bead and root pass is necessary to accept the weld [25]. To achieve the desired microstructure in SDSS, heat input must be well controlled during welding. The fusion - zone (FZ) and the heat - affected zone (HAZ) can be characterized by an unbalanced ratio between ferrite and austenite, due to high temperatures and high cooling rates during welding [20].

2.2.1 Intermetallic precipitates and secondary phases

σ - phase

The σ - phase consists mainly of iron, chromium and molybdenum, and precipitates in the temperature range of 600 - 1000 °C, but this depends on the chemical composition of the alloy [19, 26]. It has a tetragonal crystal structure and is intermetallic [27]. In the binary iron - chromium system it can form over a wide composition range between 25 and 60 % chromium, as shown in Figure 2.6 [1]. Elements, such as chromium, molybdenum, nickel, silicon and manganese enhance formation of the σ - phase [3]. This phase forms in an eutectoid reaction, given by Equation 2.4 [28]:

$$\alpha \rightarrow \sigma + \gamma_2 \tag{2.4}$$

The binary phase diagram of iron - chromium, in Figure 2.6, shows the σ - phase, but in SDSS the other alloying elements will also affect the phase diagram, giving other regions of temperature and composition combinations where the σ - phase can form.

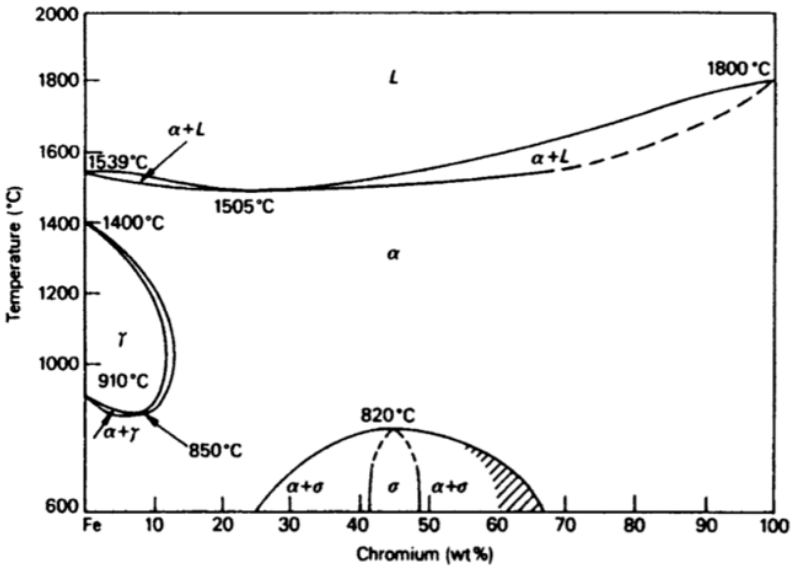

Figure 2.6: Fe - Cr equilibrium diagram, showing the conditions of precipitation of the σ - phase [1].

The precipitation kinetics of the σ - phase includes nucleation and growth and are controlled by thermodynamic driving forces and diffusion [19]. The nucleation of the σ - phase predominantly occurs on the α/α and α/γ grain boundaries, and grows preferentially into the ferrite due to higher concentration of chromium and molybdenum in the ferrite matrix [19, 29]. Another reason for the preferential growth of σ into ferrite is that ferrite is thermodynamically metastable at temperatures where the σ - phase precipitates. A similar composition in ferrite and in the σ - phase indicates that growth of this phase does not require long - range diffusion of elements, such as chromium and molybdenum. As the precipitation continues in the ferrite,

chromium and molybdenum diffuse from the ferrite to the σ - phase, which leads to formation of austenite from ferrite [19]. Assuming spherical precipitates and cubic grains, the volume fraction of σ - phase, X_e, as a function of time, t, during isothermal heat treatment can be estimated by Equation 2.5 [19]:

$$X_e = \frac{4\pi r^3(t)}{3} N(t) \tag{2.5}$$

where r(t) is the radius of a sphere as a function of time and N(t) is the number of nuclei per unit volume as a function of time. The fraction of σ particles precipitated in a DSS during isothermal heat treatment as a function of temperature and time is shown in Figure 2.7, where the highest precipitation rate occurs at around 850°C. Sieurin et al. found that isothermal heat treatment of DSS 2205 at 865°C for 134 seconds gave 1% σ, and should therefore not be exceeded due to detrimental effects on corrosion properties [19].

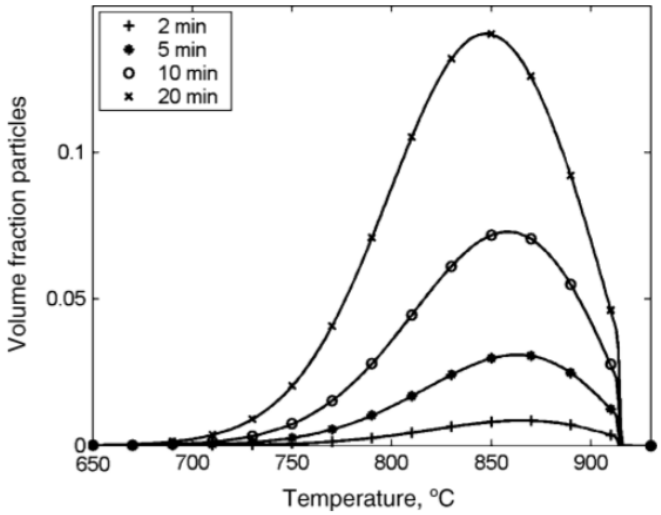

Figure 2.7: Volume fraction of σ - phase particles as a function of temperature and time during isothermal heat treatment of a DSS 2205 [19].

The amount of hard and brittle σ - phase increases with aging time, and the volume content can be minimized by increasing the cooling rate, which is shown in the TTT diagram in Figure 2.5 [29, 30]. Since SDSS contain more alloying elements than DSS, they require faster cooling to avoid formation of the σ - phase [2]. A high solution treatment temperature increases the volume fraction of ferrite, which will be diluted with ferrite forming elements. This will suppress the σ - phase formation, but the conditions for Cr_2N precipitation will be more favourable. This complicates the heat treatment of nitrogen alloyed SDSS, which will be further explained in the section describing the chromium nitrides. The formation of σ - phase in chromium - nickel stainless steels is enhanced when the chromium content exceeds 17 wt%. It forms at grain boundaries during aging at about 850 °C. This is illustrated in Figure 2.8, which presents the microstructure of UNS S32750, aged for 10 minutes at 850 °C, showing σ phase at α/α and α/γ phase boundaries [2].

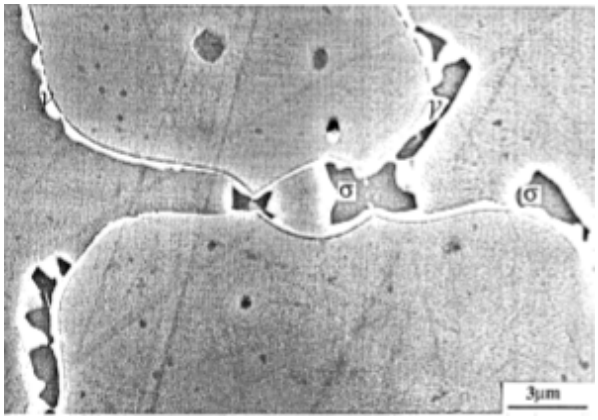

Figure 2.8: Microstructure of UNS S32750 (SAF 2507) aged for 10 minutes at 850 °C. The picture shows the σ - phase at phase boundaries [2].

The morphology of the σ - phase depends on the precipitation temperature [27]. At lower precipitation temperatures, at about 750°C, a coral - like structure of the σ - phase forms. The diffusion velocity is low at low precipitation temperatures, which leads to shorter diffusion distance and higher density of precipitations [27]. At higher precipitation temperatures, the σ - phase is more compact resulting from a lower nucleation formation force but high diffusion rate at elevated temperatures. Morphologies of the σ - phase at three isothermal heat treatment temperatures are given in Figure 2.9.

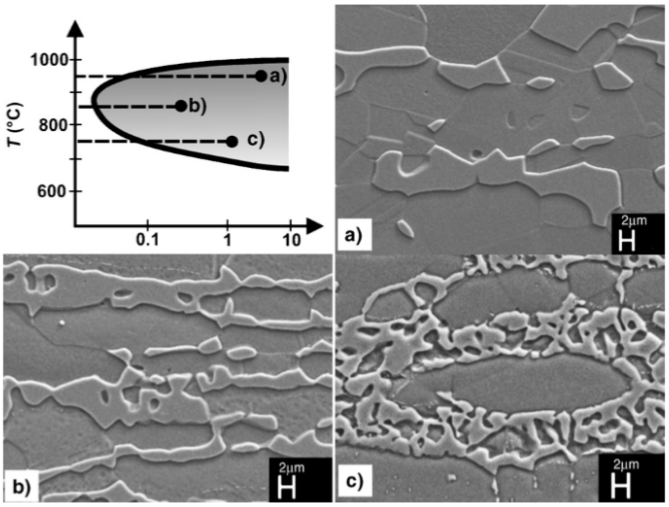

Figure 2.9: Morphology of the σ - phase at isothermal heat treatment temperatures of a) 950°C, b) 850°C and c) 750°C [27].

The ferrite, being richer in chromium, tends to be preferentially absorbed during the growth of the σ - phase [1]. The σ - phase is detrimental to the mechanical performance, because it embrittles SDSS [23]. In addition, it decreases the toughness properties and adversely affects ductility [19, 2]. The σ - phase is more easily generated in SDSS than in DSS since they contain a higher amount of alloying elements, such as chromium and molybdenum, which accelerate precipitation kinetics of the σ - phase [19]. The σ - phase has been found to decrease the corrosion resistance of SDSS [29].

Some authors have found that tungsten - rich weld metals show faster kinetics of intermetallic phase formation, and a higher dissolution temperature of intermetallic phase compared with tungsten - poor and tungsten - free weld metals [22]. This susceptibility to intermetallic precipitation was found to be due to tungsten, which presumably decreases the free energy and formation of nonequilibrium χ - phase. Experiments on precipitation kinetics in SDSS of various compositions by Charles et. al show that tungsten, like molybdenum, increases the precipitation rate of σ - phase and expands the C formed curve in TTT - diagrams towards higher temperatures [2, 22]. No effect of copper was observed in the experiments. Maehara et al. found that nickel accelerates the precipitation kinetics of σ - phase, while the equilibrium volume fraction was reduced [2].

χ - phase

The χ - phase forms in the temperature range of 750 - 850°C [3]. It has an adverse effect on corrosion properties and toughness, which is difficult to separate from the effect of σ - phase since the two phases often coexist, as can be seen from the TTT diagram of UNS S32750 in Figure 2.5 [2]. The χ - phase has been found to form at α/α phase boundaries [31]. In the beginning of the σ - phase precipitation, the χ - phase is consumed in favour of the σ - phase, as shown in Figure 2.10 [27].

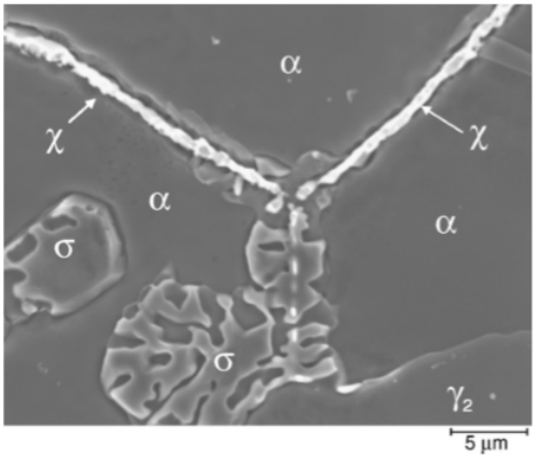

Figure 2.10: Formation of the χ - phase and growth of the σ - phase in a cast DSS [27].

Precipitation of χ - phase can lower the critical pitting temperature (CPT) because it consumes chromium and molybdenum, leading to formation of γ_2 from α, as described below. The χ - phase is also richer in molybdenum than the σ phase, contributing more to the depletion of molybdenum than the σ - phase [32]. This can lead to lower pitting resistance of γ_2, and will be explained in the next section.

Secondary austenite

SDSS are almost entirely ferritic at temperatures just below solidus, but during cooling, transformation from ferrite to austenite will occur [22]. This type of austenite is termed primary austenite and forms through solid state transformation out of the ferrite, given by Equation 2.6:

$$\alpha \rightarrow \gamma \tag{2.6}$$

Additional transformation of ferrite to secondary austenite (γ_2) may occur after the duplex structure has been established, during a subsequent isothermal heat treatment or during welding [22]. It seems to be two types of γ_2, one occurring at the phase boundary between ferrite and austenite, and one occuring in the interior of ferrite grains [22]. The secondary austenite which is characteristic of isothermal heat treatments of the base metal is the one which occurs at the phase boundaries. The type of γ_2 found in welds is essentially of the intragranular type, due to stresses and vacancy clusters in combination with a large number of inclusions in the welded structure [22]. There are three mechanisms for how austenite can precipitate in ferrite, in addition to the direct transformation at high temperatures. The first mechanism is the eutectoid reaction, given by Equation 2.7:

$$\alpha \rightarrow \sigma + \gamma_2 \tag{2.7}$$

The two other mechanisms are formation of austenite as widmansttten precipitates and through martensitic shear process [2]. The eutectoid reaction occurs by rapid diffusion along δ/γ boundaries, and results in an eutectoid structure of σ - phase and austenite in ferrite grains, as shown in Figure 2.11. This occurs in the temperature range of 700 - 900 °C. Below 650 °C, transformation to austenite is diffusionless with respect to substitutional elements, a mechanism that has similarities with the martensite formation. Above 650 °C, where diffusion is more rapid, austenite can be formed as Widmannsttten precipitates.

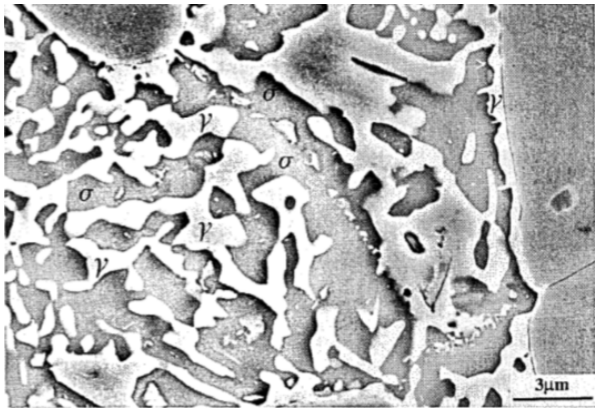

Figure 2.11: Microstructure of UNS 32750 (SAF 2507) aged for 72 h at 700°C. The figure shows how the ferrite has been decomposed into an eutectoid structure of σ - phase and γ_2 [2].

The secondary austenite formed by the eutectoid reaction, given in Equation 2.7, absorbs nickel and rejects chromium and molybdenum. As a consequence, the secondary austenite formed at the α/γ phase boundaries has lower concentration of chromium, molybdenum and nitrogen than primary austenite, particularly when Cr_2N precipitates are present [2, 18]. As the σ - phase forms, chromium and molybdenum are enriched in this particles and nickel diffuses simultaneously into the ferrite [27]. The enrichment of γ stabilizing elements in the ferrite and the loss of α stabilizing elements, lead to an unstable ferrite, transforming into γ_2. The reduced amount of chromium and molybdenum in γ_2 is the reason why pitting attack can occur in that area. Pitting can due to this be a problem although there is no σ - phase present in the microstructure [33]. The lower chromium and molybdenum content is not the only factor for γ_2 being prone to corrosion. The more noble phases near the γ_2 - phase enhances the anodic dissolution of γ_2 [27].

Chromium nitrides

With the increased use of nitrogen in SDSS, the precipitation of Cr_2N has become more important to investigate. The formation of chromium nitrides is likely to occur when rapid cooling takes place from a high solution temperature, due to supersaturation of nitrogen in ferrite [2, 34]. When SDSS undergoes rapid cooling from a high solution temperature, the Cr_2N particles often precipitate intragranularly [35]. The chromium nitrides precipitate from the ferrite by nucleation at dislocations, inclusions and grain boundaries. Isothermal heat treatment in the temperature range of 700 - 900 °C results in intergranular Cr_2N, which has an influence on pitting corrosion of SDSS by reducing the critical pitting temperature (CPT) [2, 36]. The morphology of intragranular and intergranular chromium nitrides in a UNS S32750 SDSS is shown in Figure 2.12a - 2.12b, respectively [37]. It has been found that SDSS with quenched in chromium nitrides had higher corrosion resistance than SDSS with isothermal nitrides [37].

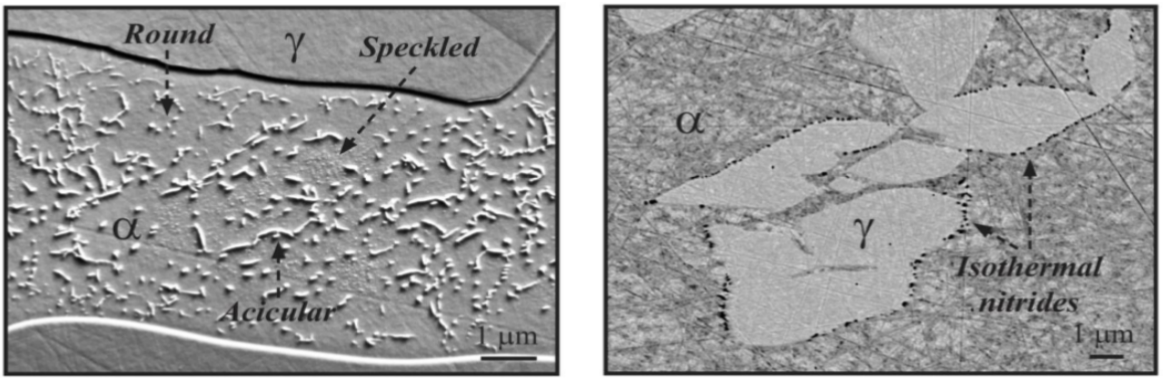

(a) Heat treated at 1125°C for 10 minutes followed by quenching.

(b) Isothermal heat treated at 800°C for 10 minutes followed by quenching.

Figure 2.12: Intragranular and intergranular chromium nitrides in a UNS S32750 SDSS solution annealed and isothermal heat treated, respectively [37].

Chromium nitrides do often coexist with both the χ - phase and the σ - phase, as shown in Figure 2.13.

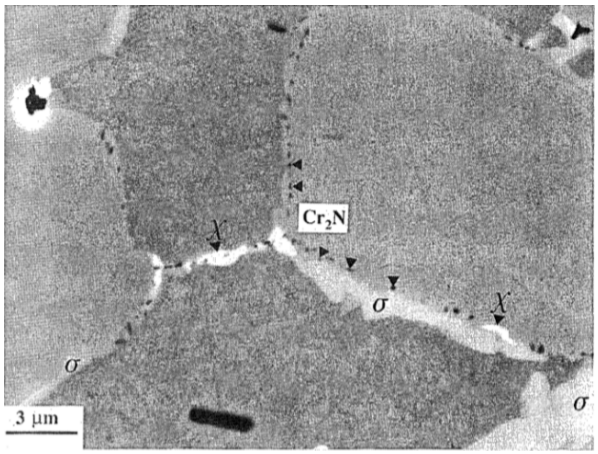

Figure 2.13: Chromium nitrides do often coexist with the σ - and χ - phase, shown here in a backscattered electron (BSE) SEM, for a UNS S32750 SDSS aged for 10 minutes at 850°C [2].

Carbides

Carbides of the type M_7C_3 can precipitate in the temperature range of 950 - 1050 °C, while $M_{23}C_6$ precipitates below 950 °C [2]. Both types of carbides can form at α/γ grain boundaries, but precipitation has also been observed at α/α and γ/γ boundaries. The carbides have a less important role in SDSS due to the low carbon content.

Alpha prime phase

The ferrite phase can decompose into an α - phase rich in iron and an α' - phase rich in chromium. This can form in binary Fe - Cr alloys in the temperature range of 280 - 500 °C, and can lead to embrittlement of SDSS, which is called the 475 °C embrittlement [38]. The α' - phase results in embrittlement of the ferrite and an increase in hardness [2]. Chromium, molybdenum and copper have been found to promote 475°C embrittlement.

2.3 Corrosion of SDSS

General, or uniform, corrosion is when the corrosion attack is assumed to occur homogeneously on the entire surface of the metal [39]. The anodic charge transfer reaction on the metal surface of steels can be the dissolution of iron, given by Equation 2.8:

$$\mathrm{Fe(s)} \longrightarrow \mathrm{Fe^{2+}(aq)} + 2\,\mathrm{e^-} \tag{2.8}$$

The cathodic charge transfer reaction can be the hydrogen evolution reaction or the oxygen reduction reaction, given by Equation 2.9 - 2.12:

$$2\,H^+(aq) + 2\,e^- \longrightarrow H_2(g) \;\; \text{acidic solutions} \tag{2.9}$$

$$2\,H_2O(l) + 2\,e^- \longrightarrow H_2(g) + 2\,OH^-(aq) \;\; \text{alkaline solutions} \tag{2.10}$$

$$O_2(g) + 4\,H^+(aq) + 4\,e^- \longrightarrow 2\,H_2O(l) \;\; \text{acidic solutions} \tag{2.11}$$

$$O_2(g) + 2\,H_2O(l) + 4\,e^- \longrightarrow 4\,OH^-(aq) \;\; \text{alkaline solutions} \tag{2.12}$$

Adsorbed species, as a consequence of anodic dissolution, may form stable oxides or hydroxides instead of soluble iron ions. The stable components can for instance be $Fe(OH)_2$ or $Fe(OH)_3$, where the former can have a dark green color and the latter can have a red brown color [5, 40]. If the oxidized species form a sufficiently adherent film at the metal surface, the anodic dissolution rates can be considerably reduced. The corrosion resistance of SDSS is due to the formation of a relatively thin, adherent film of low ionic permeability [5]. The thickness of the oxide film layer is in the order of 1 to 3 nm, and is composed of water molecules, anions and cations of alloying elements such as iron, chromium or silicon [5]. The corrosion resistance of iron alloys, included SDSS, in seawater rely on the ability to form an adherent, protective oxide film. At which conditions the stable oxides form can be predicted with Pourbaix diagrams. The Pourbaix diagram of pure iron in seawater at 25 °C is shown in Figure 2.14.

The protective nature of oxides depends on structural and kinetic factors which can not be interpreted directly in terms of thermodynamic considerations [5]. Polarization curves can be used to determine kinetic properties by electrochemical measurements. SDSS contain alloying elements which contribute to the formation of a protective oxide film in contact with air. This film can form at high rates and will further protect from general corrosion. The properties of this protective film depends on the content of chromium, molybdenum and nitrogen in the metal.

In low alloyed steels which are exposed to humid environments, a complicated hydroxide, $Fe_3O_4 \cdot nH_2O$, can be formed [9]. This layer is porous and O^{2-} ions can diffuse through it, resulting in a higher amount of corrosion products. In SDSS, chromium forms a dense oxide film on the metal surface, in the presence of oxygen, which protects against corrosion. It is only at high temperature oxidation that chromium forms simple oxides, such as Cr_2O_3, on stainless steels. At low temperatures, the oxide film is more complex, consisting of hydrated Cr_2O_3 as an outer and an inner layer containing iron - chromium oxides [9]. Nickel enhances the formation of a protective oxide film on stainless steels. Molybdenum enhances also the formation of a protective film, and stabilizes it, which leads to slower degradation.

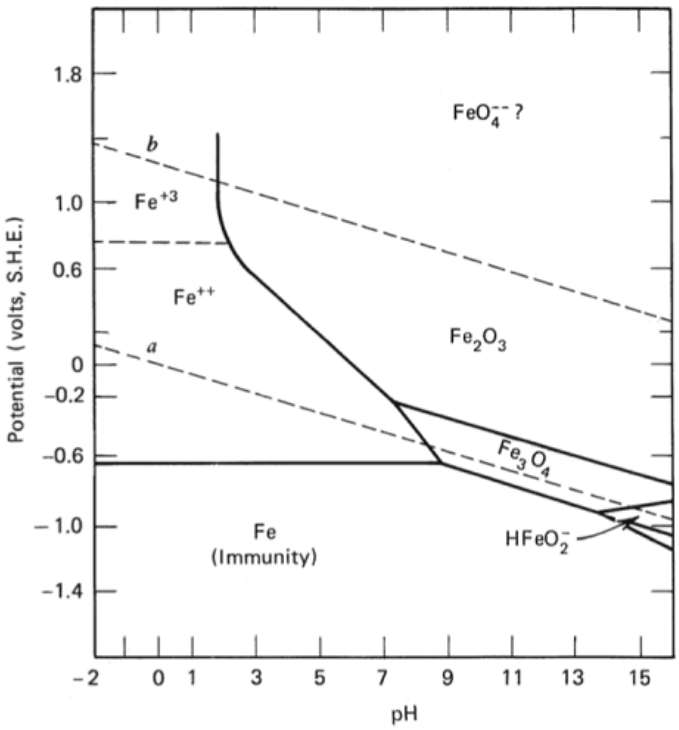

Figure 2.14: Pourbaix diagram of the iron - water system at 25°C, assuming that Fe, Fe_2O_3 and Fe_3O_4 are the only solid substances [41].

Metals that grow network - modifying oxides are more exposed to corrosion. The presence of grain boundaries or other paths of ion movement in the oxide, allows continued film growth. To increase the corrosion resistance, the metal can be alloyed with elements that forms network oxides and the alloying metal will tend to oxidize preferentially. It can segregate to the surface as an oxide film and protect the alloy from further corrosion [42]. Modifiers can break the covalent bonds in a network forming oxide and introduce ionic bonds, giving a mixed oxide. Iron has a valence of two or three in oxides, where the former acts as a modifier and the latter can be a network former [42]. The valence of nickel in oxides is two, and it is a modifier. Chromium has a valence of three and has been found to have properties of both network forming and modifying oxides [42]. Copper can also form oxides and can have a valence of two or three. It can act as a modifier. Based on this four alloying elements, the oxide film of SDSS can contain components such as Fe_2O_3, Fe_3O_4, NiO, Cr_2O_3, Cu_2O and CuO, which protect the metal against corrosion with both network forming oxides and modifiers.

The protective oxide film is not impermeable of chloride ions and SDSS are due to this exposed to localized corrosion in chloride containing environments [9]. If damage occurs on an existing oxide film, it can act as an initiation site for localized corrosion, as will be further described in Section 2.5. When localized corrosion of stainless steels occur, iron can dissolve from the oxides as trivalent iron to divalent iron in a cathodic charge transfer reaction, shown in Figure 2.24 and given by Equation 2.13:

$$Fe^{3+}(aq) + e^- \longrightarrow Fe^{2+}(aq) \tag{2.13}$$

2.4 Galvanic corrosion

When two dissimilar metals are in metallic contact in the presence of a corrosive environment, galvanic corrosion can occur [39]. When the circuit is closed, a net current flows from the more active to the more noble metal. The generation of a net current flow, from the active to the noble component, is a result of increased oxidation of the more active component relative to the oxidation rate at the open circuit potental (OCP). The active component is expected to corrode at a higher rate in metallic contact with the more noble component, than under open circuit conditions. The corrosion rate of the more noble component is expected to decrease as a result of galvanic coupling with the active component. This is applicable to precipitations and intermetallic phases in SDSS. If the electrochemical potential of a precipitate or an intermetallic phase is different from the base metal, it can lead to small galvanic cells in the metal causing galvanic corrosion [39]. This can be detrimental to the corrosion properties of SDSS. The anode to cathode area ratio is a very important factor when determining galvanic corrosion rates. This can be expressed by Equation 2.14 [39]:

$$i_{corr(N-M)} = \frac{A_M}{A_N} \cdot |i_{red(M)}| + |i_{red(N)}| \tag{2.14}$$

where $i_{corr(N-M)}$ is the corrosion current density of the more active metal N, $i_{red(M)}$ is the reduction current density of the more noble metal M, $i_{red(N)}$ is the reduction current density of metal N and A_M and A_N are the areas of metal M and N, respectively. Equation 2.14 shows that metal N corrodes at a higher rate if the area of the more noble metal is large relative to the area of the more active metal. This can be the case for intermetallic and secondary phases in SDSS, where significant differences between the area of such phases and the base metal can occur.

When two dissimilar metals are in electrical contact in an electrolyte, higher OCP differences generally gives higher galvanic corrosion rates [43]. In addition to geometry, area and potential difference, environmental factors as dissolved oxygen content, temperature and chlorination also affect the galvanic corrosion rate [43]. A galvanic series is an arrangement of OCP of metals and alloys measured in a given electrolyte. The galvanic series can be used to investigate the potential difference between a intermetallic or a secondary phase and the base metal in a SDSS, if OCP of the phases, metals and alloys are given. Thierry et. al. measured OCP of different stainless steel grades in seawater under different conditions, and the galvanic series of several stainless steel grades, copper alloys and a nickel alloy at 30°C and 70°C are shown in Figure 2.15a - 2.15b, respectively [43].

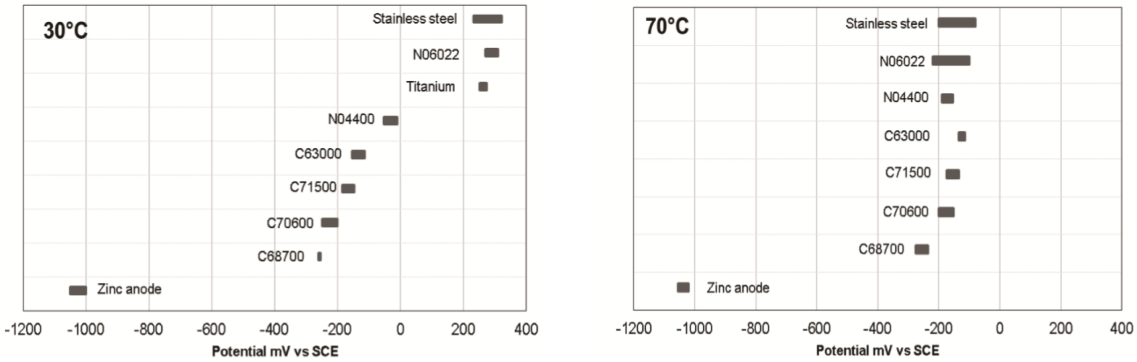

(a) Galvanic series at 30°C.

(b) Galvanic series at 70°C.

Figure 2.15: Galvanic series for some stainless steels, copper alloys and a nickel alloy, N06022, at two different temperatures [43]. For stainless steels a mean value of OCP of several stainless steel grades were used.

2.5 Localized corrosion

Localized corrosion occurs when significant anodic dissolution of a metal appears on a restricted zone of the steel surface, where the rest of the surface is protected by a protective oxide film. When local film breakdown happens on a metal surface, in absence of repairing, it can lead to localized corrosion of the metal [5].

The mechanism for all localized corrosion types consists of the same overall stages. The first stage is initiation, followed by propagation and eventually termination. The initiation step is characterized by local breakdown of a protective film caused by either environmental conditions, such as chloride ions, or material microstructure [5]. The presence of external stresses, high flow rates, hydrogen evolution or anodic currents due to galvanic coupling, can also cause local breakdown of the oxide film [39]. Microstructural factors that can cause localized corrosion are sensitized grain boundaries, inclusions and selective corrosion due to a high potential difference between components in a solid solution alloy. Propagation of localized corrosion is generally characterized by a large cathode area and small, localized anodes. A current balance derived from the mixed potential theory for a corroding system is given by Equation 2.15:

$$(i \cdot A)_{anode} = (|i| \cdot A)_{cathode} \tag{2.15}$$

where $(i \cdot A)_{anode}$ is the anodic current and $(|i| \cdot A)_{cathode}$ is the cathodic current. Since $A_{cathode} >> A_{anode}$, i_{anode} can be high although $i_{cathode}$ may be low.

2.6 Pitting corrosion of SDSS

2.6.1 Mechanism

Pitting corrosion is a form of localized corrosion that produces pits [12]. Once pits develop, they may continue to grow by a self - sustaining mechanism, but certain conditions must exist for pitting to occur. The conditions include an oxide film on the metal surface, certain ions such as the chloride ion and an external or internal electric driving force. The potential of the metal must in addition exceed a potential, the critical pitting potential (E_p) [39]. An external electric driving force may be due to galvanic coupling, while an internal source of current may occur between cathodic inclusions and pits. The oxide on the metal substrate may also act as cathode for pits on the surface, if it has a certain electronic conductivity, which is illustrated in Figure 2.16 [39].

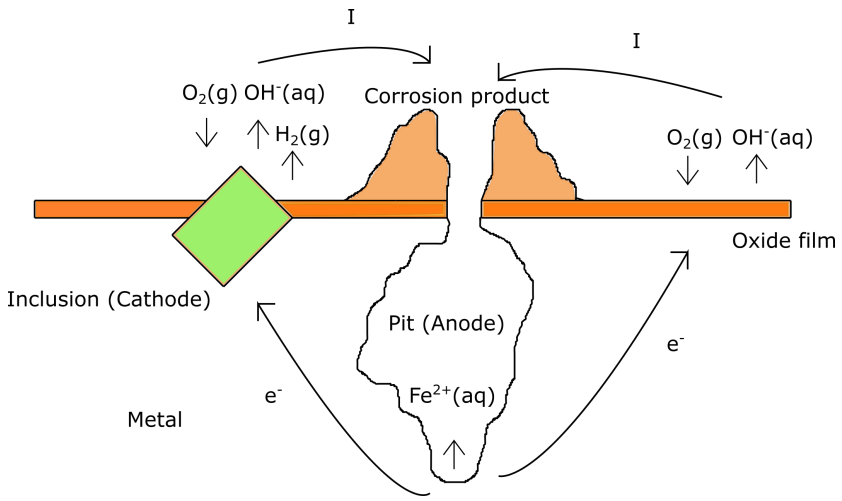

Figure 2.16: Illustration of the mechanism and the driving force for pitting corrosion. Anodic oxidation occurs in a pit, while the reduction processes occur on oxides or inclusions.

Several theories exist about the mechanism for pit initiation. Typical sites for initiation are locations where the oxide is damaged, which can occur as a result of either mechanical or microstructural factors [39]. According to one theory, the chloride ions attack the oxide, given by Equation 2.16 - 2.17:

$$Cl^-(aq) \longrightarrow Cl^-_{ads} \tag{2.16}$$

$$pCl^-_{ads} + M(OH)_n \longrightarrow M(OH)_{n-p}Cl_p + pOH^- \tag{2.17}$$

When the oxide layer is damaged, the chloride ions reach the metal surface leading to oxidation, but oxide repair is also a possible reaction, given by Equation 2.18 - 2.19, respectively:

$$M(s) + Cl^-_{ads} \longrightarrow MCl_{n(ads)} + ne^- \quad \textit{chloride attack} \tag{2.18}$$

$$M(s) + nOH^-_{ads} \longrightarrow M(OH)_{n(ads)} + ne^- \quad \textit{oxide repair} \tag{2.19}$$

When the potential of a metal reaches E_p, the pit will start to initiate after a certain time and the reaction given by Equation 2.18 will dominate. The time before initiation is called the induction time, and depends on the potential of the metal relative to E_p and oxide film thickness. Induction time decreases with increasing potential difference between the metal and E_p, while it increases with increasing film thickness. E_p is a material property, but decreases with increasing chloride concentration and temperature, as illustrated in Figure 2.17.

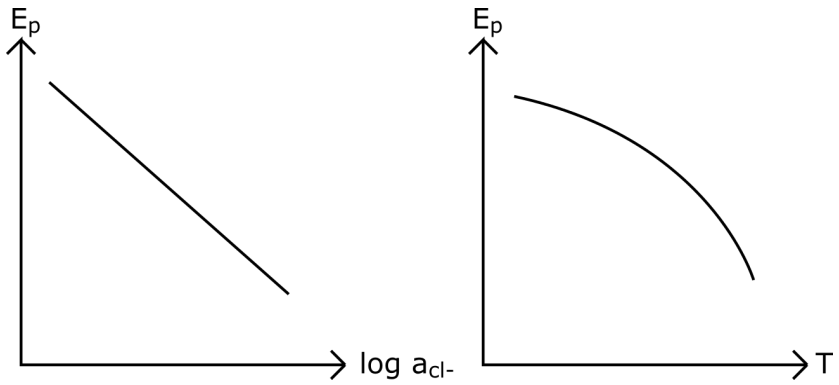

Figure 2.17: Illustration of the variation of E_p with the activity of chloride ions and temperature [39].

The propagation of pits is thought to involve dissolution of the metal and increased acidity at the bottom of the pit, by the hydrolysis of dissolved metal ions [12]. The reactions that may occur inside the pits during propagation are given by Equation 2.20 - 2.22 [39]:

$$nCl^- \longrightarrow nCl^-_{ads} \tag{2.20}$$

$$M(s) + nCl^-_{ads} \longrightarrow MCl_{n(ads)} + ne^- \tag{2.21}$$

$$MCl_{n(ads)} \longrightarrow M^{n+} + nCl^- \tag{2.22}$$

Based on this three reactions, the overall reaction is given by Equation 2.23:

$$M(s) \longrightarrow M^{n+}(aq) + ne^- \tag{2.23}$$

The increased concentration of M^{n+} inside the pit results in migration of chloride ions into the pit to maintain the charge balance. The metal chloride formed is hydrolyzed by water

to hydroxide and HCl [12]. This, in addition to the reactions given by Equation 2.20 - 2.23 lead to different phenomena. The acidity in the pit increases the solubility of salts, especially chloride salts, and chloride ions may migrate into the pit in order to neutralize excess positive charge created by H^+ and M^{n+} ions. Concentrated HCl can then be generated in the pit, which accelerate the rate of pit propagation. Corrosion products can be deposited at the pit opening, leading to more narrow pits. This results in an increased corrosive environment inside the pit.

2.6.2 Kinetics and parameters

SDSS resistance to pitting corrosion is given by PREN, which can be calculated from Equation 2.24 [9]:

$$PREN = \%Cr + 3.3\%Mo + 16\%N \tag{2.24}$$

where the amount of alloying elements are given in weight percent in solid solution. Equation 2.24 is based on chromium, molybdenum and nitrogen, while ISO 21457 includes tungsten into the PREN, given by Equation 2.25 [7, 44]:

$$PREN_W = \%Cr + 3.3 \cdot (\%Mo + 0.5\%W) + 16\%N \tag{2.25}$$

Steels with PREN values over 40 can be used in seawater up to 20°C according to the Norsok standard M - 001 [45, 7]. However, the value of PREN is not enough to decide if SDSS can be used in seawater. Pitting corrosion resistance is strongly dependent on microstructural features, such as ferrite/austenite proportion, the presence of intermetallic precipitates and secondary phases and elemental partitioning between the austenite and the ferrite phase [20, 45]. Parameters, such as E_p, the repassivation potential (E_{RP}), the corrosion potential (E_{corr}) and the flade potential E_{Flade} also affect pitting corrosion resistance of SDSS. The SDSS can be considered pitting corrosion resistant in seawater if E_{RP} - $E_{corr} > 200$ mV [46]. The different parameters can be determined by an electrochemical method, were anodic cyclic potentiodynamic polarization (CPP) curves are recorded based on for instance the ASTM G61 standard [47]. An example of an anodic CPP curve, showing different parameters related to pitting corrosion, is given in Figure 2.18 [46].

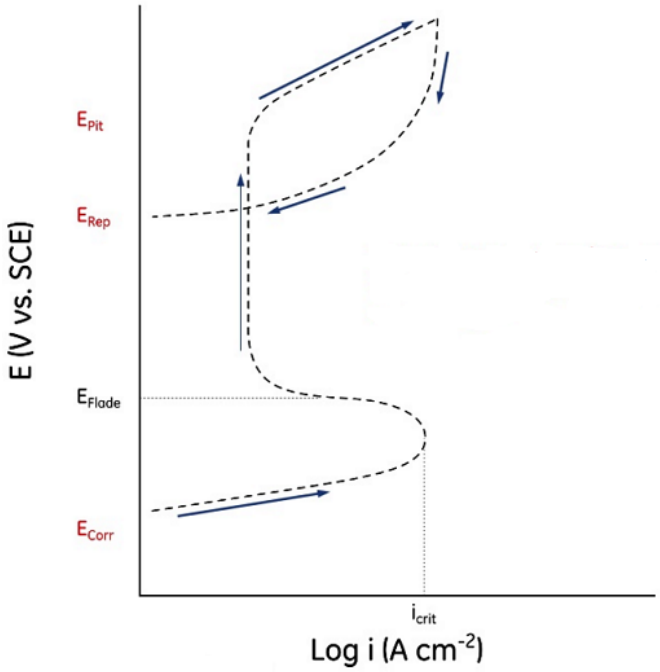

Figure 2.18: Typical anodic CPP curve [46]. E_p is given as E_{pit} in this figure.

E_p can be measured at the inflection point, as illustrated in Figure 2.19 [46].

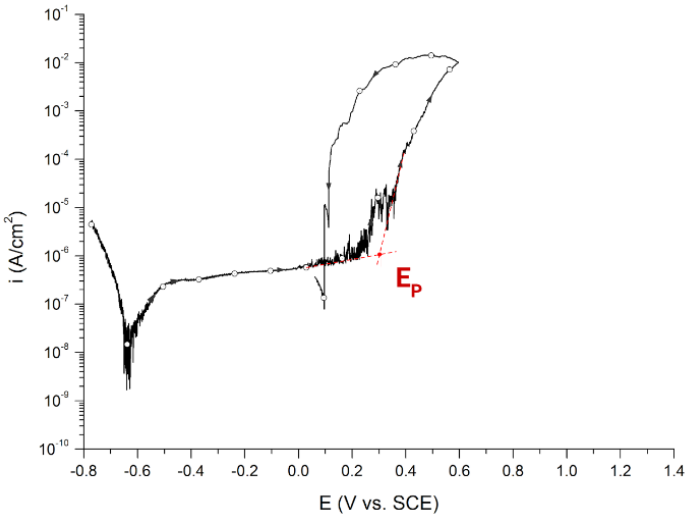

Figure 2.19: Anodic CPP curve showing E_p [46].

E_{RP} is in this thesis defined as the potential when a stable oxide film forms after pits have been formed. This potential is defined to be where the current density is below $2\mu A/cm^2$, as illustrated in Figure 2.20. The passive current density (i_p) can be defined as the average or mid point of the current density in the potential area where oxide film forms.

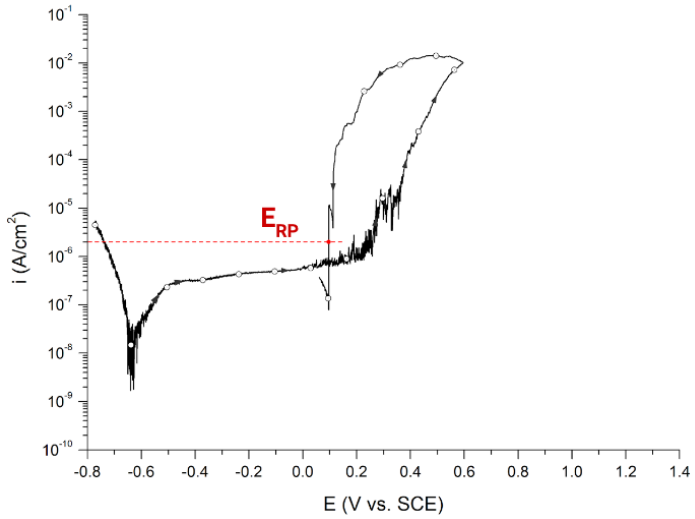

Figure 2.20: Anodic CPP curve showing E_{RP} [46].

The electrochemical response of anodic CPP curves can be divided in three distinctive cases [48]. The curve can include no hysteresis, indicating anodic dissolution and oxygen evolution, which can be the case at low electrolyte test temperatures. Dissolution of austenite has been found to occur at higher potentials than dissolution of ferrite in DSS, and the ferrite - phase has generally been found to dissolute at a higher rate than austenite [49, 50]. The second case is when the curve includes a little hysteresis with high breakdown potentials and small pits, which can be the case for electrolyte test temperatures close to CPT. The third case is when the curve has a positive hysteresis and clear signs of pitting corrosion, which can be the case for elevated temperatures and/or the presence of detrimental phases, such as the σ - phase. Examples of the three cases are shown in Figure 2.21 - 2.23, respectively [48].

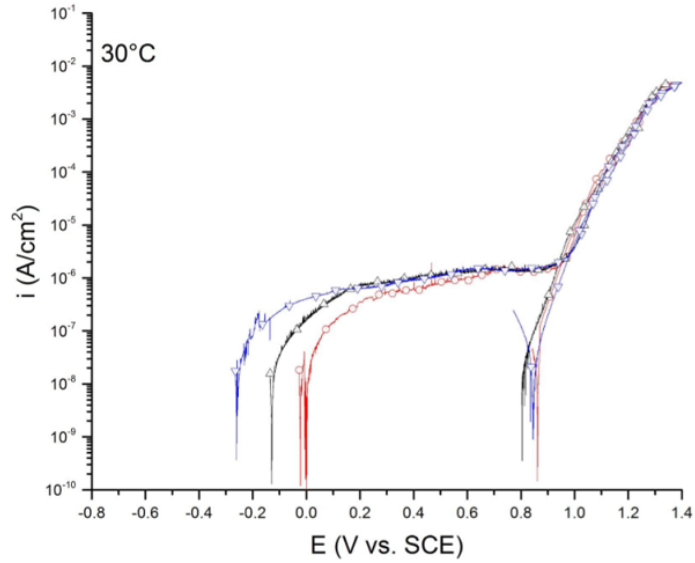

Figure 2.21: Anodic CPP curve with no hysteresis, indication anodic dissolution and oxygen evolution [48]. This is the case at low electrolyte test temperatures.

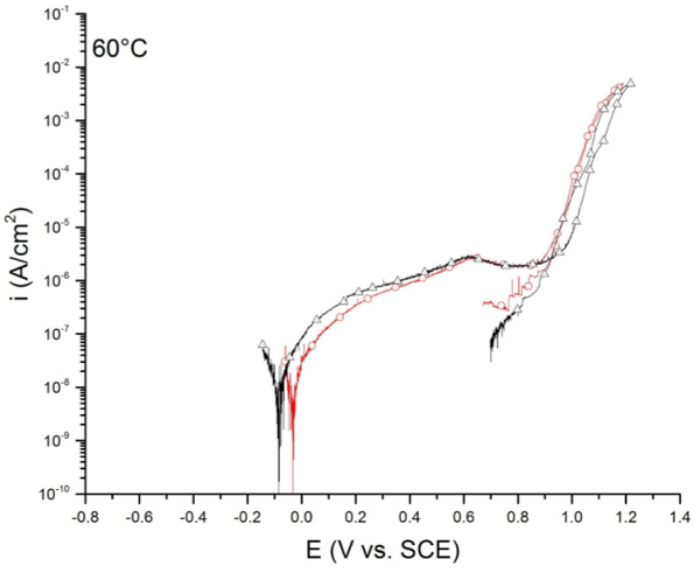

Figure 2.22: Anodic CPP curve with little hysteresis, very high breakdown potentials and small pits [48]. This is the case at temperatures close to CPT.

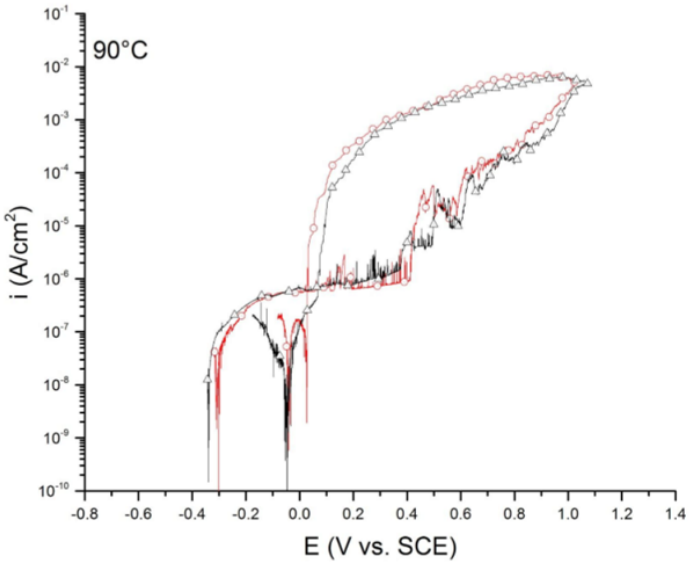

Figure 2.23: Anodic CPP curve with hysteresis and clear signs of pitting corrosion. This is the case at elevated temperatures and/or with the presence of detrimental phases such as the σ - phase.

Another way to determine pitting corrosion resistance of SDSS is to evaluate the CPT. CPT is defined as the minimum temperature to produce pitting on a surface of a specimen, and the lowest potential - independent temperature, below which pitting does not occur [51]. This parameter can be determined at the inflection point of a E_p vs. temperature plot or by the ASTM G48 standard [52]. This parameter can also be determined by an electrochemical method, where OCP of a test specimen in a ferric chloride ($FeCl_3$) solution is logged. The temperature where a fall in OCP, from about 700 mV_{SCE} below 500 mV_{SCE}, can be defined as the CPT [53]. This is a modified version of the ASTM G48 standard, and is based on the

effect of increased temperature or increased amount of intermetallic precipitates and secondary phases on polarization curves of SDSS, as shown in Figure 2.24.

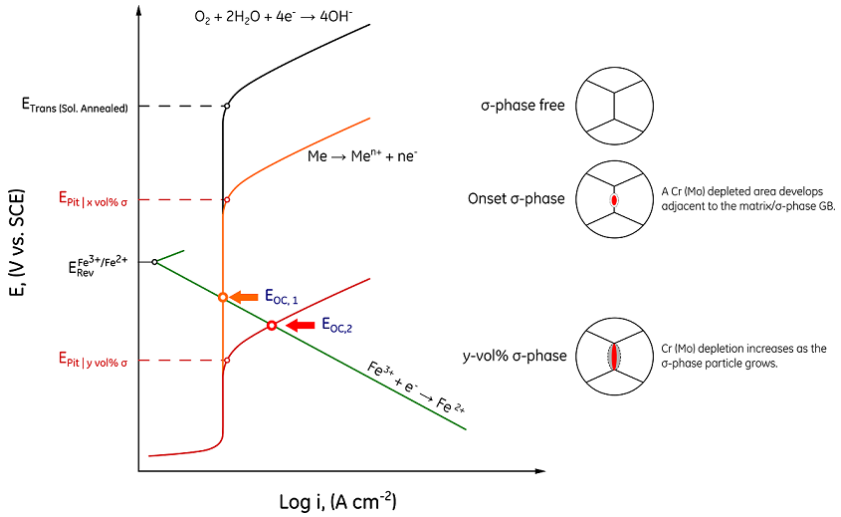

Figure 2.24: Effect of increased amount of intermetallic precipitates and secondary phases on polarization curves of SDSS.

2.6.3 Effect of microstructure

The microstructure of SDSS affects the CPT and is highly dependent of intermetallic precipitates and secondary phases. As an example, Figure 2.25 shows CPT as a function of aging temperature from previous work [24]. Park et al. found that CPT decreased with increasing aging time, and with increasing volume fraction of the σ - phase [54]. Mathiesen et al. found a reduction in corrosion resistance of DSS with increasing amount of σ - phase by CPT measurements, and that the effect became evident for volume fractions of σ - phase above 4% [55]. They also found that for the same amount of σ - phase, the effect was stronger for materials heat treated at 750°C than 850°C. This was due to steeper concentration gradients along the σ - phase precipitates due to slower diffusion rate at the lowest temperature.

In the two phase structure of SDSS, chromium and molybdenum are preferentially partitioned to ferrite, while nickel and nitrogen are preferentially partitioned to austenite. This can result in different PREN values of the two phases [18]. To obtain equal pitting corrosion resistance for both phases, alloying and selection of annealing temperature are important. Nitrogen lowers the partitioning ratio for chromium, nickel and molybdenum, while nickel enhances the element partitioning of chromium and molybdenum. By increasing the annealing temperature, the differences in composition for important alloying elements are reduced. When the content of nitrogen in the steel increases, the PREN value of austenite is higher than of ferrite [18].

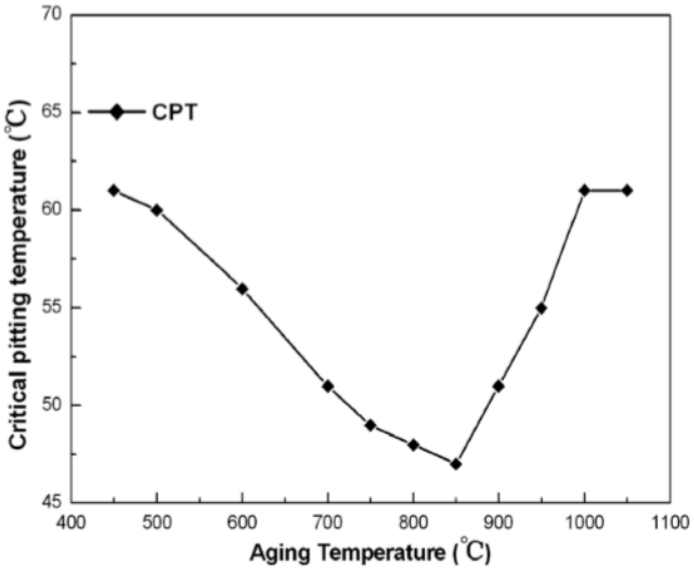

Figure 2.25: CPT of a DSS grade UNS S31803 specimens aged at several temperatures for 10 minutes plotted against aging temperature. A reduction in CPT reveals at which aging temperature the material has a reduction in pitting corrosion resistance, due to microstructural aspects [15].

The pitting behavior of DSS and SDSS depends on the microstructure, due to several reasons. Manganese sulphide precipitations at grain boundaries and higher diffusion rate of chromium in ferrite than in austenite are two examples on how the pitting resistance depends on the microstructure. In addition, preferentially partition of molybdenum and chromium in ferrite and nickel and nitrogen in austenite affects the pitting corrosion resistance [12]. In DSS and SDSS, sulfur is thought to partition preferentially to ferrite, and to precipitate as manganese sulfide at the grain boundaries between austenite and ferrite. Pits are often found to initiate at the austenite - ferrite grain boundaries in DSS and SDSS, which may be due to this precipitation [3]. Once pits have initiated in manganese sulphide or other phases at the α/γ boundaries, they can propagate into one of the two phases.

If nitrogen is present only as an impurity, the preferential partitioning of chromium and molybdenum to ferrite leads to a ferrite phase more resistant to pitting, resulting in pit propagation in the austenite phase. If the steel contains significant amounts of nitrogen, it is preferentially partitioned to austenite, which gives an austenite phase more resistant to pitting than the ferrite phase, and pit propagation occurs in ferrite. Tavares et al. characterized microstructure, chemical composition and corrosion resistance in root pass and filler passes of a weld in a UNS S32750 super duplex stainless steel, through cyclic polarization test [45]. It was found that the base metal, root pass and filler passes had the same pitting potential, about 1,0V$_{SCE}$, but the root pass, with excess of ferrite phase and chromium nitrides, had a higher degree of corrosion during the cyclic test [45]. Some authors have found that CPT decreases due to chromium nitrides [3].

In DSS and SDSS with more than 4,5 wt% copper, and nitrogen only at the impurity level (lower than 0,02 wt%), a copper - rich phase has been formed at the α/γ grain boundaries.

This phase has been found to act as pit initiation sites [12]. The presence of the σ - phase, as described in Section 2.2.1, has been shown to reduce E_p [12]. The σ - phase contains high amounts of chromium and molybdenum, which are ferrite stabilizers in SDSS. The precipitation of this phase causes depletion of chromium and molybdenum from surrounding ferrite and austenite, leading to a reduction in pitting corrosion resistance in the depleted zones, near the precipitates [3]. It has been shown that only 1 vol% σ - phase reduces the corrosion resistance of SDSS[16]. Park et al. studied DSS in 10wt% $FeCl_3 \cdot 6H_2O$, and found that CPT decreased with an increase in σ - phase precipitation [3]. Ezuber et al. found that pitting corrosion in SAF 2205 duplex stainless steel increased markedly with increasing heat treatment duration at 845 °C and with increasing seawater temperature [26]. They also found that the pits initiated at α/γ phase boundaries and propagated more preferentially into ferrite, indicating the beneficial effect of nitrogen in austenite [26].

Pohl et al. observed that as the σ - phase was formed, the amount of chromium and molybdenum increased in the σ - phase and nickel diffused into the ferrite [27]. The enrichment of γ stabilizers in the ferrite and the reduction of α stabilizers lead to formation of γ_2. The γ_2 is depleted in chromium and molybdenum, which reduces the corrosion resistance of this phase. Other authors have found that DSS is immune to pitting corrosion if low amounts of σ - phase is present at ambient temperature. However, pitting corrosion was initiated at higher temperatures due to damage of the oxide film [26]. Martins et al. found that E_p decreases with increasing temperature of SDSS castings [56].

2.6.4 Effect of tungsten

Tungsten is often added as an alloying element intentional rather than as a cost - saving strategy [6]. Additions of tungsten in SDSS has been found to increase E_p and decrease i_p, which is illustrated in Figure 2.26 [12].

Several researchers seem to agree that there is an optimal concentration of tungsten in stainless steels [6]. Tomashov et al. reported that tungsten had a net beneficial effect at around 3 wt% in a 18 - wt%Cr, 14 - wt%Ni alloy [48]. Ash et al. concluded that tungsten and molybdenum increased E_p in almost the same amount when measuring the potentials of Fe - 29 - wt%Cr alloys in 4M $MgCl_2$ at 80°C [6]. Kim and Kwon reported that a tungsten to molybdenum ratio of 2 gave the best localized corrosion resistance, and Ogawa et al. reported a maximum in pitting corrosion resistance at 2 wt% tungsten in SDSS [6].

Tungsten can increase the corrosion resistance of SDSS in several ways. Enrichment of tungsten in the oxide film, as WO_3, or as dissolved ions, tungstate $WO_4{}^{2-}$, can inhibit electrolyte entering pits and crevices [6]. Bui et al. reported that addition of tungsten and dissolved tungstate to a 16 wt% Cr - 14 wt% Ni stainless steel alloy increased E_p in a 0,1M NaCl solution at 25°C [48].

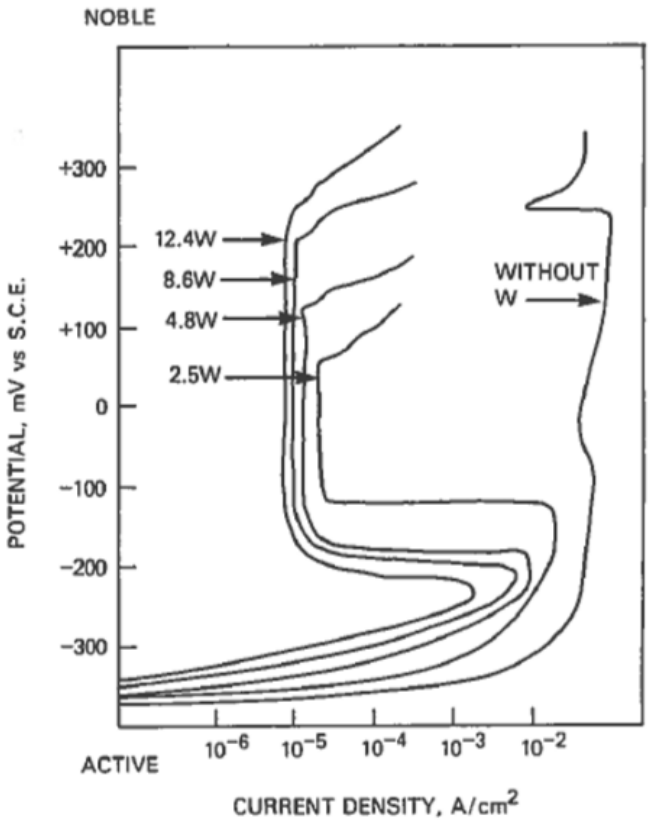

Figure 2.26: Effect of tungsten on polarization curves [12].

Tungsten can either accelerate or decrease precipitation kinetics of deleterious intermetallic precipitates and secondary phases during welding. Ogawa et al. and Kim and Kwon studied the precipitation kinetics in DSS, with and without tungsten, and found that tungsten promotes formation of the χ - phase and Cr_2N at grain boundaries, reducing the number of nucleation sites for σ - phase precipitation [6]. This means that tungsten reduces the formation kinetics of the σ - phase. Ogawa et al. have also found that tungsten increased pitting corrosion resistance of the base metal and the HAZ with a maximum at 2 - 3 wt% tungsten [48]. Jeon et al. also reported that tungsten strongly favoured the precipitation of the χ - phase, improving the overall pitting corrosion resistance, when substituting molybdenum with tungsten in a DSS [57]. They also reported that addition of tungsten reduced the total volume fraction of secondary phases.

Park et al. found, by anodic polarization tests that there was less σ - phase precipitation in the tungsten added specimen compared to specimens only containing molybdenum [16]. The specimens with tungsten were also more resistant against corrosion after aging treatment, and pitting occurred in chromium and molybdenum depleted zones around the σ - phase [16]. It has been found by anodic CPP that tungsten increases CPT by investigating and comparing the localized corrosion properties of UNS S32750 and UNS S39274. This is illustrated in Figure 2.27. This study found that tungsten improve the localized corrosion properties of SDSS and that CPT of UNS S39274 was 85°C against 70°C for UNS S32750 [6].

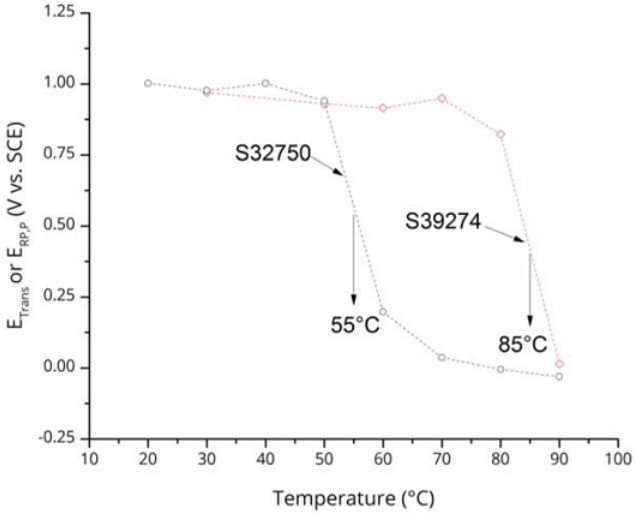

Figure 2.27: CPT of UNS S32750 and UNS S39274 [6].

Chapter 3

Experimental work

The objective with the experimental work was to investigate the effect of isothermal heat treatments on pitting corrosion properties of UNS S39274. This chapter presents first the procedure for isothermal heat treatments. This was done at 820°C, 870°C and 940°C for a selection of isothermal heat treatment times. Then, the setup and procedure for the electrochemical measurements are presented. The electrochemical measurements consisted of a modified ASTM G48 method and ASTM G61 anodic CPP. After electrochemical measurements, surface characterization was performed by optical microscope (OM), 3D OM and scanning electron microscope (SEM) to investigate pitting corrosion morphology.

3.1 Test material

The SDSS grade UNS S39274 was used as test material in this work. The UNS S39274 samples were delivered by Sumitomi. All specimens were machined at the workshop at the Department of Engineering Design and Materials (IPM). The chemical composition of UNS S39274 is given in Table 3.1, and the material datasheet is given in Appendix A. The $PREN_W$ of UNS S39274 was calculated by Equation 2.25, and found to be 43,20.

Table 3.1: Chemical composition of UNS S39274, used in the experimental work.

Element	**UNS S39274** [**wt**%]
Cr	24,9
Ni	6,3
Mo	3,1
W	2,08
Mn	0,72
Cu	0,47
Si	0,25
N	0,29
C	0,018
P	0,019
S	0,0002

In this work, circular samples with a diameter and width of 25 and 2 mm, respectively, were used as test materials. Each sample contained a hole, with a diameter of 2 mm, to connect the samples to a circuit with a platinum wire when used in electrochemical measurements. An overview of the geometry of the samples is shown in Figure 3.1. The area was found to be 11,3 cm^2, calculated from Equation 3.1:

$$A_{sample} = \frac{\pi \cdot d_1^2}{2} + \pi \cdot d_1 \cdot b - \frac{\pi \cdot d_2^2}{2} \tag{3.1}$$

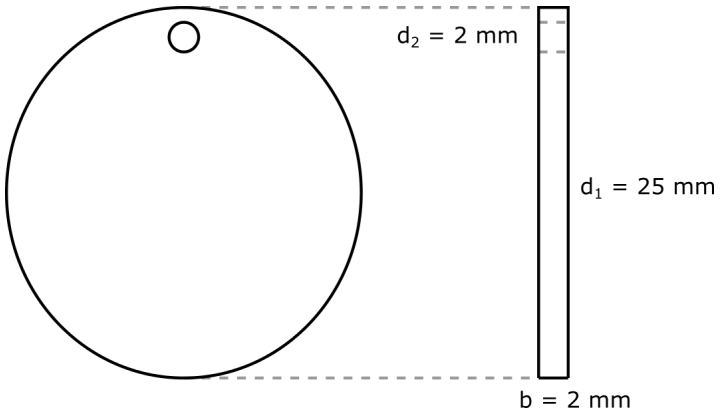

Figure 3.1: Test sample geometry used in the experimental work.

3.2 Heat treatment

3.2.1 Solution annealing

All heat treatments were done in a Nabertherm N17/HR oven. All SDSS samples were solution annealed before they were isothermal heat treated. The specimens were solution annealed at 1110 °C for 15 minutes, followed by water quenching at ambient temperature. Solution annealing was done by placing all samples in a pre - heated oven. The time for the samples to reach the wanted temperature of 1110 °C was added to the 15 minutes of solution annealing. The added time was found by logging the temperature in the middle of one sample in a test experiment, and the heating rate was found to be 25°C/second. The objective with the solution annealing was to obtain similar grain sizes and to remove heat treatment history to secure equal conditions for all samples.

3.2.2 Isothermal heat treatment

After solution annealing, a selection of samples were isothermal heat treated to obtain formation of intermetallic precipitates and secondary phases. Temperatures and times for the isothermal heat treatments were decided from a TTT - diagram of UNS S32750, given in Figure 2.5 [2]. This was done since the two SDSS grades UNS S39274 and UNS S32750 have a similar chemical composition. The temperature and time conditions were decided to obtain different content and degree of precipitation of intermetallic and secondary phases, especially considering the χ - and σ - phase, γ_2 and chromium nitrides. The intermetallic precipitates and secondary phases start to precipitate at 800°C. For that reason, the time for a sample to be heated from ambient temperature to 800°C was added to the isothermal heating time (IHt). The isothermal heating temperatures (IHT) and IHt, used in this work, are shown in Figure 3.2, illustrated by the TTT diagram of UNS S32750 and summarized in Table 3.2. An illustration of the heat treatment procedure of the SDSS samples is given in Figure 3.3.

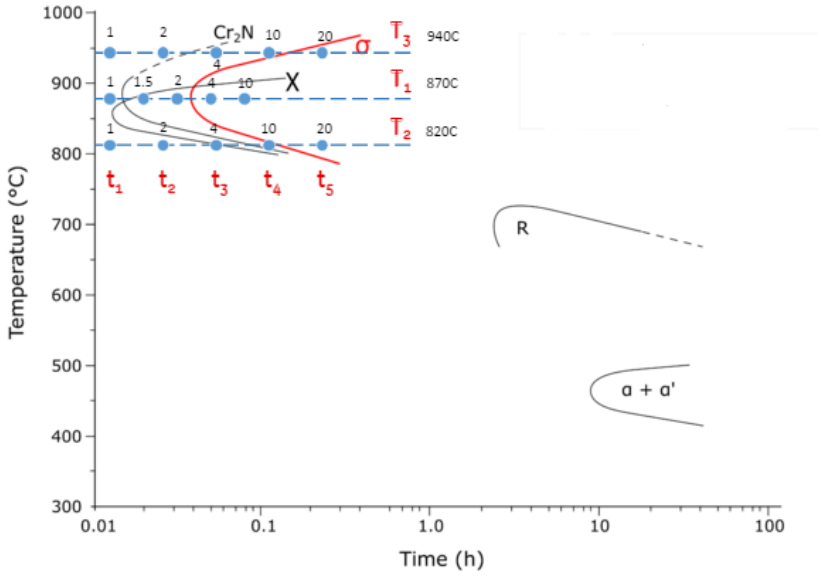

Figure 3.2: Temperature and time conditions of isothermal heat treatments of the SDSS samples, resulting in formation of intermetallic precipitates and secondary phases [2]. Note that the numbered times, given by blue dots in the TTT diagram, are given in minutes.

Table 3.2: Temperature and time conditions of isothermal heat treatments of UNS S39274. The number of samples for each heat treatment is also given.

Heat treatment notation	**Number of samples**	**Temperature [°C]**	**Time [min]**
Solution annealing	8	1110	15
T_1t_1	8	870	1
T_1t_2	8	870	1,5
T_1t_3	8	870	2
T_1t_4	2	870	4
T_1t_5	0	870	10
T_2t_1	2	820	1
T_2t_2	2	820	2
T_2t_3	8	820	4
T_2t_4	0	820	10
T_2t_5	2	820	20
T_3t_1	2	940	1
T_3t_2	2	940	2
T_3t_3	8	940	4
T_3t_4	0	940	10
T_3t_5	2	940	20

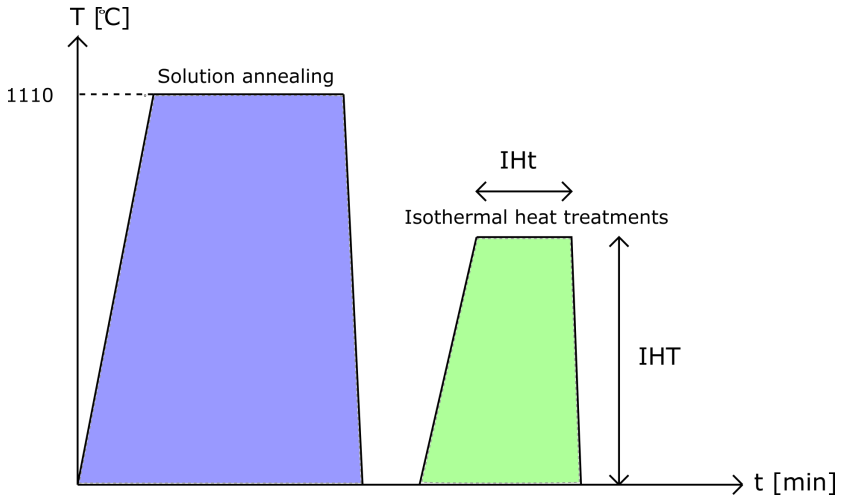

Figure 3.3: Illustration of the heat treatment procedure for the test samples. The heat treatment consisted of solution annealing, followed by water quenching, and isothermal heat treatments.

3.3 Electrochemical measurements

Two electrochemical measurements were performed, CPT measurements by a modified ASTM G48 method and anodic CPP by ASTM G61, to investigate the effect of isothermal heat treatment on the pitting corrosion properties of UNS S39274. Prior to electrochemical testing, all samples were grinded with 320, 500, 800, 1200 and 2400 SiC paper followed by polishing with 3 and 1 μm diamond spray. The samples were then rinsed in an ultrasonic bath for 5 minutes. They were then cleaned with distilled water, air dried and stored in a dessicator for at least 24 hours.

3.3.1 Reference electrode

A standard calomel electrode (SCE), immersed in a saturated potassium chloride (KCl) solution, was used as a reference electrode in all experiments performed in this work. The half reaction in the reference electrode is given by Equation 3.2 [58]:

$$\mathrm{Hg_2Cl_2(s) + 2\,e^- \longrightarrow 2\,Hg(l) + 2\,Cl^-(aq)} \tag{3.2}$$

All potentials in this report are given with respect to the SCE reference electrode and the standard potential of the SCE is approximately 241 mV_{SHE}. A hose filled with electrolyte and a cotton string was used to secure electrical connection between the electrolyte and the reference electrode for all electrochemical measurements.

3.3.2 Critical pitting temperature measurements

CPT of the test specimens were obtained based on a modified method of the ASTM G48 standard, and are called CPT measurements further in this report [52, 53]. The electrolyte used in this tests was made by dissolving 100g $FeCl_3 \cdot 6H_2O$ in 900 mL distilled water, giving a total of about 6 wt% $FeCl_3$. The salt was dissolved by a magnet stirrer at ambient temperature. The test specimen was immersed in a 1000 mL beaker containing preheated electrolyte, on a heating plate. OCP was recorded and logged while the specimen was immersed in the electrolyte. At the beginning of each measurement, the electrolyte temperature was set to 40 °C. The temperature was adjusted +5 °C every 24 hour. This was done until the OCP dropped below 500 mV_{SCE}, indicating that the metal was in the active area. The test specimen was then removed, rinsed with distilled water. An illustration of the test setup is given in Figure 3.4. An overview of the test setup used for CPT measurements is shown in Figure 3.5, with numbered components specified in Table 3.3. The test matrix for CPT measurements is given in Table 3.4.

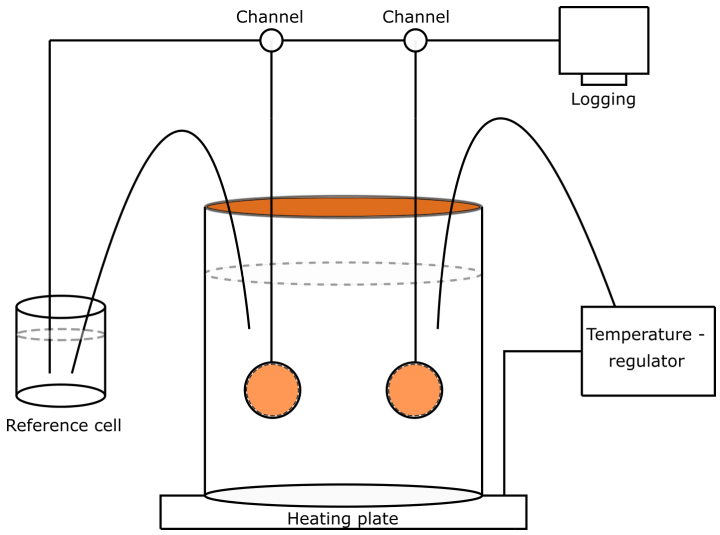

Figure 3.4: Schematic presentation of the test setup used for CPT measurements [52, 53].

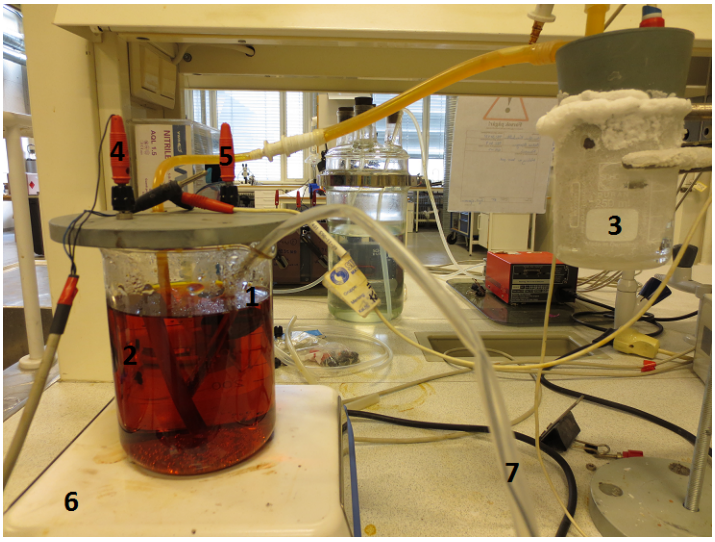

Figure 3.5: An overview of the test setup used for CPT measurements. Numbered components are specified in Table 3.3.

Table 3.3: Numbered components in the test setup in Figure 3.5.

Item #	**Explanation**
1	Test sample 1
2	Test sample 2
3	Reference cell with reference electrode (SCE)
4	Logging channel for test sample 1
5	Logging channel for test sample 2
6	Heating plate
7	Temperature regulator

Table 3.4: Test matrix for CPT measurements of UNS S39274.

Sample number	**Heat treatment temperature [°C]**	**Isothermal heating time [min]**
1.1, 1.2	1110	Solution annealed
1.3, 1.4	870	1
1.5, 1.6	870	1,5
1.7, 1.8	870	2
1.9, 1.10	870	4
1.11, 1.12	820	1
1.13, 1.14	820	2
1.15, 1.16	820	4
1.17, 1.18	820	20
1.19, 1.20	940	1
1.21, 1.22	940	2
1.23, 1.24	940	4
1.25, 1.26	940	20

3.3.3 Anodic cyclic potentiodynamic polarization curves

Anodic CPP curves were recorded to obtain the parameters OCP, E_p, E_{RP} and i_p. The anodic CPP was performed according to the ASTM G61 standard [47]. The electrolyte used in the experiments was made by dissolving 34 g sodium chloride (NaCl) in 920mL distilled water, giving about 3,56 wt% NaCl. The salt was dissolved by a magnet stirrer at ambient temperature. A setup with three electrodes was used in this experiments, where the test specimen was used as working electrode and a platinum mesh as counter electrode. A Gamry Interface 1000 potentiostat was used to obtain the anodic CPP curves. Before polarization, OCP was measured for one hour. The electrolyte was bubbled with N_2(g) through a hose during the tests, to secure minimal dissolved oxygen gas (O_2) in the electrolyte. Anodic CPP curves were recorded by polarizing the test specimen in anodic direction, from OCP, until the current density reached 5 mA/cm^2. After this value was reached, the polarization was reversed until the potential retrieved OCP, that was measured prior to anodic CPP. The anodic CPP curves were obtained by polarizing the sample 600 mV/hour, with 10 measurements each minute. Three electrolyte test temperatures were used in anodic CPP measurements, 40°C, 60°C and 80°C. An illustration of the test setup based on the ASTM G61 standard is given in Figure 3.6. An overview of the test setup is shown in Figure 3.7, with numbered components specified in Table 3.5. The test matrix for anodic CPP is given in Table 3.6.

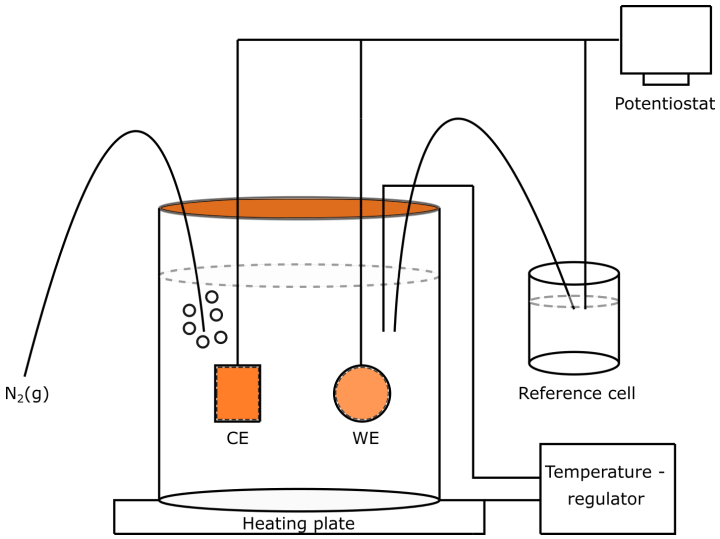

Figure 3.6: Illustration of the test setup based on the ASTM G61 standard, used to obtain anodic CPP curves. WE and CE are the working and counter electrode, respectively.

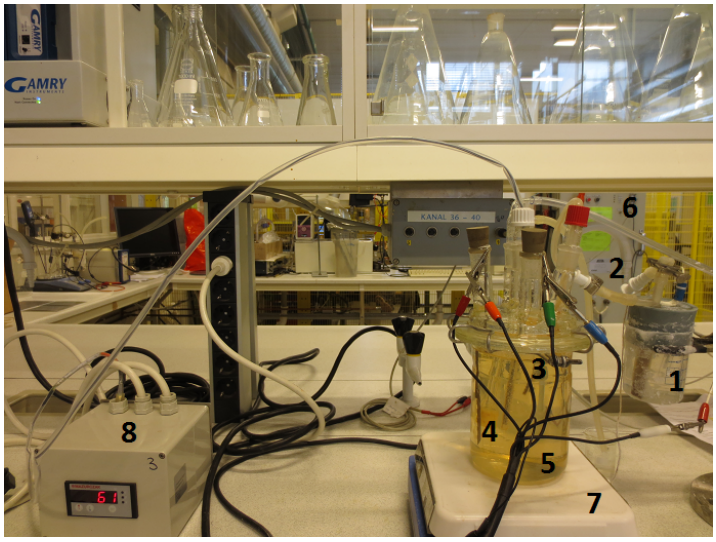

Figure 3.7: An overview of the test setup used to obtain anodic CPP curves. Numbered components are specified in Table 3.5.

Table 3.5: Numbered components in the test setup shown in Figure 3.7.

Item #	**Explanation**
1	Reference cell with reference electrode (SCE)
2	Hose filled with electrolyte and cotton string (salt bridge)
3	Working electrode (test specimen)
4	Counter electrode (platina (Pt) mesh)
5	Container with test specimen (SDSS), counter electrode and electrolyte
6	Hose supplying N_2(g)
7	Heating plate
8	Temperature regulator

Table 3.6: Test matrix for the ASTM G61 electrochemical tests, used to obtain anodic CPP curves.

Sample number	**Heat treatment temperature [°C]**	**Isothermal heating time [min]**	**ASTM G61 temperature [°C]**
2.1, 2.2	1110	Solution annealed	40
2.3, 2.4	1110	Solution annealed	60
2.5, 2.6	1110	Solution annealed	80
2.7, 2.8	870	1	40
2.9, 2.10	870	1	60
2.11, 2.12	870	1	80
2.13, 2.14	870	1,5	40
2.15, 2.16	870	1,5	60
2.17, 2.18	870	1,5	80
2.19, 2.20	870	2	40
2.21, 2.22	870	2	60
2.23, 2.24	870	2	80
2.25, 2.26	820	4	40
2.27, 2.28	820	4	60
2.29, 2.30	820	4	80
2.31, 3.32	940	4	40
2.33, 2.34	940	4	60
2.35, 2.36	940	4	80

After anodic CPP, some corrosion products, were left in the beaker. After ended tests at electrolyte temperature of 40°C, the corrosion product in the beaker was red brown, as shown in Figure 3.8a. After ended tests at electrolyte temperature of 80°C, the corrosion product in the beaker was black green, as shown in Figure 3.8b.

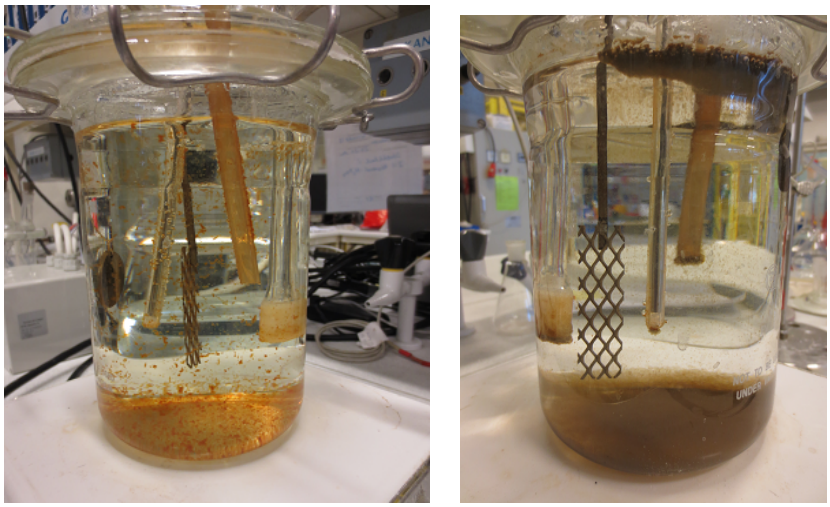

(a) After anodic CPP at 40°C. (b) After anodic CPP at 80°C.

Figure 3.8: Corrosion products after anodic CPP.

3.4 Surface Characterization

Surface characterization before electrochemical measurements was done by another master student in SEM, to document the microstructure after heat treatments. The exposed surfaces of the test specimens after electrochemical measurements were characterized by OM and 3D OM. The OM used for surface characterization of all test specimens was a Leica MEF4M OM and a confocal 3D OM. In addition, the depth and width of some pits of some of the samples after the ASTM G61 anodic CPP were measured in 3D OM.

Chapter 4

Results

This chapter presents the results from the experimental work on the SDSS grade UNS S39274 according to test matrix given in Table 3.4 and Table 3.6. Surface characterization of the microstructure by SEM after heat treatments is presented first and was performed by another master student. The electrochemical measurements are presented as CPT and anodic CPP curves. CPT is given as a function of IHt and IHT. The anodic CPP curves were used to obtain the parameters OCP, E_p, E_{RP}, i_p, describing pitting corrosion properties of UNS S39274. Surface characterization of samples by OM and 3D OM after electrochemical measurements are then presented, and was done to investigate the degree of pitting corrosion, pitting morphology and pit depth and width. Surface characterization of one sample after ASTM G61 anodic CPP by SEM was also performed. All surface characterization in SEM was performed by another master student.

4.1 Microstructure after heat treatments

The objective with the isothermal heat treatments was to simulate welding procedures and to achieve formation of intermetallic precipitates and secondary phases. The presented microstructures in this section are in accordance with the heat treatments in Table 3.2. The microstructure after solution annealing is shown in Figure 4.1. The microstructures after isothermal heat treatment at 870°C for 1 - 4 minutes, are shown in Figure 4.2a - 4.2d, respectively. A higher amount of intermetallic precipitates and secondary phases can be observed with increasing IHt.

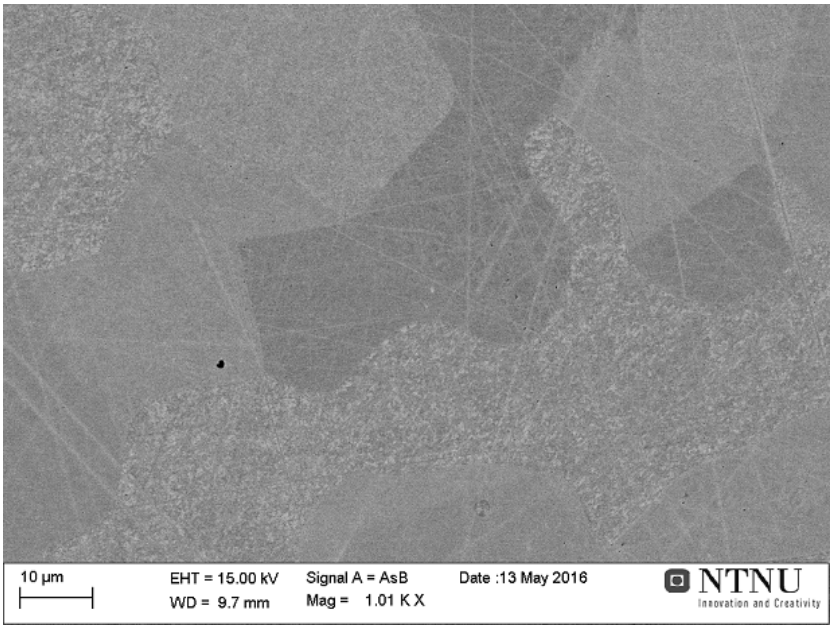

Figure 4.1: Microstructure of a sample after solution annealing at 1110°C for 15 minutes.

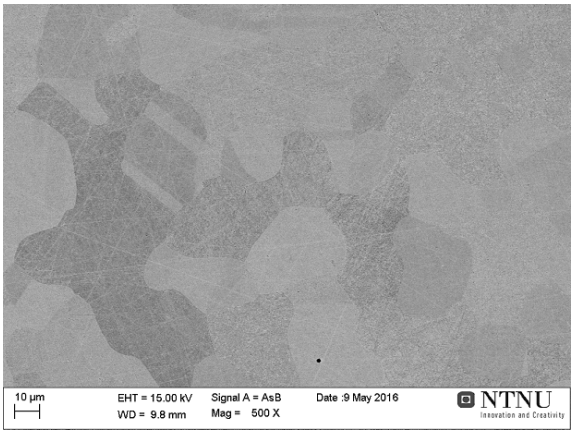

(a) The microstructure is similar to the solution annealed condition.

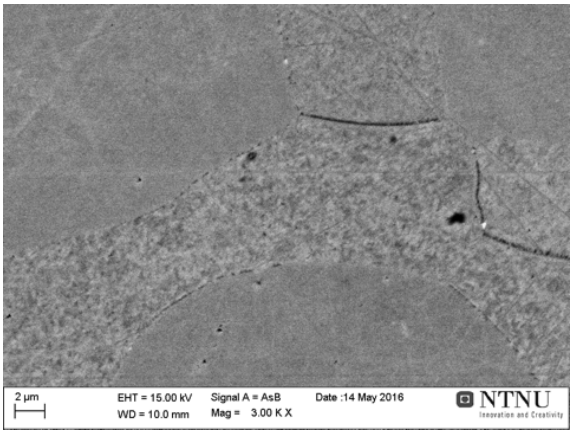

(b) Nucleation of the χ - phase at grain boundaries.

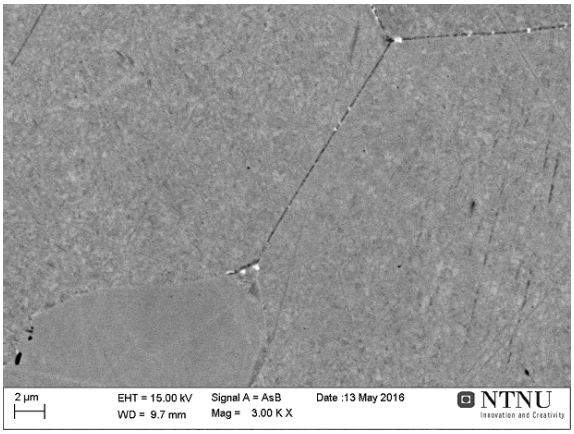

(c) Propagation of the χ - phase at grain boundaries.

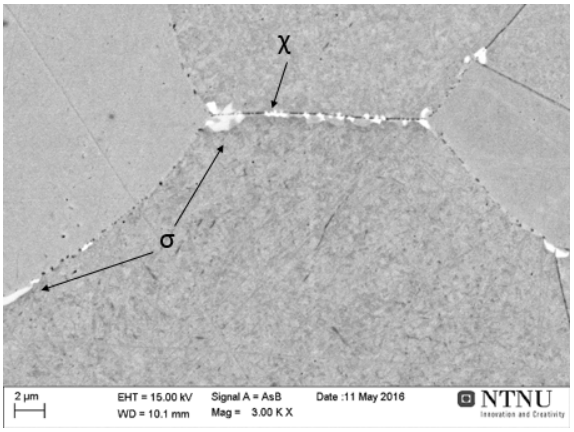

(d) Initiation of σ - phase, resulting in formation of γ_2.

Figure 4.2: Microstructures of samples after isothermal heat treatment at 870°C for a) 1 minute, b) 1,5 minutes, c) 2 minutes and d) 4 minutes. A higher amount of χ - and σ - phase with increasing isothermal heat treatment time can be observed.

The relative amount of alloying elements in ferrite and austenite in solution annealed condition was determined by energy dispersive spectroscopy (EDS), and is given in Table 4.1.

Table 4.1: Relative amount of alloying elements in ferrite and austenite in solution annealed condition.

Phase	**Fe**	**Cr**	**Ni**	**Mo**	**W**
Ferrite	61,4	25,3	5,4	3,3	0,5
Austenite	62,3	21,8	8,7	1,9	0,3

The marked areas in Figure 4.2d, was determined to be χ - and σ - phase by EDS, and the relative amount of alloying elements in the χ - and σ - phase after isothermal heat treatment at 870°C for 4 minutes is given in Table 4.2.

Table 4.2: Relative amount of alloying elements in the χ - and σ - phase after isothermal heat treatment at 870°C for 4 minutes.

Phase	**Fe**	**Cr**	**Ni**	**Mo**	**W**
χ	56,0	25,9	4,7	8,7	1,8
σ	57,8	28,4	4,8	5,3	0,86

The microstructure of a sample heat treated at 870°C for 10 minutes was characterized by electron backscattered diffraction (EBSD) in SEM, and found to contain a volume fraction of 0,541 ferrite, 0,432 austenite and 0,027 σ - phase. Determination of volume fraction of intermetallic precipitates and secondary phases after the other isothermal heat treatments will be done in another project work.

The microstructures after isothermal heat treatment at 820°C for 4 and 20 minutes, are shown in Figure 4.3a - 4.3d. The microstructures of samples heat treated at this temperature, seem to contain chromium nitrides at low IHt and higher amount of σ - phase with increasing IHt.

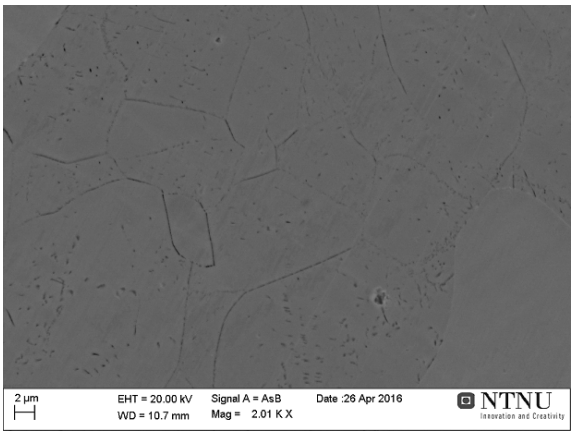

(a) Intergranular and intragranular precipitations.

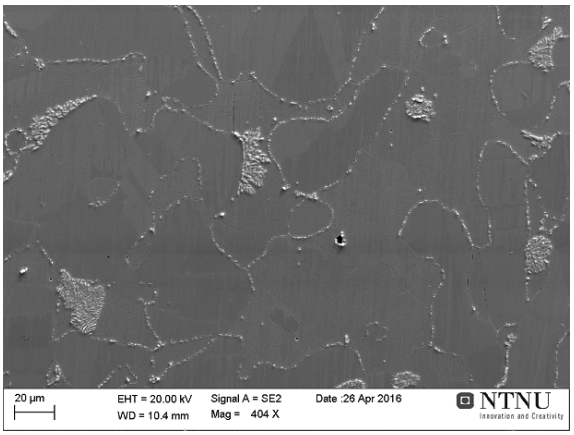

(b) Increased amount of both the χ - and σ - phase.

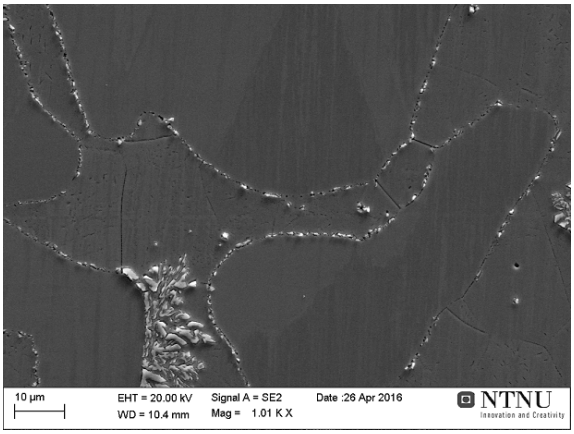

(c) Precipitation and propagation of the χ - and σ - phase.

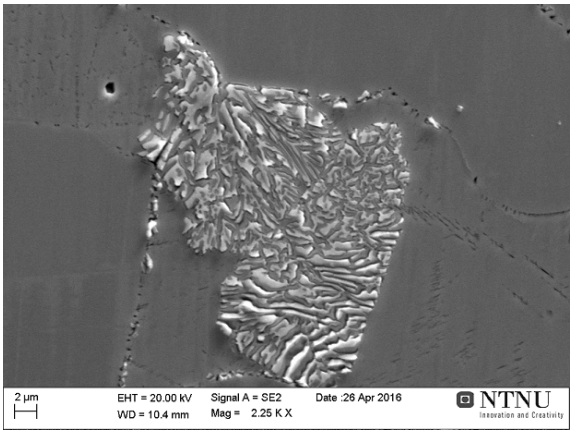

(d) Morphology of the σ - phase and formation of γ_2.

Figure 4.3: Figure a) shows the microstructure of a sample isothermal heat treated at 820 °C for 4 minutes. Figure b) - d) show the microstructure of a sample isothermal heat treated at 820 °C for 20 minutes at several magnifications.

The microstructures after isothermal heat treatment at 940°C for 2 and 4 minutes, are shown in Figure 4.4a - 4.4d.

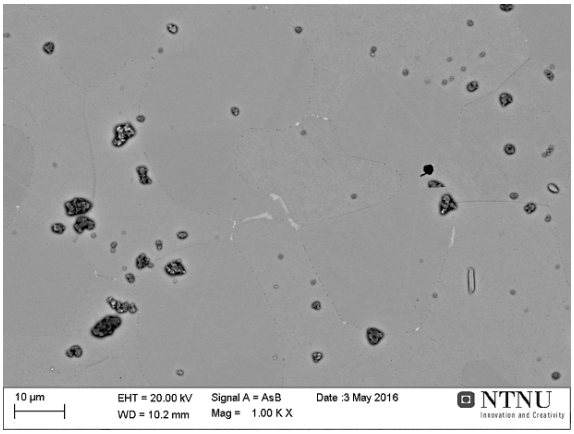

(a) Precipitation at grain boundaries.

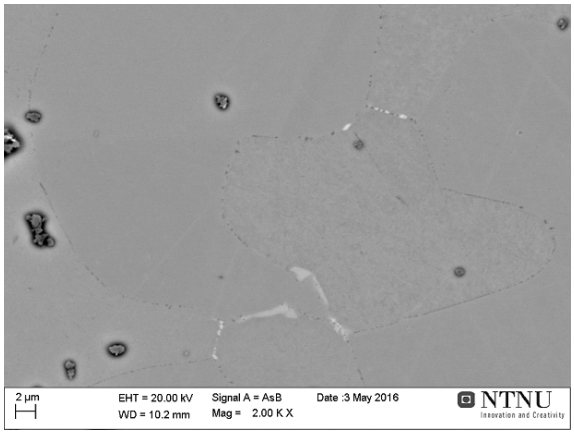

(b) Precipitation at grain boundaries.

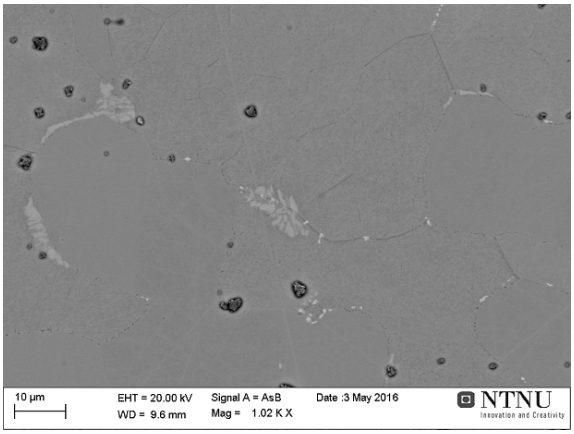

(c) Precipitation of the χ - and σ - phase.

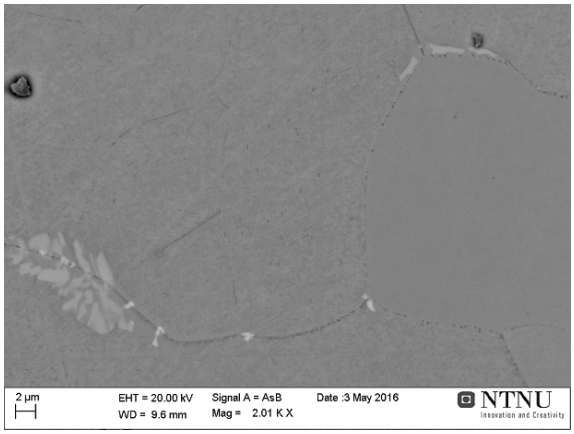

(d) Morphology of the χ - and σ - phase.

Figure 4.4: Figure a) - b) show the microstructure of a sample isothermal heat treated at 940 °C for 2 minutes. Figure c) - d) show the microstructure of a sample isothermal heat treated at 940 °C for 4 minutes.

4.2 Critical pitting temperature measurements

CPT was determined from a modified ASTM G48 method, by OCP and temperature measurements, when OCP dropped below 500 mV_{SCE}, as described in Section 3.3.2. Examples of OCP and temperature measurements of sample 1.3 - 1.10, are given in Figure 4.5a - 4.5d. The rest can be found in Appendix B. Values of CPT are given in Table 4.3. The results in this section are given according to the test matrix in Table 3.4.

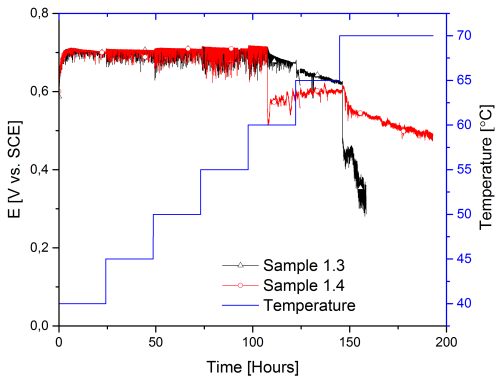

(a) Sample 1.3 and 1.4.

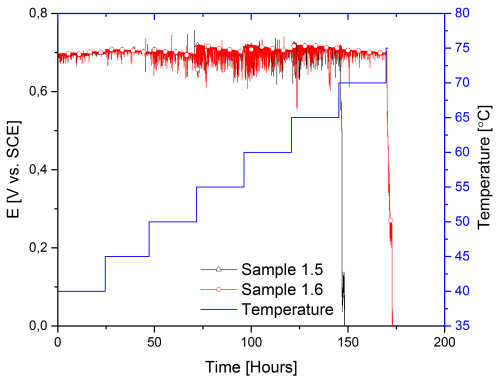

(b) Sample 1.5 and 1.6.

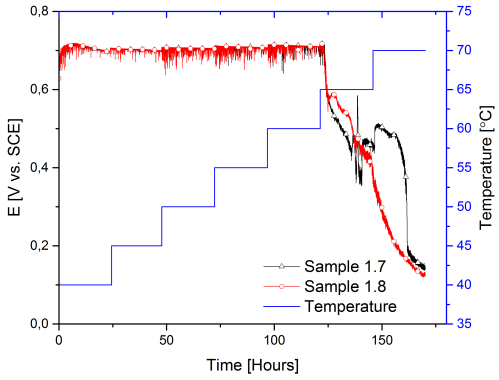

(c) Sample 1.7 and 1.8.

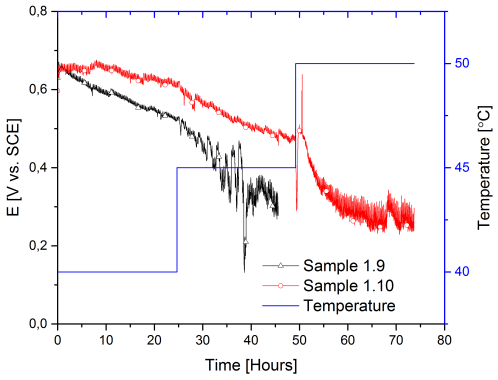

(d) Sample 1.9 and 1.10.

Figure 4.5: CPT measurements of sample 1.3 - 1.10.

Table 4.3: CPT as a function of heat treatments.

Sample number	**Isothermal heat treatment**	**CPT [°C]**
1.1	S.A.	80
1.2	S.A.	75
1.3	T1t1	70
1.4	T1t1	70
1.5	T1t2	70
1.6	T1t2	75
1.7	T1t3	65
1.8	T1t3	65
1.9	T1t4	45
1.10	T1t4	45
1.11	T2t1	65
1.12	T2t1	65
1.13	T2t2	65
1.14	T2t2	65
1.15	T2t3	55
1.16	T2t3	55
1.17	T2t5	Below 40
1.18	T2t5	Below 40
1.19	T3t1	70
1.20	T3t1	70
1.21	T3t2	70
1.22	T3t2	70
1.23	T3t3	65
1.24	T3t3	60
1.25	T3t5	Below 40
1.26	T3t5	Below 40

The CPT values were used to determine a critical IHt at a given isothermal heat treatment temperature. A sudden drop in CPT as a function of IHt indicates a reduction in the pitting corrosion resistance. CPT was generally observed to decrease with increasing IHt, for a given isothermal heat treatment temperature. CPT as a function of IHt of samples heat treated at 870°C, 820°C and 940°C, are shown in Figure 4.6 - 4.8, respectively.

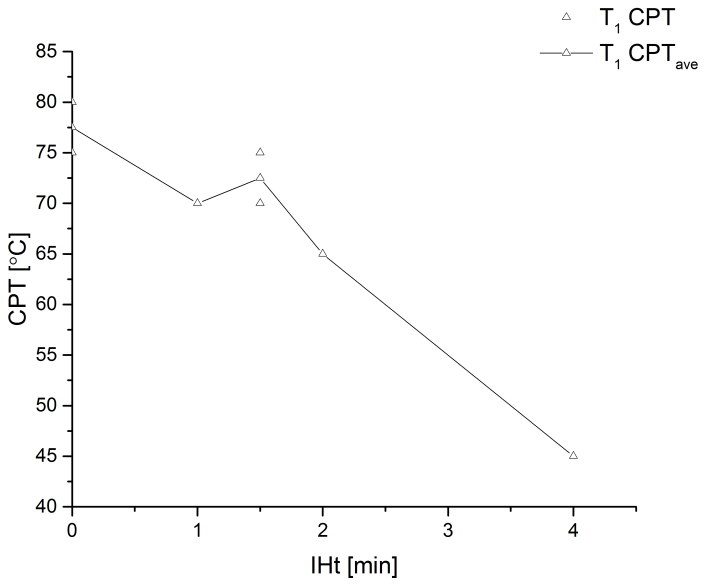

Figure 4.6: CPT as a function of IHt for samples isothermal heat treated at temperature T_1 (870°C). CPT of solution annealed samples are included for comparison (IHt = 0).

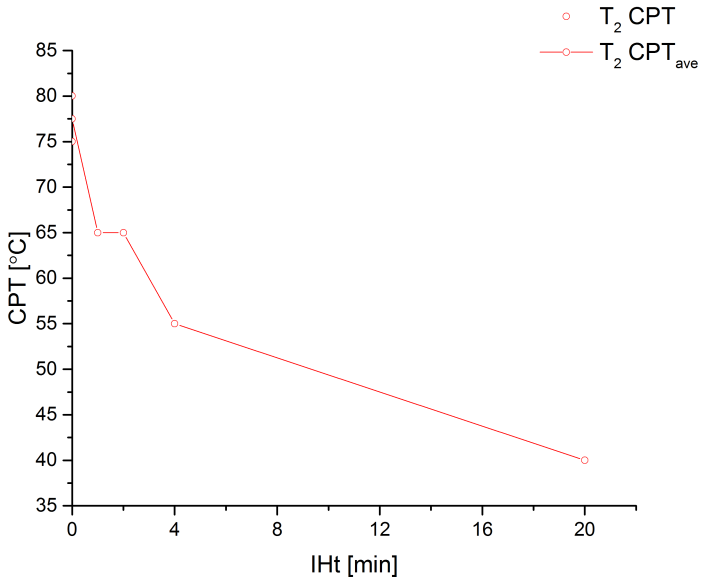

Figure 4.7: CPT as a function of IHt for samples isothermal heat treated at temperature T_2 (820°C). CPT of solution annealed samples are included for comparison (IHt = 0).

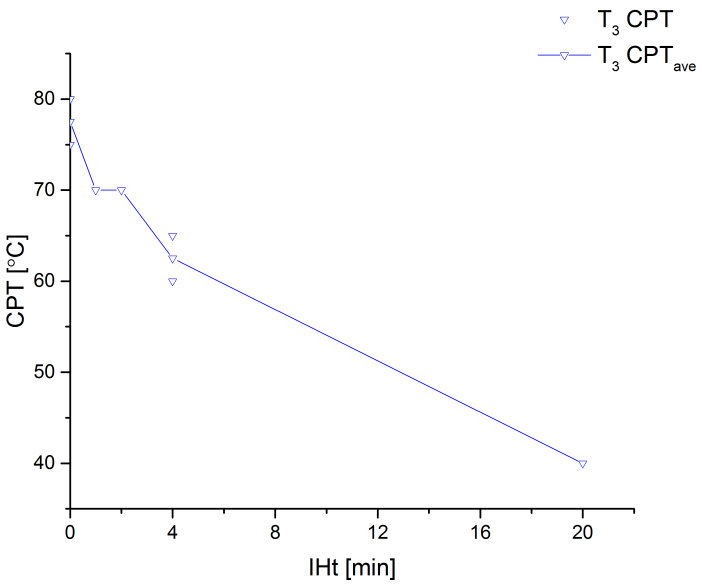

Figure 4.8: CPT as a function of IHt for samples isothermal heat treated at temperature T_3 (940°C). CPT of solution annealed samples are included for comparison (IHt = 0).

CPT as a function of IHT, for samples heat treated for 1, 2 and 4 minutes, are shown in Figure 4.9 - 4.11, respectively, and are called corrosion maps further in this work. CPT was observed to depend on IHT for a given isothermal heat treatment time.

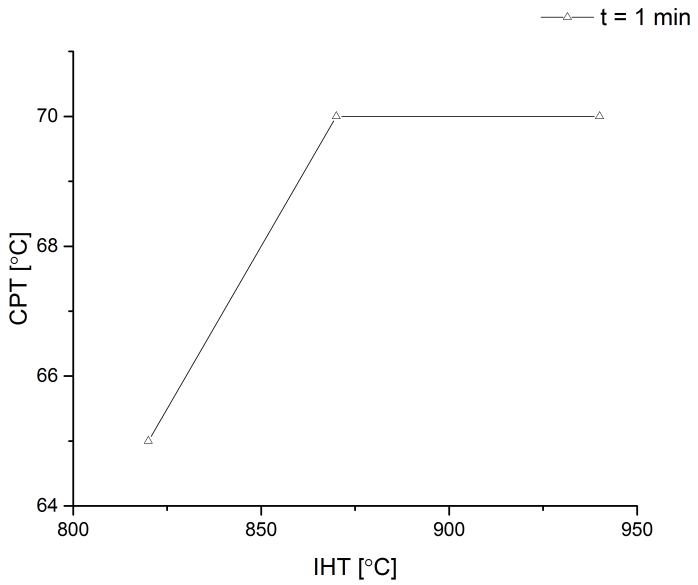

Figure 4.9: CPT as a function of IHT for samples heat treated for 1 minute.

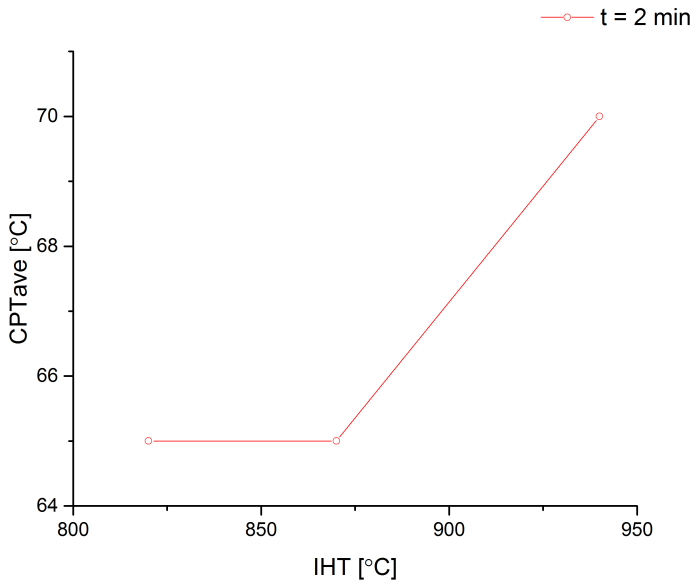

Figure 4.10: CPT as a function of IHT for samples heat treated for 2 minutes.

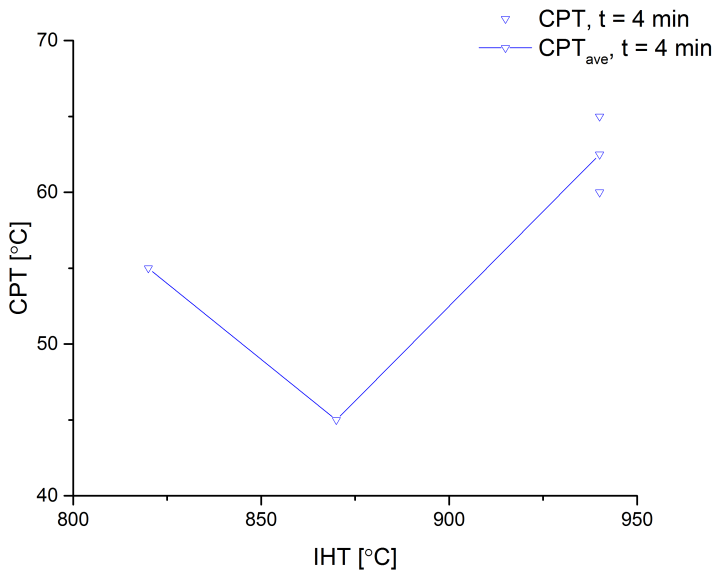

Figure 4.11: CPT as a function of IHT for samples heat treated for 4 minutes.

4.3 Anodic cyclic potentiodynamic polarization curves

This section presents some of the ASTM G61 anodic CPP curves, of some samples from the test matrix in Table 3.6. The rest can be found in Appendix E. Values of the parameters obtained from anodic CPP curves, OCP, E_p, E_{RP}, i_p are also given in this section. All anodic CPP curves obtained at 40°C contained no hysteresis. This was also generally the case for anodic CPP curves obtained at 60°C, with some exceptions that contained a little hysteresis. All anodic CPP curves obtained at 80°C contained a hysteresis. The anodic CPP curves of sample 2.9 - 2.12, heat treated at 870°C for 1 minute, are shown in Figure 4.12 - 4.13.

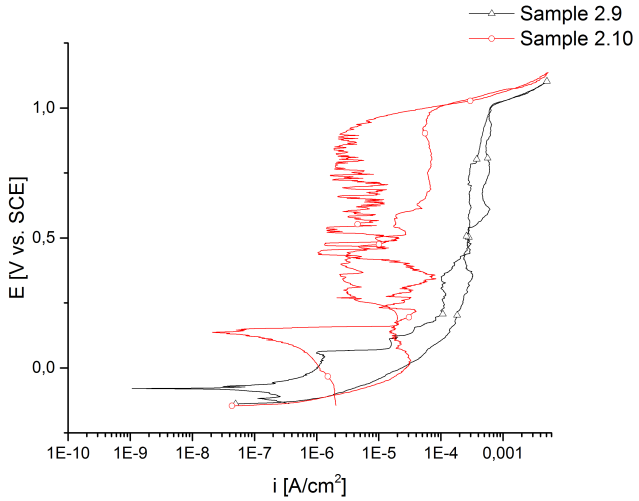

Figure 4.12: Anodic CPP curves of sample 2.9 and 2.10, heat treated at 870°C for 1 minute. The curves were recorded with an electrolyte temperature of 60 °C.

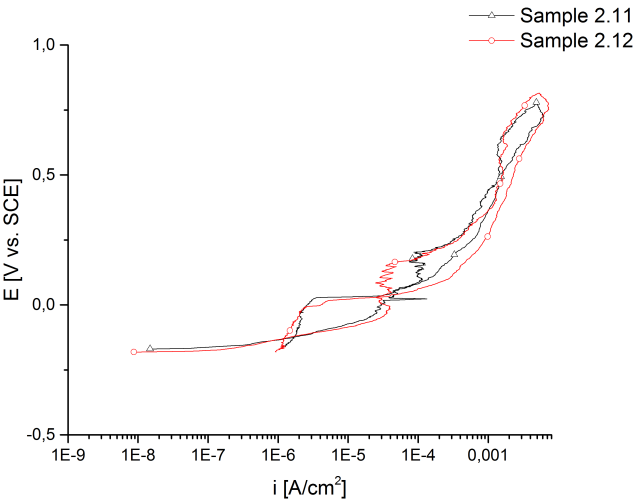

Figure 4.13: Anodic CPP curves of sample 2.11 and 2.12, heat treated at 870°C for 1 minute. The curves were recorded with an electrolyte temperature of 80 °C.

The anodic CPP curves of sample 2.13 - 2.14, heat treated at 870°C for 1,5 minutes, are shown in Figure 4.14. The anodic CPP curves of sample 2.31 - 2.36, heat treated at 940°C for 4 minutes, are shown in Figure 4.15 - 4.17.

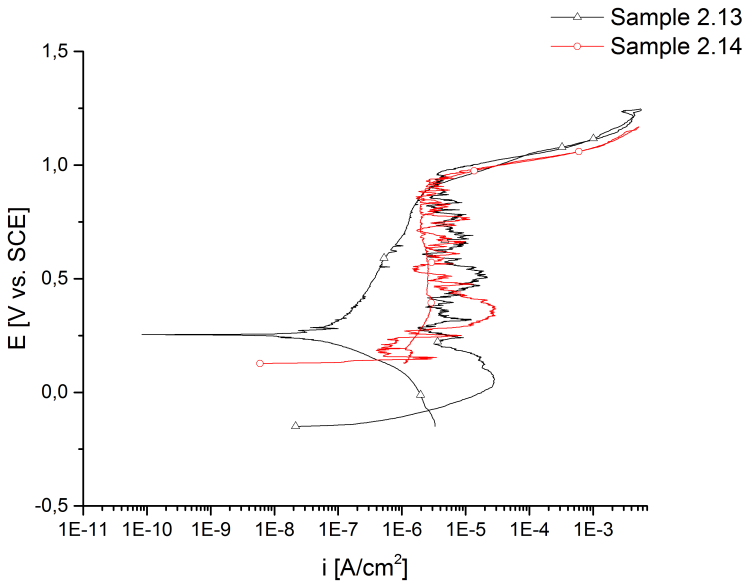

Figure 4.14: Anodic CPP curves of sample 2.13 and 2.14, heat treated at 870°C for 1,5 minutes. The curves were recorded with an electrolyte temperature of 40 °C.

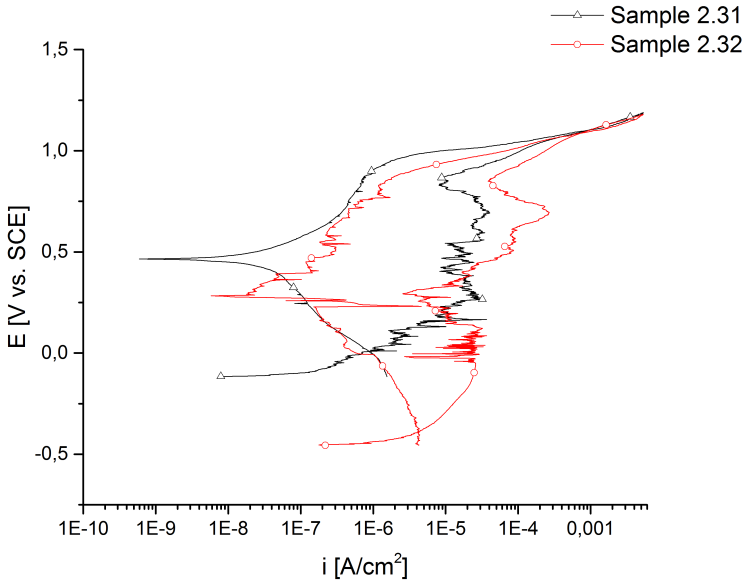

Figure 4.15: Anodic CPP curves of sample 2.31 and 2.32, heat treated at 940°C for 4 minutes. The curves were recorded with an electrolyte temperature of 40 °C.

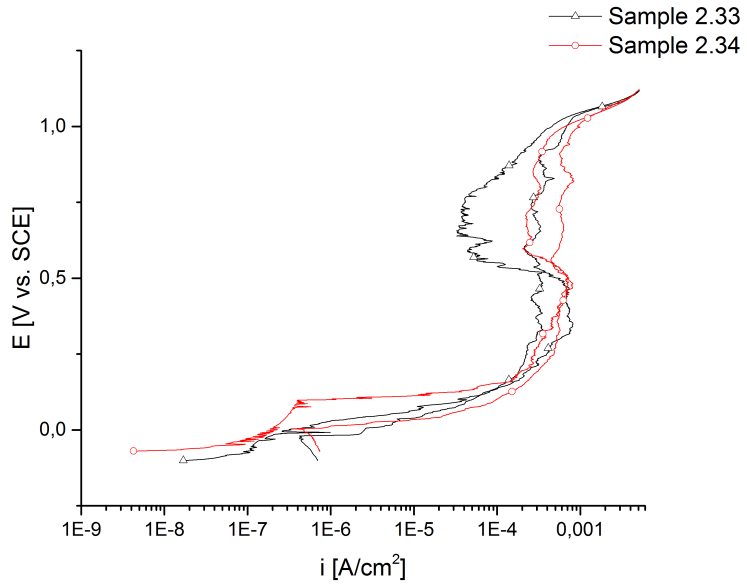

Figure 4.16: Anodic CPP curves of sample 2.33 and 2.34, heat treated at 940°C for 4 minutes. The curves were recorded with an electrolyte temperature of 60 °C.

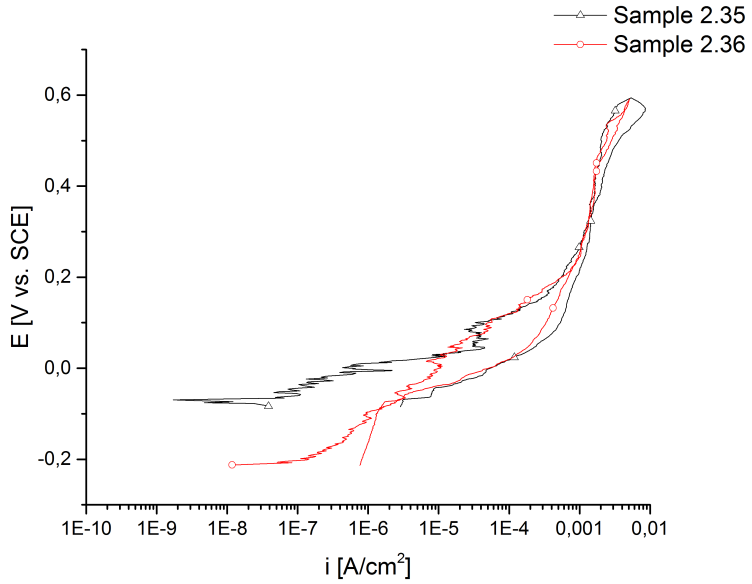

Figure 4.17: Anodic CPP curves of sample 2.35 and 2.36, heat treated at 940°C for 4 minutes. The curves were recorded with an electrolyte temperature of 80 °C.

The parameters, OCP, E_p, E_{RP} and i_p obtained from anodic CPP curves for samples in the test matrix in Table 3.6, are given in Table 4.4 - 4.9.

Table 4.4: Parameters obtained from anodic CPP curves of solution annealed samples 2.1 - 2.6.

Sample number	**OCP** [V_{SCE}]	E_p [V_{SCE}]	E_{RP} [V_{SCE}]	i_p [$\mu A/cm^2$]
2.1	-0,1032	0,9250	0,9350	0,3382
2.2	0,05070	0,9600	0,9800	0,2438
2.3	0,04445	0,9223	0,8357	0,3215
2.4	-0,04154	0,9223	0,9512	0,4398
2.5	-0,04377	0,07385	-0,02334	0,2411
2.6	0,01848	0,2114	0,02716	0,3748

Table 4.5: Parameters obtained from anodic CPP curves of samples 2.7 - 2.12, heat treated at 870°C for 1 minute.

Sample number	**OCP** [V_{SCE}]	E_p [V_{SCE}]	E_{RP} [V_{SCE}]	i_p [$\mu A/cm^2$]
2.7	0,09812	0,9424	0,9221	1,4984
2.8	-0,11081	0,9355	0,9221	3,4505
2.9	-0,13831	0,9801	0,06537	-
2.10	-0,14549	0,9512	0,8502	4,4254
2.11	-0,16887	0,2050	-0,1180	86,56
2.12	-0,18107	0,1706	-0,1180	34,48

Table 4.6: Parameters obtained from anodic CPP curves of samples 2.13 - 2.17, heat treated at 870°C for 1,5 minutes.

Sample number	**OCP** [V_{SCE}]	E_p [V_{SCE}]	E_{RP} [V_{SCE}]	i_p [$\mu A/cm^2$]
2.13	-0,1496	0,9573	0,8656	4,1924
2.14	0,12744	0,9454	0,8656	3,029
2.15	-0,10659	0,9457	0,1698	-
2.16	-0,12545	0,9690	0,8722	2,2067 and 26,577
2.17	-0,18887	0,1176	0,1116	28,666

Table 4.7: Parameters obtained from anodic CPP curves of samples 2.19 - 2.24, heat treated at 870°C for 2 minutes.

Sample number	**OCP** [$\mathbf{V}_{SCE}$]	$\mathbf{E}_p$ [$\mathbf{V}_{SCE}$]	$\mathbf{E}_{RP}$ [$\mathbf{V}_{SCE}$]	$\mathbf{i}_p$ [$\mu\mathbf{A/cm^2}$]
2.19	-0,16929	0,9548	0,8894	3,5147
2.20	-0,14149	0,9548	0,9522	3,5147
2.21	-0,05038	0,9701	0,7384	2,678
2.22	-0,14561	0,9657	0,8775	1,878
2.23	-0,23913	0,2716	-0,006367	3,4972
2,24	-0,23649	-0,1617	-0,02419	0,5434

Table 4.8: Parameters obtained from anodic CPP curves of samples 2.25 - 2.30, heat treated at 820°C for 4 minutes.

Sample number	**OCP** [$\mathbf{V}_{SCE}$]	$\mathbf{E}_p$ [$\mathbf{V}_{SCE}$]	$\mathbf{E}_{RP}$ [$\mathbf{V}_{SCE}$]	$\mathbf{i}_p$ [$\mu\mathbf{A/cm^2}$]
2.25	-0,18806	0,7657	1,004	0,4243 and 3,1198
2.26	-0,005500	0,7982	0,944	0,5874 and 6,2138
2.27	-0,04803	0,2755	0,06324	0,2749
2.28	-0,09958	0,7517	0,1897	0,4398 and 2,8962
2.29	-0,1268	-0,0308998	-	0,1728 and
2,30	-0,19486	-0,01420	-0,0841	0,3596 and

Table 4.9: Parameters obtained from anodic CPP curves of samples 2.31 - 2.36, heat treated at 940°C for 4 minutes.

Sample number	**OCP** [$\mathbf{V}_{SCE}$]	$\mathbf{E}_p$ [$\mathbf{V}_{SCE}$]	$\mathbf{E}_{RP}$ [$\mathbf{V}_{SCE}$]	$\mathbf{i}_p$ [$\mu\mathbf{A/cm}^2$]
2.31	-	0,8697	0,9544	11,237
2.32	-0,45587	0,8697	0,8729	21,686
2.33	-0,10196	0,7632	-0,01613	0,1338 and 37,266
2.34	-0,07060	0,6515	0,01273	0,3522
2.35	-0,08454	0,007583	-	0,1214 and 33,066
2,36	-0,21332	-0,09853	-0,07448	0,4876 and 47,725

E_p is presented as a function of IHt for the three ASTM G61 electrolyte test temperatures 40°C, 60°C and 80°C, in Figure 4.18 - 4.20, respectively. The results for solution annealed samples were also included for comparison (IHt = 0). E_p generally decreased from solution annealed condition to isothermal heat treated condition at 820°C and 940°C for 4 minutes.

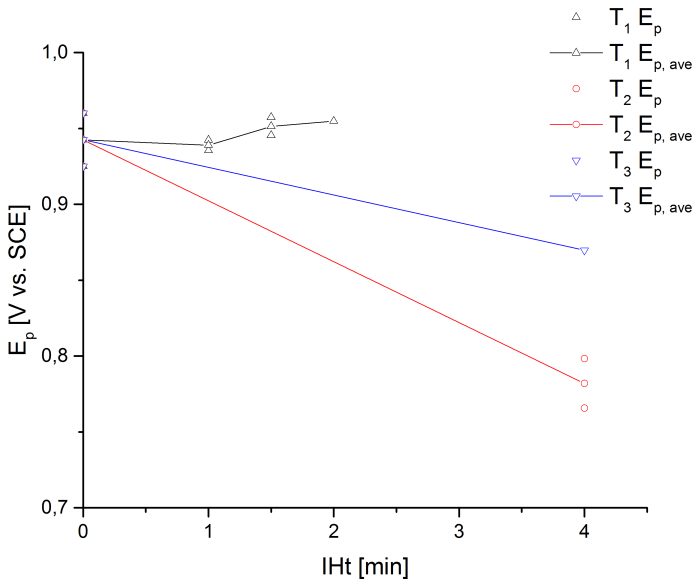

Figure 4.18: E_p as a function of IHt for samples, that was anodic cyclic potentiodynamic polarized, with an electrolyte test temperature of 40 °C.

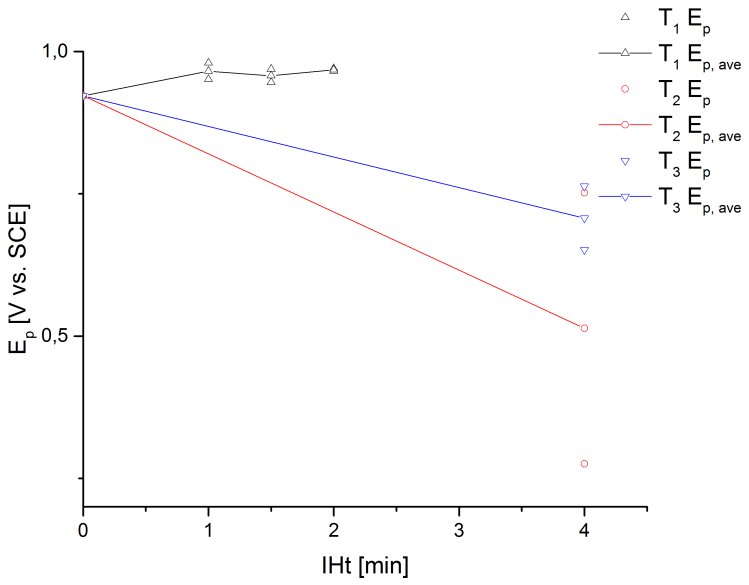

Figure 4.19: E_p as a function of IHt for samples, that was anodic cyclic potentiodynamic polarized, with an electrolyte test temperature of 60 °C.

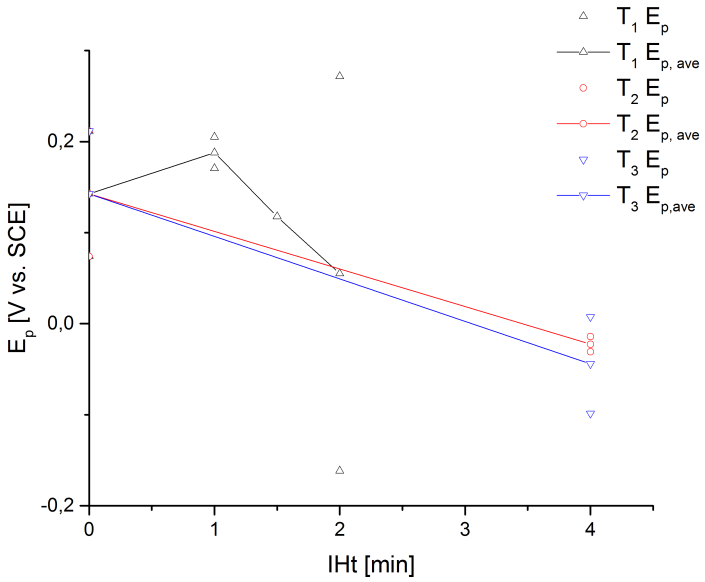

Figure 4.20: E_p as a function of IHt for samples, that was anodic cyclic potentiodynamic polarized, with an electrolyte test temperature of 80 °C.

4.4 Surface characterization after electrochemical measurements

This section presents surface characterization of samples after electrochemical measurements, and are divided into modified ASTM G48 CPT measurements and ASTM G61 anodic CPP measurements.

4.4.1 After critical pitting temperature measurements

Several samples from CPT measurements, with the modified ASTM G48 method, showed major weight loss from corrosion, which generally increased with increasing IHt for a given isothermal heat treatment temperature. The surface characterization of samples in this section is in accordance with the test matrix in Table 3.4. Surface characterization by 3D OM at a magnification of 2,5X of sample 1.12 - 1.17 are shown in Figure 4.21a - 4.21f, respectively. The rest can be found in Appendix C.

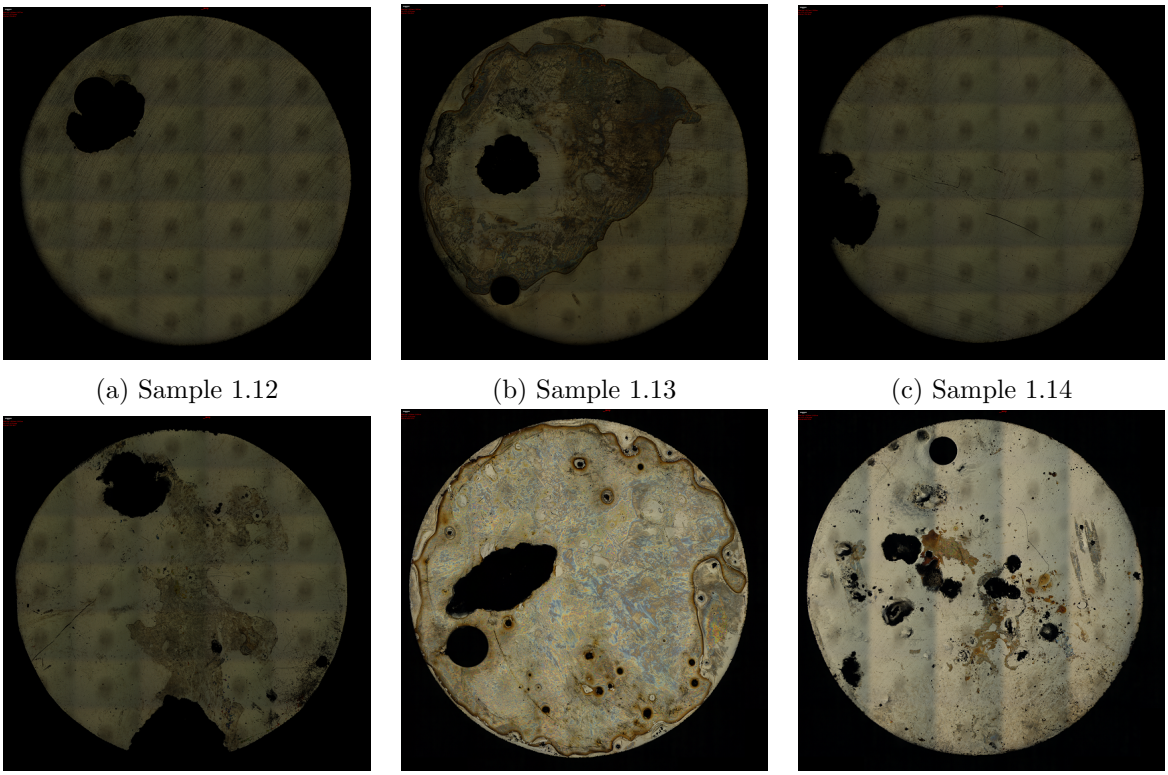

(a) Sample 1.12 (b) Sample 1.13 (c) Sample 1.14

(d) Sample 1.15 (e) Sample 1.16 (f) Sample 1.17

Figure 4.21: Surface characterization by 3D OM with a magnification of 2,5X.

Surface characterization of the microstructure of some samples after CPT measurements are shown in Figure 4.22 - 4.23. Corrosion on edges was observed for several of the samples, and some examples of this is shown for sample 1.4 and 1.9 in Figure 4.24.

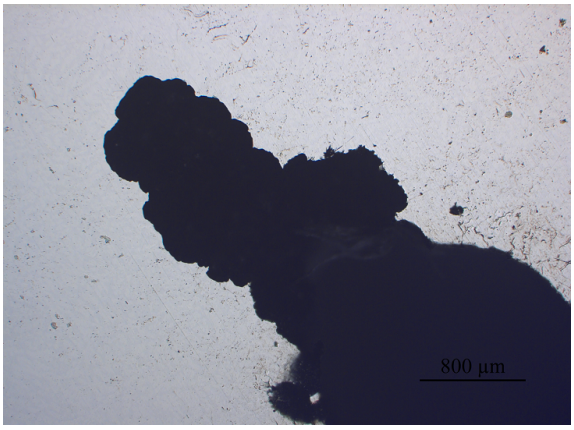

(a) Sample 1.6, magnification 2,5X.

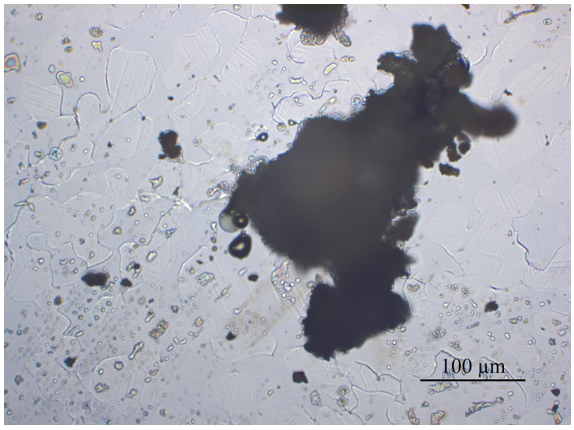

(b) Sample 1.7, magnification 20X.

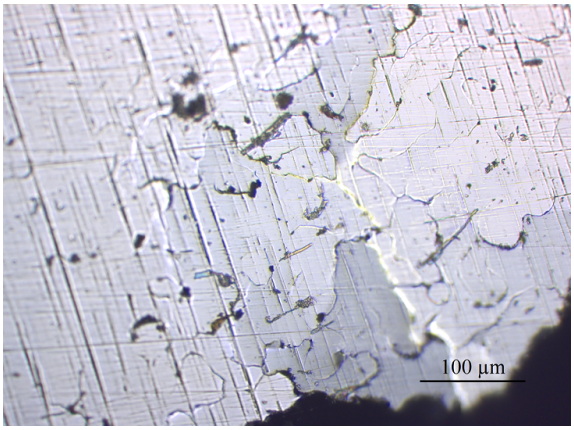

(c) Sample 1.8, magnification 20X.

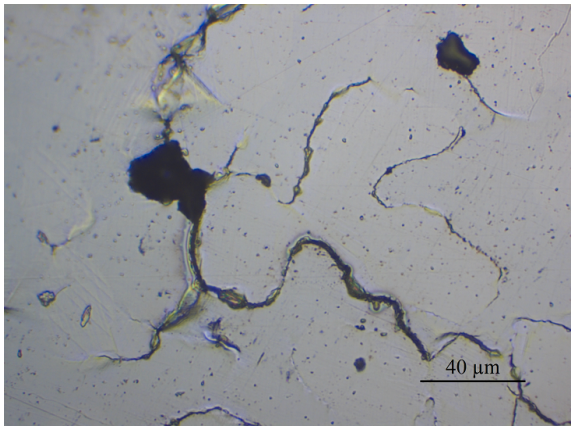

(d) Sample 1.10, magnification 50X.

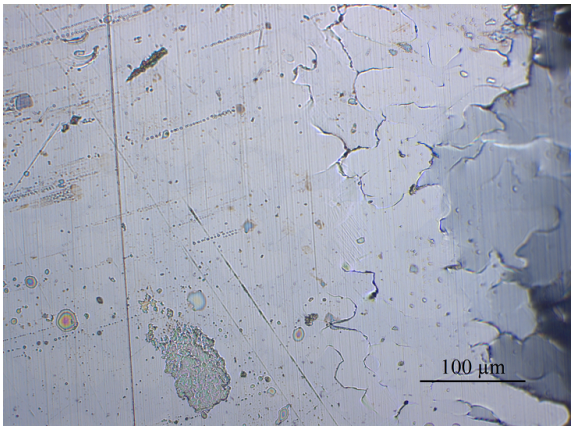

(e) Sample 1.16, magnification 20X.

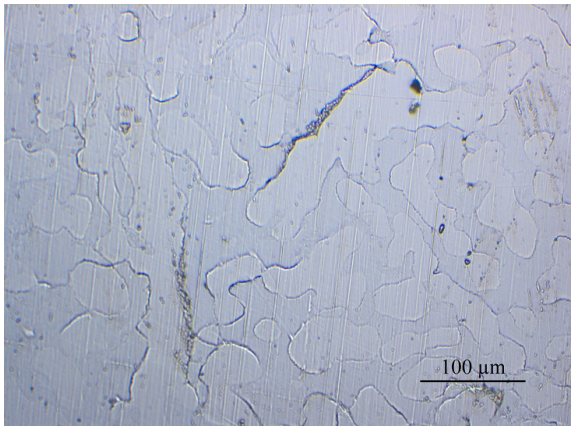

(f) Sample 1.17, magnification 20X.

Figure 4.22: Surface characterization by OM of selected samples, after CPT measurements.

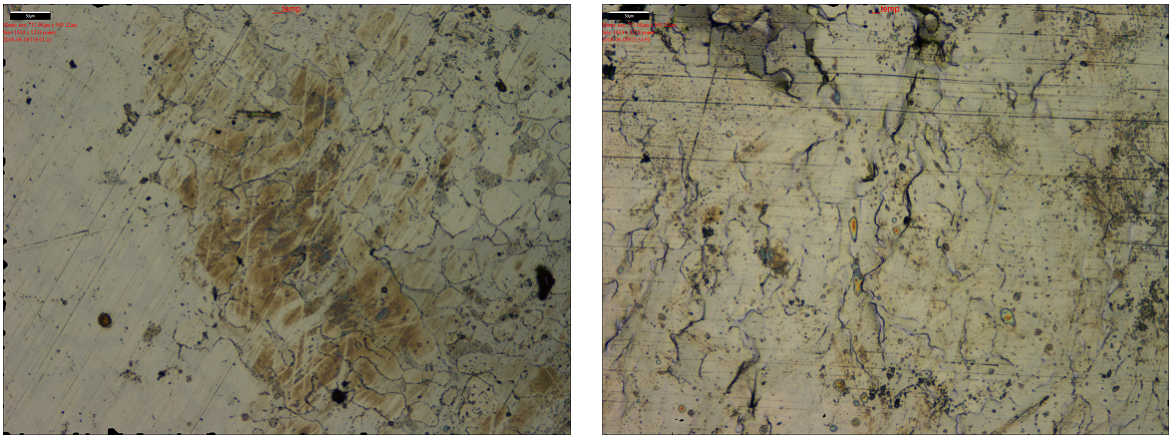

(a) Sample 1.17, magnification 20X.

(b) Sample 1.24, magnification 20X.

Figure 4.23: Surface characterization by 3D OM of sample 1.17 and 1.24 after CPT measurements.

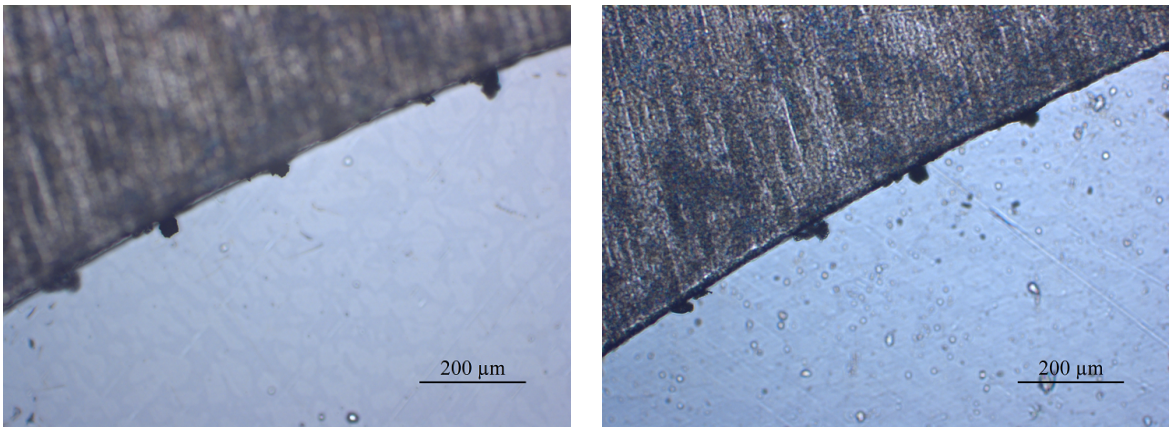

(a) Sample 1.4, magnification 10X.

(b) Sample 1.9, magnification 10X.

Figure 4.24: Surface characterization by OM of sample 1.4 and 1.9 after CPT measurements, showing corrosion on edges.

4.4.2 After anodic cyclic potentiodynamic polarization measurements

For samples with no hysteresis in the anodic CPP curve, indicating no pitting corrosion, the anodic dissoluted areas were investigated by 3D OM. Examples of anodic dissolution areas of sample 2.2, 2.10 and 2.27 are shown in Figure 4.25a - 4.25d. The dark phase is ferrite and the bright phase is austenite.

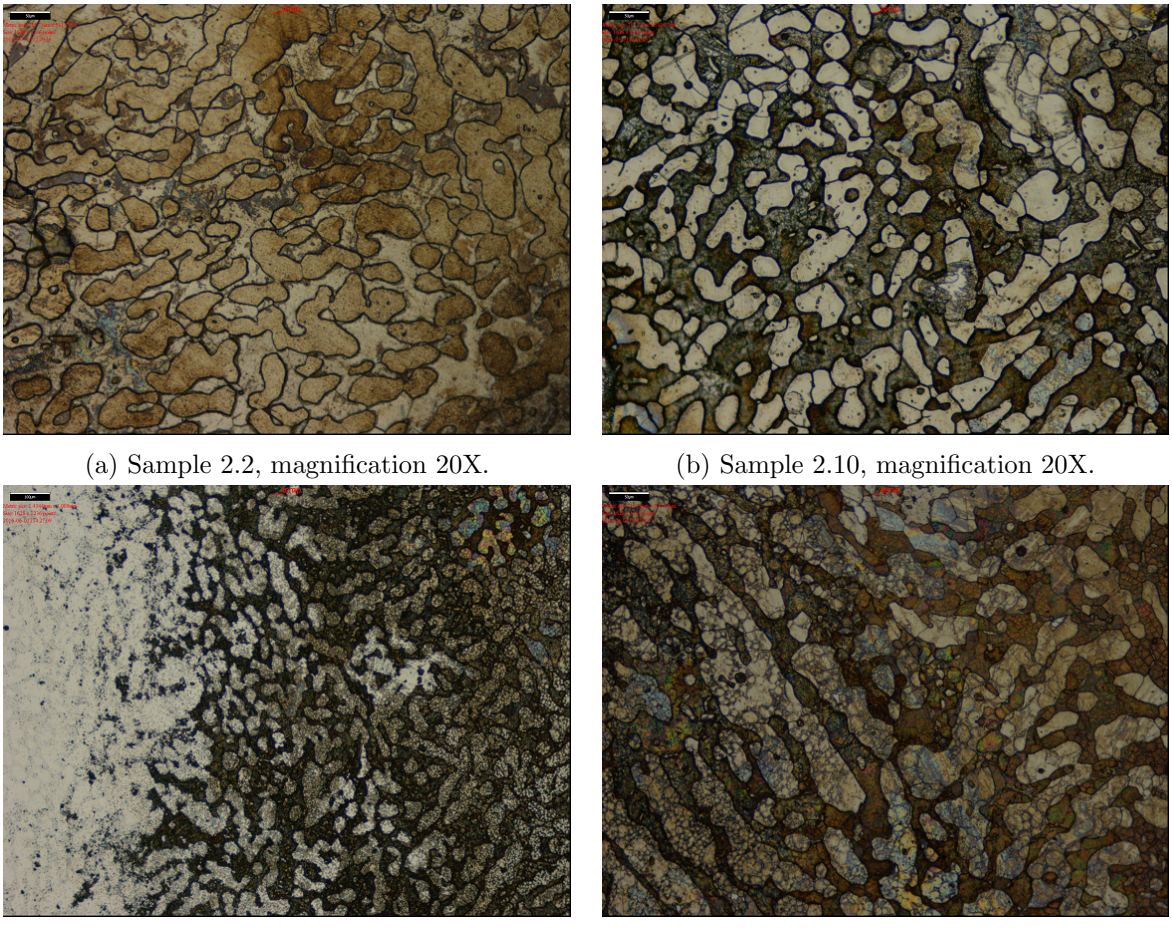

(a) Sample 2.2, magnification 20X.

(b) Sample 2.10, magnification 20X.

(c) Sample 2.27, magnification 10X.

(d) Sample 2.27, magnification 20X.

Figure 4.25: Surface characterization by 3D OM of sample 2.2, 2.10 and 2.27 after anodic CPP, showing anodic dissolution. The dark phase is ferrite and the bright phase is austenite.

Surface characterization by 3D OM of some samples with an anodic CPP curve that contained a hysteresis, are shown in Figure 4.26a - 4.26f.

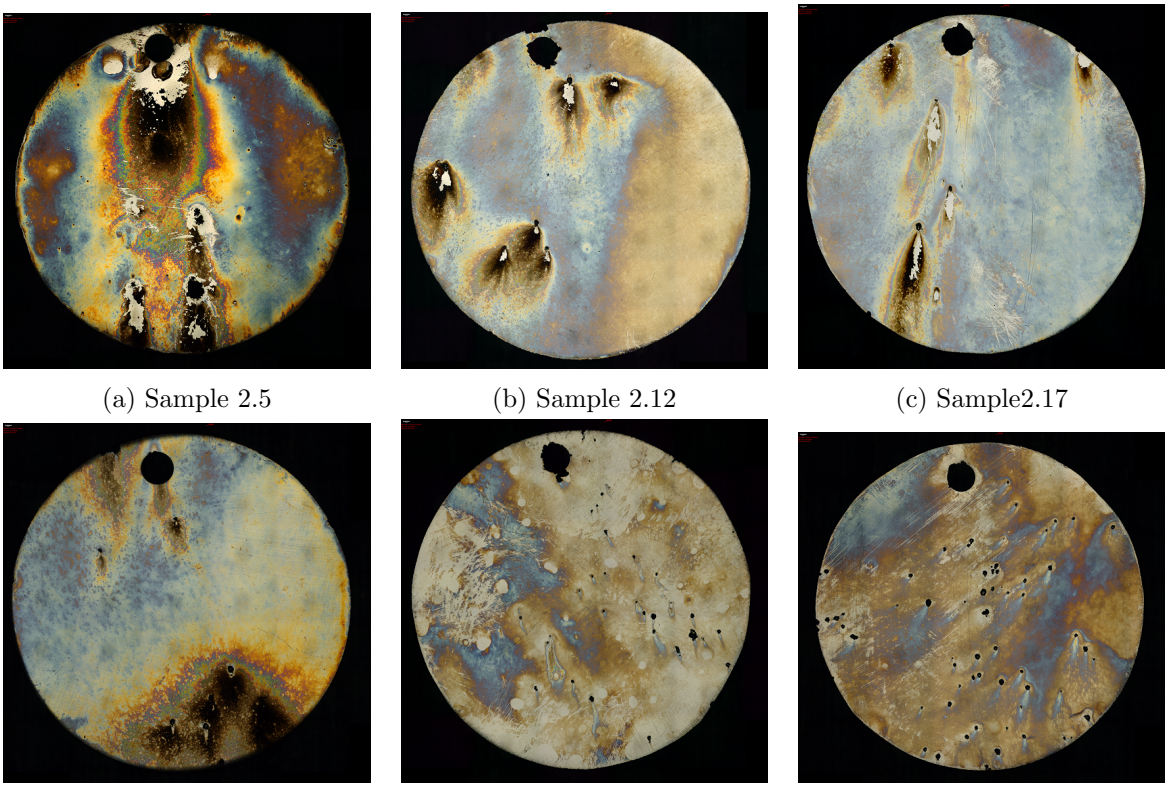

(a) Sample 2.5 (b) Sample 2.12 (c) Sample2.17

(d) Sample 2.23 (e) Sample 2.29 (f) Sample 2.35

Figure 4.26: Surface characterization by 3D OM with a magnification of 2,5X of samples after anodic CPP.

The depth and width was measured for three pits for three samples in Figure 4.26 after anodic CPP, and are given in Table 4.10. The pit depth and width measurements are given in Appendix G61Surfacecharacterization.

Table 4.10: Depth and width of three pits on the surface of sample 2.5, 2.29 and 2.35.

Sample number	**Average pit depth [μm]**	**Average pit width [μm]**
2.5	131,07	776,45
2.29	19,218	150,98
2.35	16,831	205,43

The pitting morphology was investigated by 3D OM. Surface characterization of sample 2.5, 2.29 and 2.35 by 3D OM are shown in Figure 4.27 - 4.31, respectively.

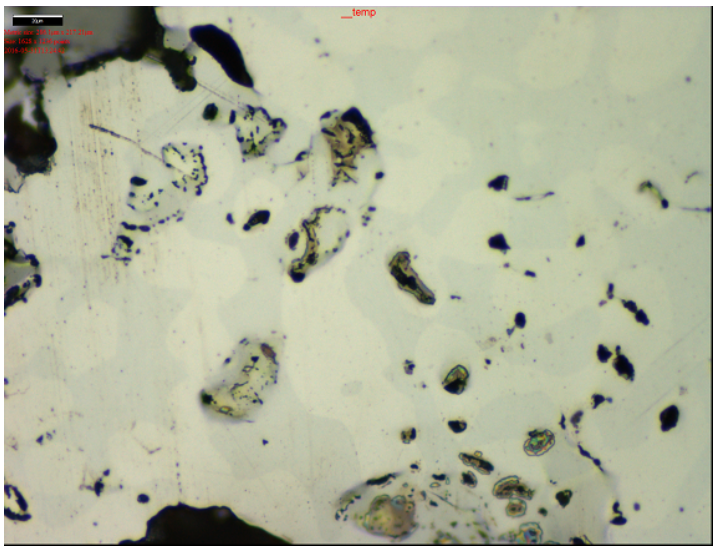

Figure 4.27: Surface characterization by 3D OM of sample 2.5 after anodic CPP. A magnification of 50X was used.

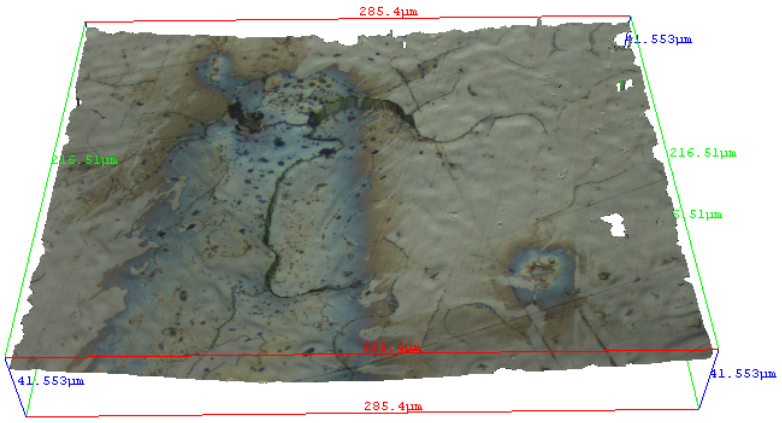

Figure 4.28: Surface characterization by 3D OM of sample 2.29, after anodic CPP. A magnification of 50X was used.

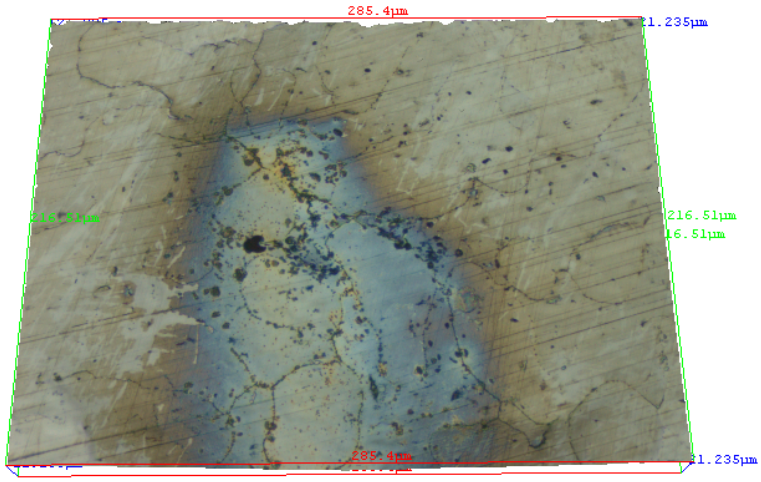

Figure 4.29: Surface characterization by 3D OM of sample 2.29 after anodic CPP. A magnification of 50X was used.

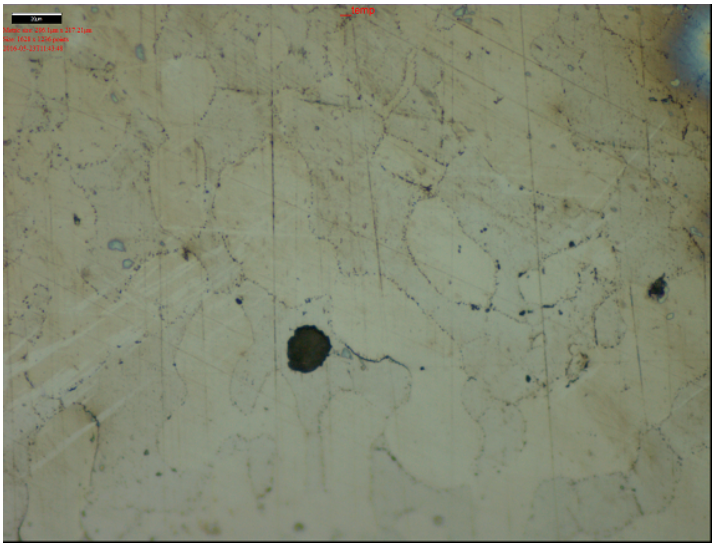

Figure 4.30: Surface characterization by 3D OM of sample 2.35 after anodic CPP. A magnification of 50X was used.

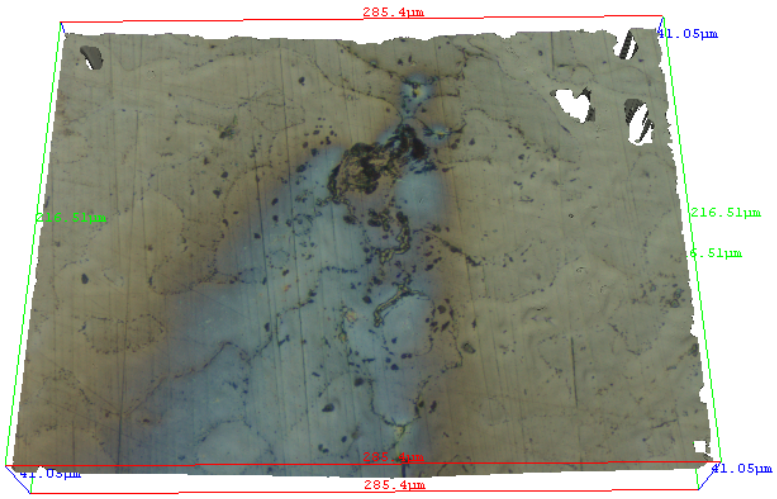

Figure 4.31: Surface characterization by 3D OM of sample 2.35, after anodic CPP. A magnification of 50X was used.

Surface characterization of sample 2.35, isothermal heat treated at 940°C for 4 minutes tested at an electrolyte temperature of 80°C, was investigated in SEM in cooperation with another master student. This is shown in Figure 4.32a - 4.32d.

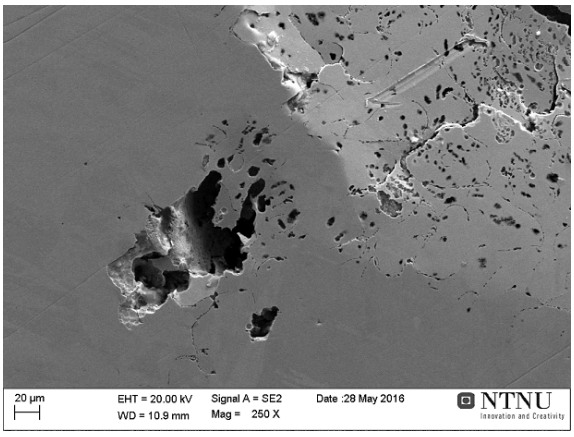

(a) Sample 2.35, magnification 250X.

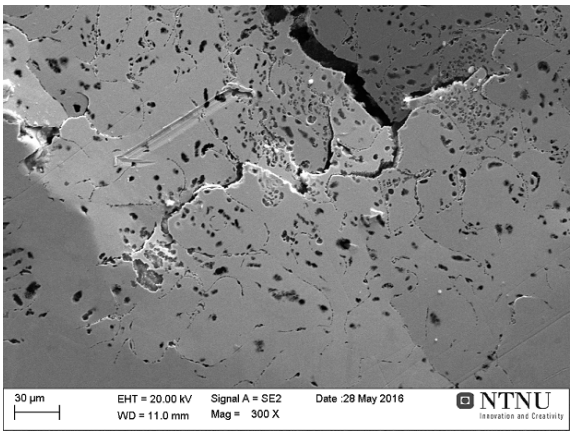

(b) Sample 2.35, magnification 300X.

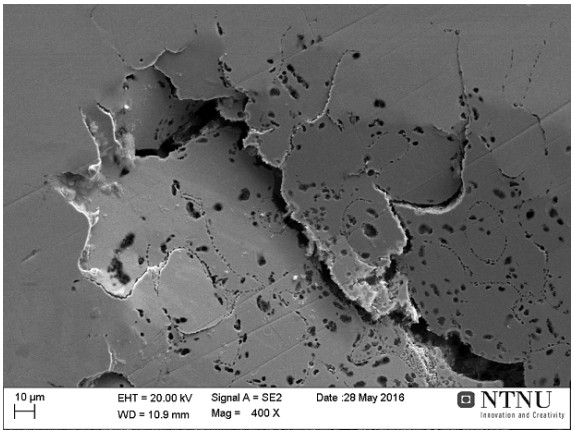

(c) Sample 2.35, magnification 400X.

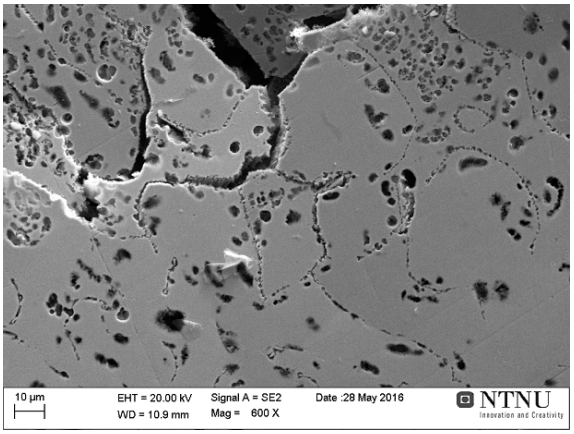

(d) Sample 2.35, magnification 600X.

Figure 4.32: Surface characterization by SEM of sample 2.35 after anodic CPP.

Chapter 5

Discussion

5.1 Effect of isothermal heat treatment on microstructure

The heat treatments in this work were based on the TTT diagram of the SDSS grade UNS S32750, given in Figure 2.5 in Section 2.2 [2]. Similar results for the SDSS grade UNS S39274, used in this work, were obtained. This may be due to a similar chemical composition between the two SDSS. The solution annealing was chosen to be 1110°C based on recommendations for obtaining a microstructure consisting of austenite and ferrite, without intermetallic precipitates and secondary phases [20]. This was successful based on surface characterization of the microstructure after solution annealing, as is shown in Figure 4.1. There was not observed any intermetallic precipitates or secondary phases in the solution annealed condition. For DSS and SDSS containing molybdenum, intermetallic precipitates and secondary phases can form up to about 1050°C, which is one of the reasons for the successful solution annealing at 1110°C [21].

The surface characterization of the microstructure in Figure 4.2 - 4.4 show formation of the χ - and σ - phase, secondary austenite and chromium nitrides. This phases and precipitations are emphasized in this thesis. The isothermal heat treatment temperatures used in this thesis were 820°C, 870°C and 940°C. It is in agreement with the literature that this phases form at the given temperatures. They have been reported to mainly form in the temperature range of 700 - 900°C [19, 26, 36, 3].

At an isothermal heat treatment temperature of 870°C, it seems like the χ - phase starts to nucleate at grain boundaries after 1,5 minutes of heat treatment, as shown in Figure 4.2b. Propagation of the χ - phase can further be observed in Figure 4.2c. By comparing the microstructure after 1,5 and 2 minutes of heat treatment at this temperature, it may indicate more nucleation areas of χ - phase formation after 2 minutes. The σ - phase starts to form after the χ - phase, which may be due to higher precipitation kinetics of the χ - phase, at lower isothermal heat treatment times, than the σ - phase. This is in accordance with the TTT

diagram of UNS S32750. In addition, tungsten has been reported to promote formation of the χ - phase, which may be a reason for nucleation of this phase after 1 minute of isothermal heat treatment at 870°C [6, 57]. Comparison of Figure 4.2c and 4.2d indicates that the σ - phase has started to form at grain boundaries between 2 and 4 minutes of heat treatment at 870°C. This is in agreement with the TTT diagram of UNS S32750, which shows that the σ - phase starts to precipitate after about 2,4 minutes of heat treatment at about 870°C. The σ - phase appears to be darker than the χ - phase, which is in accordance with Figure 2.10 in Section 2.2.1 [27]. This can be due to the higher amount of molybdenum in the χ - phase than in the σ - phase, as can be seen in Table 4.2 [32].

In Figure 4.2d, the σ - phase grows preferentially into the ferrite grains, which is the darker phase. This may be due to higher concentration of chromium and molybdenum in the ferrite matrix, which are the elements that the σ - phase mainly consists of, in addition to iron as can be seen in Table 4.2 [19, 29].

After 20 minutes of isothermal heat treatment at 820°C, as shown in Figure 4.3b - 4.3d, a significant amount of σ - phase seems to have formed. This is due to the high isothermal heat treatment time. The morphology of the σ - phase seems to be more compact with higher isothermal heat treatment temperature, as can be seen in Figure 4.2d, 4.3d and 4.4d. A coral - like structure can be observed from the isothermal heat treatment at 820°C. This may be due to the low diffusion velocity at low precipitation temperatures leading to shorter diffusion distance as described in Section 2.2.1 [27]. A more compact σ - phase morphology can be observed for the isothermal heat treatment temperatures 870 and 940°C, which may be due to a lower nucleation formation force but high diffusion rate. This observation is in agreement with reported morphology of the σ - phase in Figure 2.9 in Section 2.2.1 [27].

5.2 Effect of isothermal heat treatment on localized corrosion properties

5.2.1 Critical pitting temperature measurements

CPT measurements were done by a modified ASTM G48 method as described in Section 3.3.2 [52, 53]. In the beginning of each measurement, OCP of several of the samples showed a stable value of 700 mV_{SCE}, which is in accordance with reported values of OCP of stainless steels in this electrolyte [53]. The OCP values showed some drops around the 700 mV_{SCE} value, which may be due to the amount of measurements. It may also be due to chemical reactions at the metal surface. When the temperature reached a certain value, the OCP dropped, as can be seen in Figure 4.5. The temperature when OCP dropped below 500 mV_{SCE}, was defined as the CPT. This can be explained based on polarization curves. Increased temperature or detrimental phases can decrease the pitting corrosion area or increase the active area in the polarization curve. The corrosion rate depends on the intersection between the cathodic tafel slope for dissolution of trivalent iron into divalent iron with the anodic polarization

curve. If the sample contains a stable oxide film, the intersection gives a low corrosion rate. If the temperature is raised or detrimental phases are present and the oxide film contains damages, the intersection can be found in the pitting area or in the active area of the anodic polarization curve, giving a high corrosion rate. This will also suppress the OCP from the corrosion potential of iron to lower values, and the critical value for activation and corrosion has been found to be about 500 mV_{SCE} [53], as illustrated in Figure 2.24 in Section 2.6.2. The surface characterization of the samples after CPT measurements show severe corrosion, indicating that the OCP criteria correlates with initiation of localized corrosion, as can be seen in Figure 4.21.

The average CPT of solution annealed samples was found to be 77,5°C, based on the values in Table 4.3. CPT has been reported to be higher than this in some previous work, at about 85°C [6]. The lower CPT, obtained in this work, may be due to microstructural factors as for instance grain size and grain orientation, which can affect the corrosion properties. Another reason for this may be the surface condition. The test samples in this work had a 1μm surface finish, contrary to the reported test samples, which had a 600 grit surface finish [6]. It may also be due to initiation of other localized corrosion forms. Surface characterization of for instance sample 1.12, as can be seen in Figure 4.21a, shows corrosion from where the platina thread was mounted, which may have caused conditions for crevice corrosion.

At the isothermal heat treatment temperature 870°C, the average CPT was reduced by 12,5°C (77,5 °C - 65°C) after 2 minutes of heat treatment, from solution annealed condition. From 2 to 4 minutes of isothermal heat treatment at the same temperature, the average CPT was reduced by 20°C (65°C - 45°C), given in Table 4.3 and Figure 4.6. Figure 4.2 indicates that the χ - phase may be the phase causing the reduction in CPT after 2 minutes of heat treatment at 870°C. From the TTT diagram of UNS S32750 in Figure 2.5, the χ - phase starts to precipitate after 1 minute of isothermal heat treatment. This is in accordance with the result in Figure 4.2b. The reason for the reduced CPT with increased χ - phase precipitation after 2 minutes of isothermal heat treatment at 870°C, may be that the χ - phase consumes chromium and molybdenum, leading to formation of γ_2 from ferrite, as described in Section 2.2.1 [32]. This was verified by the high amount of chromium and molybdenum in the χ - phase, given in Table 4.2. This leads to depletion of elements, such as chromium and molybdenum, causing microgalvanic cells in the microstructure. These alloying elements increase the pitting corrosion resistance of SDSS in solid solution, as given by the $PREN_W$ in Equation 2.25. The γ_2 absorbs nickel and rejects chromium and molybdenum. As a consequence, γ_2 has lower concentration of chromium, molybdenum and nitrogen than primary γ [18]. The reduced amount of chromium and molybdenum in γ_2 explains why pitting can initiate in that area. The metallic contact between the more noble χ - phase and the less noble γ_2 may give the same effect as when two dissimilar metals are in metallic contact [27]. This can give a galvanic corrosion effect that enhances the dissolution of γ_2, as described in Section 2.4. The anode to cathode area is an important factor for the corrosion rate, given by Equation 2.14 [39]. The noble α -, γ -, χ - and σ - phase have a larger area than the γ_2, which may enhance the corrosion rate in accordance with Equation 2.4.

Figure 4.2d shows that σ - phase precipitation has initiated between 2 and 4 minutes of heat treatment. The σ - phase precipitation leads to depletion of chromium and molybdenum from surrounding ferrite and formation of γ_2, as described in Section 2.2.1 [19]. This leads to a reduction in pitting corrosion resistance in the depleted zones due to the same reason as described for the χ - phase above, which may be the reason for the reduced CPT after heat treatment of 4 minutes at 870°C [3]. This is in agreement with the literature, and it has been reported that the σ - phase reduces localized corrosion properties of SDSS [3, 19, 16]. After isothermal heat treatment at 870°C for 10 minutes, the microstructure was found to contain 2,7 vol% of the σ - phase. Due to this, the significant reduction in CPT after isothermal heat treatment at 870°C for 4 minutes, indicates that low amounts of the σ - phase reduces the pitting corrosion resistance of UNS S39274. This is in accordance with the literature, and it has been reported that only 1% of σ - phase reduces the corrosion resistance of SDSS [16].

At the isothermal heat treatment temperature 820°C, the average CPT was reduced by 12,5°C (77,5°C - 65°C) after 1 and 2 minutes of heat treatment, from solution annealed condition. This is given in Table 4.3 and Figure 4.7. Figure 4.3 shows no significant precipitation of χ - phase after 4 minutes of heat treatment at this temperature. This may be due to the etching method used for this sample before surface characterization. Precipitation at grain boundaries, which is shown in Figure 4.3a, may be chromium nitrides. The reduction in CPT after low isothermal heat treatment times at 820°C may be due to the precipitation of intergranular chromium nitrides. The UNS S39274 contains 0,29 wt% nitrogen, as given in Table 3.1, which may cause supersaturation of nitrogen in ferrite, which can lead to formation of chromium nitrides [2, 34]. The reduction in CPT is in accordance with the literature, where it has been reported that isothermal heat treatment, in the temperature range of 700 - 900°C, may result in intergranular chromium nitrides, which has an influence on pitting corrosion of SDSS by reducing CPT [2, 36].

After 4 minutes of heat treatment at 820°C, the average CPT was reduced by 22,5°C (77,5°C - 55°C) from solution annealed condition. CPT after 4 minutes of isothermal heat treatment at 870°C was found to be lower than CPT after 4 minutes of isothermal heat treatment at 820°C. This may be due to less precipitation of the σ - phase at 820°C than after 4 minutes of heat treatment at 870°C. It is in accordance with the TTT diagram of UNS S32759 that the kinetics of the σ - phase is higher at 870°C, than at 820°C. This may be the reason for the lower CPT after 4 minutes of heat treatment at 870°C. After 20 minutes of heat treatment at 820°C, the CPT was lower than 40°C. This was concluded since the OCP value of sample 1.17 and 1.18 dropped below 500 mV_{SCE} rapidly after the test was started. A reason for this trend can be the high amount of σ - phase precipitated, as can be seen in Figure 4.3b - 4.3d.

At the isothermal heat treatment temperature 940°C, the average CPT was reduced by 7,5°C (77,5°C - 70°C) after 1 and 2 minutes of heat treatment, from solution annealed condition. This is given in Table 4.3 and Figure 4.8. The reason for the higher resistance against localized corrosion at this heat treatment temperature than at 820°C and 870°C may be due to lower precipitation kinetics of detrimental phases at low isothermal heat treatment times. Figure 4.4a - 4.4b indicates no significant precipitation of the χ - phase, but rather some small

amounts of precipitation of the σ - phase. The χ - phase has been reported to mainly precipitate in the temperature range of 750 - 850°C, and the chromium nitrides in the temperature range of 700 - 900°C [2, 3]. This may be the reason for the high localized corrosion resistance at low isothermal heat treatment times at 940°C. Figure 4.4c - 4.4d indicate that the σ - phase has propagated and the amount of this phase has increased from 2 to 4 minutes of heat treatment. This may be the reason for the reduction in CPT by 15°C (77,5°C - 62,5°C) after 4 minutes of heat treatment at 940°C, from solution annealed condition.

The objective with the CPT measurements was to determine a critical IHt at a given isothermal heat treatment temperature, where a reduction in localized corrosion resistance of UNS S39274 was observed. CPT as a function of IHt for the three isothermal heat treatment temperatures, 870°C, 820°C and 940°C from Figure 4.6, 4.7 and 4.8, can be seen in Figure 5.1. The reduction in the average CPT from solution annealed condition to 4 minutes of isothermal heat treatment time is 32,5°C, 22,5°C and 15°C at the isothermal heat treatment temperatures 870°C, 820°C and 940°, respectively. Figure 5.1 indicates that a isothermal heat treatment time between 2 and 4 minutes may be a critical IHt at the three isothermal heat treatment temperatures, due to a significant loss in localized corrosion properties from solution annealed condition. When the isothermal heat treatment time increases from 4 to 20 minutes at 820°C and 940°C, another significant loss in localized corrosion properties was observed. The CPT was determined to be less than 40°C at 820°C and 940°C, which was the lowest electrolyte temperature, but was included in Figure 4.7, 4.8 and 5.1 for comparison. This indicates a significant loss in localized corrosion resistance, due to the high amount of detrimental phases, as can be seen in for instance Figure 4.3b - 4.3d.

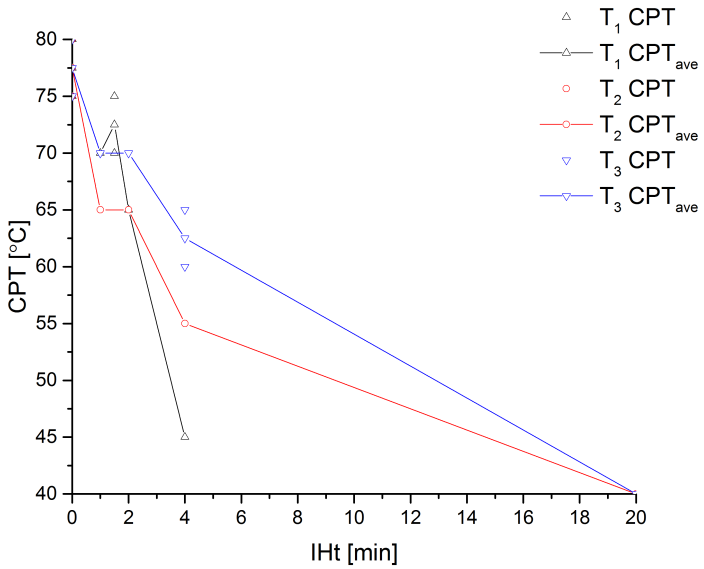

Figure 5.1: CPT as a function of IHt for samples heat treated at the isothermal heat treatment temperatures T_1 (870°C), T_2 (820°C) and T_3 (940°C) according to the test matrix in Table 3.4. CPT of solution annealed samples are included to compare.

The objective with the corrosion maps, shown in Figure 4.9, 4.10 and 4.11, was to determine the IHT with the highest reduction in pitting corrosion resistance for a given isothermal heat treatment time. CPT as a function of IHT for the three isothermal heat treatment times 1, 2 and 4 minutes, from Figure 4.9, 4.10 and 4.11, are shown in Figure 5.2 for comparison.

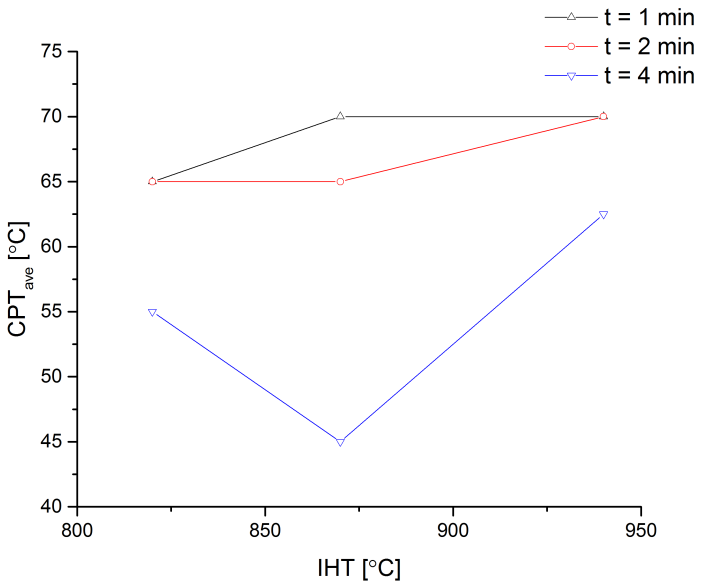

Figure 5.2: CPT as a function of IHT for samples heat treated for 1, 2 and 4 minutes, according to test matrix 3.4.

Figure 5.2 indicates that the reduction in CPT and localized corrosion properties from 1 minute of isothermal heat treatment to 4 minutes of isothermal heat treatment is highest at 870°C. This may be due to higher precipitation kinetics of intermetallic precipitates and secondary phases at this temperature. It has been reported that the highest precipitation rate of the σ - phase in a DSS 2205 is at about 850°C, as shown in Figure 2.7 [19]. The obtained results are also in accordance with reported CPT of UNS S31803 aged at several temperatures for 10 minutes, where an aging temperature of about 850°C gave the lowest CPT, as shown in Figure 2.25 [15]. Figure 5.2 also shows that the reduction in CPT was lowest at 940°C. This can be due to several possible intermetallic precipitates and secondary phases and a higher precipitation kinetics at 870°C and 820°C, compared to at 940°C. This is also the case for UNS S32750, which can be seen from the TTT diagram in Figure 2.5.

5.2.2 Anodic cyclic potentiodynamic polarization curves

The anodic CPP curves obtained in this work included three electrochemical responses, as described in Section 2.6.2, illustrated by Figure 2.21 - 2.23 [48]. The anodic CPP curve in Figure 4.14 is an example with no hysteresis, indicating anodic dissolution, oxygen evolution and no pitting corrosion. This is supported by the surface characterization of sample 2.13 and 2.14 in Figure F.19e and F.19f in Appendix F. The anodic CPP curve in Figure 4.16 is an example with a little hysteresis, indicating small pits, which is supported by the surface

characterization of sample 2.33 and 2.34 in Figure F.20i and F.21a in Appendix F. The anodic CPP curve in Figure 4.13 is an example with a hysteresis, indicating pitting corrosion. This is supported by the surface characterization of sample 2.11 and 2.12 in Figure F.19d in Appendix F and 4.26b in Section 4.4.2. For several samples with an anodic CPP curve without hysteresis, the value of E_p was about 1,0 V_{SCE} as given in Table 4.4 - 4.7 for the samples tested at an electrolyte temperature of 40°C and 60°C. This is in accordance with several reported values of 1,0 V_{SCE} of E*p* for DSS and SDSS in the literature [6, 48, 45, 26].

OCP was measured prior to anodic CPP. The average OCP of solution annealed condition UNS S39274 was measured to be -26,3 mV_{SCE}, 1,0 mV_{SCE} and -12,8 mV_{SCE} at 40°C, 60°C and 80 °C, respectively. This indicates a quite similar value at the three test temperatures. The electrolyte was bubbled with N_2(g) to secure minimum dissolved O_2(g), but a high value of OCP may indicate dissolved O_2(g). Dissolved oxygen may lead to formation of hydroxide ions by Equation 2.12 in Section 2.3, which can cause formation of oxides on the metal surface. However, OCP is affected by several factors, such as geometry and temperature [43]. Increased temperature increases the possibility of a lower OCP value, due to degradation of the oxide film. The solution annealed samples 2.1 - 2.6 had similar values of OCP, which may be due to an oxide film at open circuit condition at the three electrolyte test temperature. For isothermal heat treated samples, the general trend was a reduction in OCP with increasing electrolyte temperature from 40°C to 80°C. Sample 2.7 - 2.12, heat treated at 870°C for 1 minute, had a reduction in the average OCP of 168,6 mV when the electrolyte temperature was increased from 40°C to 80°C. Samples heat treated at 870°C for 1,5 minutes and 2 minutes had a reduction in average OCP of 177,6 mV and 82,4 mV when the electrolyte temperature was increased from 40°C to 80°C, respectively, based on the values in Table 4.6 - 4.7. Samples heat treated at 820°C for 4 minutes had a reduction in average OCP of 224,88 mV when the electrolyte temperature was increased from 40°C to 80°C, based on the values in Table 4.8. The observed decrease in OCP may be due to an increased amount of precipitated detrimental phases, which can damage the oxide film on the metal surface [39]. Generally, the measured OCP values in this work are in accordance with reported values of 0 V_{SCE} - -0,2 V_{SCE} at 70°C in the literature, which can be seen in Figure 2.15 [43].

E_p was found to decrease with increasing electrolyte temperature. For solution annealed samples, E_p decreased 800 mV from a electrolyte test temperature of 40 to 80°C as given in Table 4.4. For samples heat treated at 870°C for 1 minute, E_p decreased with 751,2 mV for the same temperature interval. For samples heat treated at 870°C for 1,5 minutes and 2 minutes, E_p decreased 833,8 mV and 899,8 mV, respectively. This trend shows a significant drop in E_p with increased electrolyte temperature. A reason for this may be that a higher temperature makes the oxide film less stable, increasing the possibility for damages in the oxide film, which can lead to initiation of pitting corrosion as described in Section 2.6.1. E_p has been reported to decrease with increasing temperature, as shown in Figure 2.17 [39, 56]. Another reason for the reduction in E_p with increasing temperature, can be higher chemical reaction rates due to higher convection or increased rate of ion transport in the electrolyte [39].

At an electrolyte temperature of 40°C, E_p was found to decrease with 160,6 mV and 72,8 mV from solution annealed condition to isothermal heat treated condition at 820°C and 940° for 4 minutes, respectively. This can be seen in Figure 4.18. The same was observed at an electrolyte test temperature of 60°C, where E_p was found to decrease with 408,7 mV and 215,0 mV from solution annealed condition to isothermal heat treated condition at 820°C and 940°C for 4 minutes, respectively. This may be due to the formation of χ - phase, σ - phase, γ_2 and chromium nitrides, as shown in Figure 4.3a and 4.4c - 4.4d. The formation of this phases reduce the pitting corrosion resistance, which is earlier described in detail in Section 5.2.1. A significant reduction in E_p with increasing amount of intermetallic precipitates and secondary phases is in accordance with reported literature [2, 6, 3, 12].

The reduction in E_p was more significant at the isothermal heat treatment temperature 820°C, than after isothermal heat treatment at 940°C, for the same isothermal heat treatment time. This may be due to the morphology of the precipitated σ - phase. At 820°C, the σ - phase was observed to be coral - like, as can be seen in Figure 4.3d, contrary to the more compact σ - phase at 940°C, as shown in Figure 4.4d. This observation is in accordance with earlier work, as can be seen in Figure 2.9 in Section 2.2.1 [27]. The diffusion velocity is lower at 820°C than at 940°C, which leads to shorter diffusion distance and higher density of precipitations [27]. This may lead to increased depletion from the ferrite and austenite in the microstructure, resulting in lower localized corrosion resistance for samples heat treated at 820°C. Another reason is a steeper concentration gradient at lower heat treatment temperatures, due to reduced diffusion rate [55], leading to a higher electrochemical potential between the σ - phase and the nearby γ_2. As a result, the galvanic effect and the galvanic corrosion rate can increase as described in Section 2.4 [39].

At an electrolyte temperature of 80°C, E_p was found to decrease with 87,7 mV from solution annealed condition to isothermal heat treated condition at 870°C for 2 minutes, as shown in Figure 4.20. This was contrary to samples tested at an electrolyte temperature of 40°C and 60°C for the same heat treatment conditions, as can be seen in Figure 4.18 and 4.19. E_p decreases with increasing electrolyte temperature, which is shown in Figure 2.17, and on the increasing degradation of the oxide film with increasing temperature [39]. At an electrolyte temperature of °C, E_p was found to decrease with 165,2 mV and 188,1 mV for samples in solution annealed condition to samples heat treated at 820°C and 940°C for 4 minutes, respectively. This may be due to the increased amount of intermetallic precipitates and secondary phases as described for the trends of E_p as a function of IHt for the two other electrolyte temperatures 40°C and 60°C.

From anodic CPP curves obtained at an electrolyte test temperature of 40°C, the values of E_{RP} were observed to be quite stable at the heat treatment conditions. This can be seen from Table 4.4 - 4.9 in Section 4.3. This indicates that the pitting corrosion terminates at a high rate at this electrolyte test temperature. At an electrolyte temperature of 60°C and 80° a drop in E_{RP} was observed from solution annealed condition to isothermal heat treatment condition, as can be seen from Table 4.4 - 4.9. This may indicate that the formation of detrimental phases has more effect on the termination of pitting corrosion at higher electrolyte test temperatures.

This may be due to decreased rate of formation of the oxide film on the metal surface and in the pits after pitting corrosion at increasing electrolyte temperature.

Several of the anodic CPP curves contained more than one area of formation of oxides, which can be seen in Figure E.10 in Appendix E and 4.16 in Section 4.3. This gives two values of i_p, given in Table 4.6 and 4.8. The formation of several oxides that form at various potential intervals can be predicted by Pourbaix diagrams. The Pourbaix diagram of iron in Figure 2.14 in Section 2.3, indicates that Fe_3O_4 forms in the potential range of -0,6 V_{SHE} - -0,2 V_{SHE} [41]. SDSS contain several alloying elements that contribute to the formation of an oxide film, which lead to a complex oxide film. From surface characterization by 3D OM after anodic CPP, several colors were observed on the samples surfaces, as can be seen in Figure 4.26 in Section 4.3 and in Figure F.18 - F.21 in Appendix F.

At an electrolyte temperature of 60°C the obtained anodic CPP curves of sample 2.9 and 2.15 had no value of i_p, as can be seen in Figure 4.12 and Figure E.5 in Appendix E, respectively. This was not observed for the corresponding parallels, sample 2.10 and 2.16, in the same heat treatment condition. Sample 2.10 and sample 2.16 were tested after sample 2.9 and 2.15, respectively. This resulted in a longer time in the desiccator prior to anodic CPP, for sample 2.10 and 2.16, leading to a stable oxide layer on the metal surface. Anodic CPP curves obtained at the electrolyte temperatures 40°C and 80°C, had a value for this parameter, as can be seen in Table 4.4 - 4.9. An electrolyte temperature of 60°C is close to the CPT, wich can cause damage in the oxide layer.

5.3 Comparison of CPT measurements and anodic cyclic potentiodynamic polarization curves

From the CPT measurements in Table 4.3, it can be seen that sample 1.1 - 1.8 are resistant against pitting corrosion above 60°C, but not above 80°C. This results are in accordance with the results from anodic CPP of samples in the same heat treatment condition. Samples heat treated at 870°C had anodic CPP curves with no hysteresis indicating no pitting corrosion at an electrolyte temperature of 40°C and 60°C. However, at an electrolyte temperature of 80°C, this samples had anodic CPP curves with a hysteresis indicating pitting corrosion. This can be seen from the anodic CPP curves of sample 2.1 - 2.24 in Figure 4.12 - 4.14 in Section 4.3 and Figure E.1 - E.9 in Appendix E.

The CPT measurements in Table 4.3, indicates that sample 1.15 and 1.16 are resistance against pitting corrosion above 40°C, but not above 60°C and 80°C. This results are in accordance with the anodic CPP curves of sample 2.25 - 2.26 in the same heat treatment condition, with no hysteresis indicating no pitting corrosion at 40°C. At 60°C the result from the anodic CPP curve of sample 2.27 is in accordance with CPT measurements, with a little hysteresis indicating small pits. However, sample 2.28 seems to be more resistant against pitting corrosion, having no hysteresis in the anodic CPP curve. This may be due to longer residence time of sample 2.28 in a desiccator, than for sample 2.27, giving a more stable oxide film. At 80°C

the result from anodic CPP curves of sample 2.29 and 2.30 are in accordance with the CPT measurements, with a positive hysteresis indicating pitting corrosion.

The CPT measurements in Table 4.3 show that sample 1.23 and 1.24 are resistant against localized corrosion up to about 60°C, but not above 80°C. This results are in accordance with the results from anodic CPP curves of sample 2.31 and 2.32, with the same heat treatment condition, with no hysteresis indicating no pitting corrosion at 40°C. At 60°C the results from the anodic CPP curves of sample 2.33 and 2.34 are in accordance with CPT measurements of samples in the same heat treatment condition, with little hysteresis and low E_{RP} indicating that the test temperature is near the CPT, given in Table 4.3 and 4.9. This can be seen from the anodic CPP curves of sample 2.31 - 2.34 in Figure 4.15 - 4.17 in Section 4.3. At 80°C the results from the anodic CPP curves of sample 2.35 and 2.36 are in accordance with CPT measurements of samples in the same heat treatment condition, with a hysteresis indicating pitting corrosion. This can be seen from the anodic CPP curves of sample 2.35 - 2.36 in Figure 4.17 in Section 4.3.

Figure 5.3 - 5.5 show CPT and E_p as a function of IHt for samples heat treated at 870°C, 820°C and 940°C. The E_p values in Figure 5.3 - 5.5 are obtained from anodic CPP curves recorded at an electrolyte test temperature of 60°C, as an example. Figure 5.3 - 5.5 show that the CPT measurements are in accordance with the E_p values from anodic CPP curves. Results from the CPT measurements and values of E_p indicate that a isothermal heat treatment time between 2 and 4 minutes may be a critical IHt at the three isothermal heat treatment temperatures used in this work, due to loss in pitting corrosion properties.

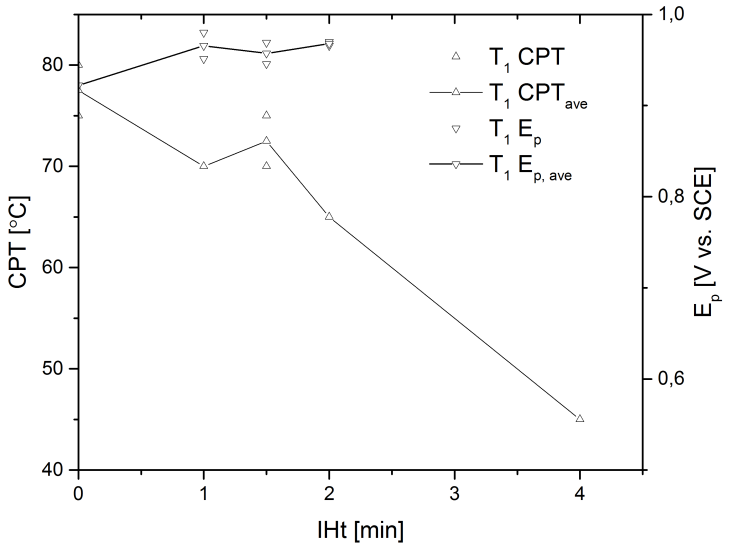

Figure 5.3: CPT and E_p as a function of IHt for samples heat treated at temperature T_1 (870°C) according to Table 3.4 and Table 3.6. CPT and E_p of solution annealed samples are included for comparison (IHt = 0). E_p values were obtained from anodic CPP curves recorded at an electrolyte temperature of 60°C. This figure is a combination of Figure 4.6 and the black line in Figure 4.19.

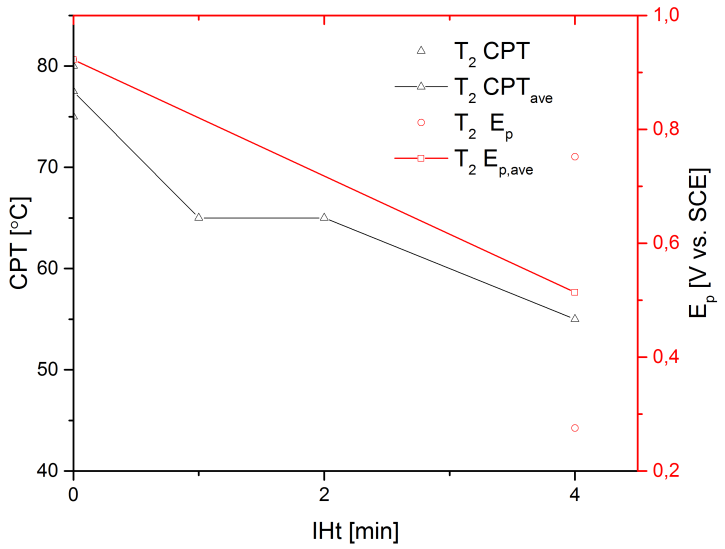

Figure 5.4: CPT and E_p as a function of IHt for samples heat treated at temperature T_2 (820°C) according to Table 3.4 and Table 3.6. CPT and E_p of solution annealed samples are included for comparison (IHt = 0). E_p values were obtained from anodic CPP curves recorded at an electrolyte temperature of 60°C. This Figure is a combination of Figure 4.7 and the red line in Figure 4.19.

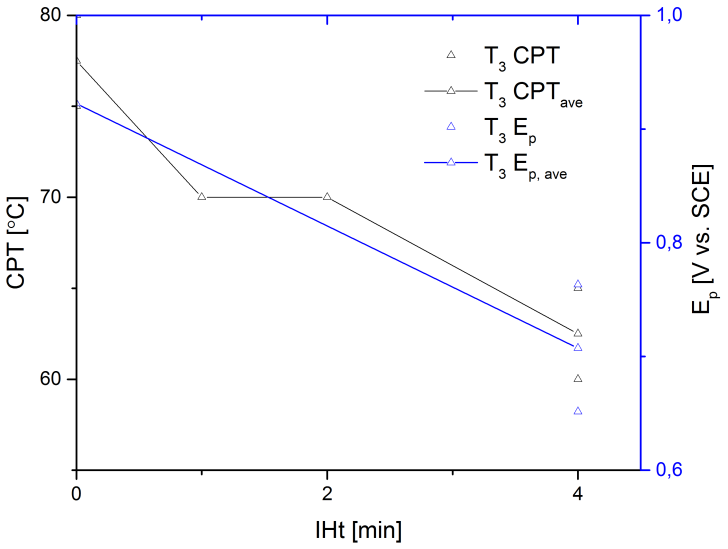

Figure 5.5: CPT and E_p as a function of IHt for samples heat treated at temperature T_3 (940°C) according to Table 3.4 and Table 3.6. CPT and E_p of solution annealed samples are included for comparison (IHt = 0). E_p values were obtained from anodic CPP curves recorded at an electrolyte test temperature of 60°C. This Figure is a combination of Figure 4.8 and the blue line in Figure 4.19.

E_p was observed to be quite stable for samples heat treated for 2 minutes at 870°C with an electrolyte temperature of 40°C and 60°C. When the electrolyte temperature was increased to 80°C, a reduction in E_p was observed, as shown in Figure 4.20. The high electrolyte temperature may lead to a less stable oxide film causing damages and exposure to the chloride ions in the test solution. The general loss in localized corrosion resistance between IHt from 2 to 4 minutes may be due to an increasing amount of intermetallic precipitates and secondary phases forming with increasing isothermal heat treatment time. Such phases can be the σ - phase, the χ - phase, chromium nitrides and γ_2, as described before.

5.4 Surface characterization

The general trend of the samples after CPT measurements was an increasing amount of pitting corrosion initiation sites with increasing isothermal heat treatment times. This is illustrated by surface characterization of sample 1.12 - 1.17 in Figure 4.21, heat treated at 820°C for 1, 2, 4 and 20 minutes according to the test matrix in Table 3.4. The degree of pitting corrosion seems to increase with increasing isothermal heat treatment time, which is in accordance with the measured CPT values. This can be due to the higher amount of intermetallic precipitates and secondary phases, leading to increased amount of initiation sites for pitting corrosion.

Pitting corrosion was found to initiate at grain boundaries, and at a higher degree with increasing isothermal heat treatment time. For solution annealed samples and samples isothermal heat treated for short times, pitting corrosion was observed to initiate preferentially inside grains, as can be seen in Figure 4.22b. The pitting corrosion was found to initiate and propagate along grain boundaries at a higher degree with increasing isothermal heat treatment times. This can be seen in Figure 4.22a - 4.22f. This may be due to higher amounts of detrimental phases with increasing heat treatment times, which lead to higher degree of depletion. The σ - and χ - phases contain a high amount of chromium and molybdenum, leading to depletion of this elements from surrounding ferrite and austenite, which is given in Table 4.2. This results in a reduction in pitting corrosion resistance in the depleted zones, near the precipitates [3]. Since the formation of the detrimental phases initiates and propagates at grain boundaries, the depletion is high at the grain boundaries. The depletion was verified by the relative amount of alloying elements in the ferrite, austenite, χ - and σ - phase, given in Table 4.1 and 4.2, which shows higher amount of chromium and molybdenum in the precipitates phases than in ferrite and austenite. This can explain the increased degree of pitting corrosion at grain boundaries with increased isothermal heat treatment times [3, 26]. Figure 4.32a - 4.32d by SEM also support this observation, showing pitting corrosion, revealing the grains in the microstructure.

Initiation and propagation of pitting corrosion along grain boundaries were also observed with increasing isothermal heat treatment times, of samples after anodic CPP. Surface characterization of a solution annealed sample, shown in Figure 4.27, indicates that pits initiate preferentially inside grains. Surface characterization of sample 2.29 and 2.35, shown in Figure 4.28 - 4.31 indicates that pitting corrosion initiates and propagates preferentially along grain bound-

aries. This may be due to an increased amount of intermetallic precipitates and secondary phases, causing depletion along grain boundaries, verified by the relative amount of alloying elements in Table 4.1 and 4.2 [3, 26]. The surface characterization indicates accordance between pitting corrosion initiation and propagation of samples after CPT measurements and samples after anodic CPP, as illustrated for sample 1.16 and 2.29, heat treated at 820°C for 4 minutes, in Figure 4.22e and 4.28.

Generally, a higher amount of pits was observed with increasing isothermal heat treatment time, as shown in Figure 4.26. Only samples tested at an electrolyte temperature of 80°C was included, due to the observation of pits after ended tests at this electrolyte temperature. The surface of sample 2.5, shown in Figure 4.26a, contained few, but large pits, contrary to for instance sample 2.29 and 2.35 in Figure 4.26e and 4.26f, which contained several small pits. This was also verified by pit depth and width measurements, given in Table 4.10. This may be due to an increased amount of intermetallic precipitates and secondary phases for higher isothermal heat treatment time. High amount of such phases leads to a higher density of depleted zones, resulting in increased amount of initiation sites for pitting corrosion. As a consequence of this, few pits initiate at the solution annealed condition, contrary to initiation of several pits at isothermal heat treatment condition. This can also affect the size of the pits. The anodic CPP curves of samples with a higher amount of pits reached the anodic current density limit of 5 mA/cm^2 at a lower potential, which is illustrated in Figure 5.6. This was observed to be an indication of amount of pits and pit depth and width, since sample 2.29 contained higher amount of pits and lower pit depth and width than sample 2.5.

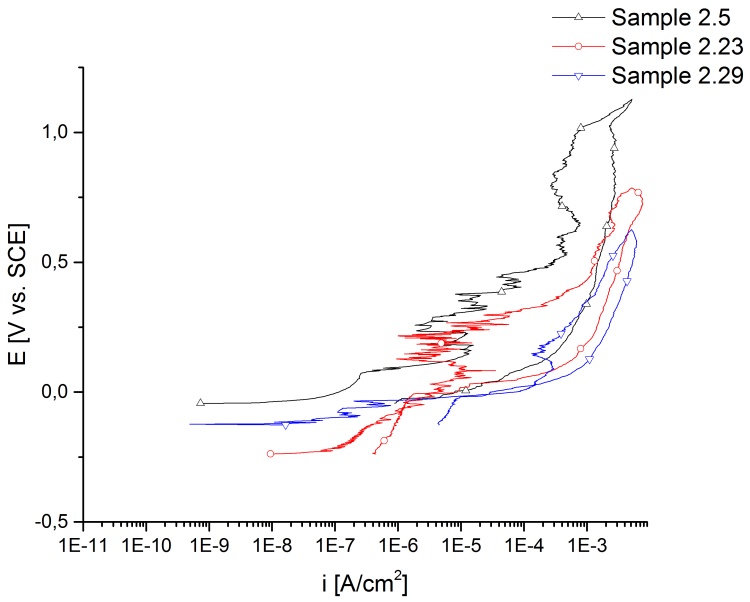

Figure 5.6: Anodic CPP curves of sample 2.5, 2.23 and 2.29, according to test matrix 3.6. The curves were recorded with an electrolyte temperature of 80°C.

For samples with anodic CPP curves containing no hysteresis, anodic dissolution was observed, as shown in Figure 4.25a - 4.25d. A possible reason for this phenomena is that the samples were forced to undergo anodic dissolution, instead of pitting corrosion, as described in Section

2.3 [39, 40]. Selective anodic dissolution of ferrite can be observed as the dark areas in Figure 4.25a - 4.25d, which is in accordance with the literature [49]. Comparison of Figure 4.25b and 4.25d, indicates that the bright austenite phase has been anodic dissolved at higher degree on sample 2.27 than on sample 2.10. A reason for this may be higher depletion of alloying elements from the austenite phase in sample 2.27, due to increased isothermal heat treatment time.

Several of the samples showed corrosion on the edges, as is shown for sample 1.4 and 1.9 in Figure 4.24. Selective corrosion on edges and not at the sample surface can be due to damages in the oxide film at edges or due to strain.

For anodic CPP curves without hysteresis, indicating anodic dissolution, a red brown corrosion product was observed in the beaker after ended test, as shown in Figure 3.8a. For anodic CPP curves with hysteresis, indicating pitting corrosion, a black green corrosion product was observed, as can be seen in Figure 3.8b. The corrosion products can be explained by the Pourbaix diagram of iron in Figure 2.14. The anodic CPP curves, indicating dissolution, shows an increase in anodic current density at around $1{,}0_{SCE}$ V. The Pourbaix diagram of iron indicates that trivalent iron is the stable compound in this potential area. Trivalent iron can form $FeOH_3$, which has a red brown color [40]. Contrary, anodic CPP curves indicating pitting corrosion, shows an increase in anodic current density at lower potentials. The Pourbaix diagram of iron indicates that divalent iron is the stable compound at this potential area. Divalent iron can form $FeOH_2$, which has a black green color [40].

5.5 Limitations and sources of error

Before heat treatments, the heat rate of UNS S39274 was found by logging the temperature in the middle of one test sample. The placement of the samples was neglected, but might have an effect on the heat rate of the test samples. In addition, another oven was used for the isothermal heat treatments at 870°C than for the other isothermal heat treatments due to maintenance of the oven. However, the temperature settings of both ovens were set to the heat treatment temperatures and times as given in Table 3.2.

The CPT measurements were based on the 500 mV_{SCE} limit, indicating initiation of pitting corrosion. The residence time below this limit, as can be seen for the OCP and temperature measurements, varied to some degree for the samples. This could give a higher degree of corrosion on samples with higher residence time than samples with lower residence time. In addition, it was not necessarily pitting corrosion that initiated on the sample surface during CPT measurements. The surface characterization of some of the samples indicated corrosion initiation in regions where the platina thread was mounted, which may cause conditions for crevice corrosion or other corrosion mechanisms. However, the results from the CPT measurements indicated a critical IHt at the three isothermal heat treatment temperatures used in this work, due to loss in localized corrosion properties. The temperature was increased by 5°C and not by 1°C during the CPT measurements, which gives rounded values of CPT

and may give a source of error by maximum 4°C.

Prior to electrochemical measurements, the samples were stored in a desiccator for various times. For two parallels with the same preparation prior to electrochemical measurements, the sample which was tested first was stored for a lower time in the desiccator compared to the sample that was tested last. This could give a spread in the results between the two parallels. The temperature in the electrolyte was regulated by a temperature regulator in the solution, which had an uncertainty of 2°C, which could contribute to some small errors in the measurements.

In Figure 4.18 - 4.20, E_p was assumed to be linear for samples that were solution annealed to samples that were isothermal heat treated at 820°C and 940°C for 4 minutes, for comparison.

5.6 Suggestions for further work

One suggestion for further work can be to test samples at several isothermal heat treatment temperatures and times. A loss in localized corrosion resistance of UNS S39274 was found to be between 2 and 4 minutes of heat treatment at the three isothermal heat treatment temperatures used in this work. However, by expanding the number of isothermal heat treatment temperatures and times, a more exact value of the critical time can be determined.

Another suggestion for further work is to determine the volume fraction of the phases after heat treatment of the samples. This can give information about at which volume fraction of a certain phase, the UNS S39274 is exposed to a reduction in localized corrosion resistance. This could be done with for instance EBSD. In addition, the effect of grain size could be investigated.

The effect of tungsten on the localized corrosion resistance of SDSS, could be investigated at the same isothermal heat treatment temperature and time. Tungsten is included in the $PREN_W$ value, and can give increased resistance against pitting corrosion. In addition, the ASTM G61 anodic CPP could be done at several temperatures to investigate the effect of electrolyte test temperature in more detail.

The OCP of various intermetallic precipitates and secondary phases could be measured to investigate how the localized corrosion resistance of SDSS. In situ characterization of localized corrosion during electrochemical measurements could also be performed to investigate initiation and propagation in the microstructure.

Chapter 6

Conclusions

In this work, the effect of isothermal heat treatment in pitting corrosion of UNS S39274 was investigated. The effect of the σ - phase, χ - phase, γ_2 and chromium nitrides was emphasized. Results from the experimental work revealed the following:

- The solution annealed samples at 1110°C for 15 minutes contained no intermetallic precipitates and secondary phases.

- Nucleation of the χ - phase was observed after isothermal heat treatment at 870°C for 1,5 minutes, while the σ - phase was observed to nucleate after isothermal heat treatment at 870°C for 4 minutes.

- After 20 minutes of isothermal heat treatment at 820°C and 940°C, a significant amount of the σ - phase was observed. The morphology of the σ - phase was coral - like at the isothermal heat treatment temperature 820°C.

- Formation of the σ - phase was observed after isothermal heat treatment at 940°C for 4 minutes. The morphology of the σ - phase was compact at at the isothermal heat treatment temperature.

- The average CPT was measured based on a modified ASTM G48 method, and determined to be 77,5°C for solution annealed samples.

- The average CPT of samples isothermal heat treated at 870°C, 820°C and 940°C for 4 minutes, was reduced by 32,5°C, 22,5°C and 15°C, respectively.

- The average CPT was found to generally decrease with increasing isothermal heat treatment time for a given isothermal heat treatment temperature.

- The anodic CPP curves obtained by ASTM G61 tests included three electrochemical responses, curves with no hysteresis indicating anodic dissolution and no pitting corrosion, curves with a little hysteresis indicating small pits and curves with hysteresis indicating pitting corrosion.

- The obtained anodic CPP curves of samples recorded at an electrolyte temperature of

80°C contained hysteresis, and the amount of pits were observed to increase with increasing isothermal heat treatment time.

- OCP decreased generally with increased electrolyte temperature and increased isothermal heat treatment time at a given isothermal heat treatment temperature.

- E_p decreased generally with increased electrolyte temperature.

- E_p decreased generally with increased isothermal heat treatment time for a given isothermal heat treatment temperature.

- The critical isothermal heat treatment time was found to be between 2 and 4 minutes from the ASTM G48 CPT measurements and ASTM G61 anodic CPP curves.

- Selective anodic dissolution of ferrite was observed after anodic CPP indicating anodic dissolution and no pitting.

- Pitting corrosion was observed to initiate and propagate preferentially inside grains after anodic CPP of solution annealed samples.

- Pitting corrosion was observed to initiate and propagate preferentially along grain boundaries after anodic CPP of isothermal heat treated samples.

Bibliography

[1] H. K. D. H. Bhadeshia. *Steels*. Third edition, 2006.

[2] J.-O. Nilsson. Super duplex stainless steels. *Materials Science and Technology*, 8(8):685–700, 1992.

[3] Prabhu Paulraj and Rajnish Garg. Effect of Intermetallic Phases on Corrosion Behavior and Mechanical Properties of Duplex Stainless Steel and Super-Duplex Stainless Steel. *Advances in Science and Technology Research Journal*, 9(27):87–105, 2015.

[4] J. R. Davis. *Stainless steels*. First edition, 1994.

[5] G. Lacombe, P., Baroux, B., Beranger. *Stainless steels*. First edition, 1993.

[6] M. Haugan, E. B., Johnsen, R., Ianuzzi, M., Næss. Effect of Tungsten on Pitting and Crevice Corrosion of Type 25Cr Super Duplex Stainless Steel. *NACE International*, pages 1–10, 2016.

[7] NORSOK M-001 Materials selection. 2002.

[8] NORSOK M-630 Material data sheets and element data sheets for piping. 2010.

[9] Jan Ketil Solberg. *Teknologiske metaller og legeringer*. 2014.

[10] George E. Dieter. *Mechanical metallurgy*. 1988.

[11] David G. Callister, William D., Rethwisch. *Materials Science and Engineering*. 2011.

[12] A. John Sedriks. *Corrosion of stainless steels*. Second edition, 1996.

[13] L. Colombier. *Molybdenum in Stainless Steels and Alloys*. 1967.

[14] Hua Tan, Yiming Jiang, Bo Deng, Tao Sun, Juliang Xu, and Jin Li. Effect of annealing temperature on the pitting corrosion resistance of super duplex stainless steel UNS S32750. *Materials Characterization*, 60(9):1049–1054, 2009.

[15] Bo Deng, Zhiyu Wang, Yiming Jiang, Tao Sun, Juliang Xu, and Jin Li. Effect of thermal cycles on the corrosion and mechanical properties of UNS S31803 duplex stainless steel. *Corrosion Science*, 51(12):2969–2975, 2009.

[16] Hae-ji Park and Hae-woo Lee. Effect of Alloyed Mo and W on The Corrosion Characteristics of Super Duplex Stainless Steel Weld. *Int. J. Electrochem. Sci.*, 9:6687–6698, 2014.

[17] G. Lothongkum, P. Wongpanya, S. Morito, T. Furuhara, and T. Maki. Effect of nitrogen on corrosion behavior of 28Cr-7Ni duplex and microduplex stainless steels in air-saturated 3.5 wt% NaCl solution. *Corrosion Science*, 48(1):137–153, 2006.

[18] H. Hänninen, J. Romu, R. Ilola, J. Tervo, and A. Laitinen. Effects of processing and manufacturing of high nitrogen-containing stainless steels on their mechanical, corrosion and wear properties. *Journal of Materials Processing Technology*, 117(3):424–430, 2001.

[19] Henrik Sieurin and Rolf Sandström. Sigma phase precipitation in duplex stainless steel 2205. *Materials Science and Engineering A*, 444(1-2):271–276, 2007.

[20] R. Cervo, P. Ferro, and A. Tiziani. Annealing temperature effects on super duplex stainless steel UNS s32750 welded joints. I: Microstructure and partitioning of elements. *Journal of Materials Science*, 45(16):4369–4377, 2010.

[21] Pierre-Jean Cunat. *Working with Stainless Steel.* 1998.

[22] J. O. Nilsson, T. Huhtala, P. Jonsson, L. Karlsson, and a. Wilson. Structural stability of super duplex stainless weld metals and its dependence on tungsten and copper. *Metallurgical and Materials Transactions A*, 27:2196–2208, 1996.

[23] Seul-kee Kim, Ki-yeob Kang, Myung-soo Kim, and Jae-myung Lee. Low-Temperature Mechanical Behavior of Super Duplex Stainless Steel with Sigma Precipitation. pages 1732–1745, 2015.

[24] B. Deng, Y. M. Jiang, J. Gao, and J. Li. Effect of annealing treatment on microstructure evolution and the associated corrosion behavior of a super-duplex stainless steel. *Journal of Alloys and Compounds*, 493(1-2):461–464, 2010.

[25] Norsok Standard M601 Welding and inspection of piping. 2004.

[26] Hosni M. Ezuber, A. El-Houd, and F. El-Shawesh. Effects of sigma phase precipitation on seawater pitting of duplex stainless steel. *Desalination*, 207(1-3):268–275, 2007.

[27] Michael Pohl, Oliver Storz, and Thomas Glogowski. Effect of intermetallic precipitations on the properties of duplex stainless steel. *Materials Characterization*, 58(1):65–71, 2007.

[28] Marcelo Martins and Luiz Carlos Casteletti. Sigma phase morphologies in cast and aged super duplex stainless steel. *Materials Characterization*, 60(8):792–795, 2009.

[29] Chi Shang Huang and Chia Chang Shih. Effects of nitrogen and high temperature aging on sigma phase precipitation of duplex stainless steel. *Materials Science and Engineering A*, 402(1-2):66–75, 2005.

[30] Henrik Sieurin and Rolf Sandström. Austenite reformation in the heat-affected zone of duplex stainless steel 2205. *Materials Science and Engineering A*, 418(1-2):250–256, 2006.

[31] D. M. Escriba, E. Materna-Morris, R. L. Plaut, and A. F. Padilha. Chi-phase precipitation in a duplex stainless steel. *Materials Characterization*, 60(11):1214–1219, 2009.

[32] Joanna Michalska and Maria Sozaska. Qualitative and quantitative analysis of σ and χ phases in 2205 duplex stainless steel. *Materials Characterization*, 56(4-5 SPEC. ISS.):355–362, 2006.

[33] Darlene Yuko Kobayashi and Stephan Wolynec. Evaluation of the low corrosion resistant phase formed during the sigma phase precipitation in duplex stainless steels. *Materials Research*, 2(4):239–247, 1999.

[34] Niklas Petterson. Precipitation of chromium nitrides in the super duplex stainless steel 2507. *Swerea*, page 26, 2015.

[35] a J Ramirez, J. C. Lippold, and S. D. Brandi. The relationship between chromium nitride and secondary austenite precipitation in duplex stainless steels. *Metallurgical and Materials Transactions A*, 34(8):1575–1597, 2003.

[36] Statoil. Significance of chromium nitride precipitates in duplex stainless steels. 2015.

[37] Sandvik. Super duplex stainless steel - Influence of nitrides on corrosion initiation of super duplex stainless steel 2507.

[38] J. K. Sahu, U. Krupp, R. N. Ghosh, and H. J. Christ. Effect of 475 C embrittlement on the mechanical properties of duplex stainless steel. *Materials Science and Engineering A*, 508(1-2):1–14, 2009.

[39] Kemal Nisancioglu. *Corrosion basics and engineering.*

[40] James D. R. Talbot, David E. J., Talbot. *Corroion science and technology.* Second edi edition, 2007.

[41] Herbert H. Revie, R. Winston, Uhlig. *Corrosion and corrosion control: An introduction to corrosion science and Engineering.* Fourth edi edition, 2008.

[42] Philippe M. *Corrosion Mechanisms in Theory and Practice.* Second edi edition, 2002.

[43] Dominique Thierry, Charles Leballeur, and Nicolas Larché. Galvanic Series in Seawater as a Function of Temperature, Oxygen Content, and Chlorination. *NACE International Paper No. 7058*, pages 1–11, 2016.

[44] ISO 21457 Petroleum and natural gas industries - Materials for use in H2S - containing environments in oil and gas production. 2010.

[45] S. S M Tavares, J. M. Pardal, L. D. Lima, I. N. Bastos, A. M. Nascimento, and J. A. de Souza. Characterization of microstructure, chemical composition, corrosion resistance and toughness of a multipass weld joint of superduplex stainless steel UNS S32750. *Materials Characterization*, 58(7):610–616, 2007.

[46] Mariano Iannuzzi. Localized corrosion resistance of corrosion resistant alloys. *Robust Materialvalg i Oljeindustrien*, 2013.

[47] ASTM G61. Standard Test Method for Conducting Cyclic Potentiodynamic Polarization Measurements to Determine the Corrosion Susceptibility of Small Implant. 86(November):1–9, 2001.

[48] Mariano Iannuzzi, Næss, Monika, Haugan, Eirik B., Johnsen, Roy. Use of electrochemical techniques to determine localized corrosion resistance of 25-wt% Cr super duplex stainless steels: Effect of tungsten. 2015.

[49] Heejoon Hwang, Gwanyong Lee, Soonhyeok Jeon, and Yongsoo Park. Selective Dissolution Characteristics of 26Cr-7Ni-2.5Mo-3W Duplex Stainless Steel in H2SO4/HCl Mixed Solution. *Materials Transactions*, 50(5):1214–1218, 2009.

[50] M. Femenia, J. Pan, C. Leygraf, and P. Luukkonen. In situ study of selective dissolution of duplex stainless steel 2205 by electrochemical scanning tunnelling microscopy. *Corrosion Science*, 43(10):1939–1951, 2001.

[51] ISO 17864: Corrosion of Metals and Alloys - Determintation of the Critical Pitting Temperature Under Potentiostatic Control. 2005.

[52] ASTM G48. Standard test methods for pitting and crevice corrosion resistance of stainless steels and related alloys by use of ferric Chloride solution. *ASTM International*, 03(2009):1–10, 2003.

[53] Trond Haugen, Bård Espelid, and Peter Hummelgaard. Improved method for ASTM G48. 2004.

[54] C. J. Park, V. Shankar Rao, and H. S. Kwon. Effects of sigma phase on the initiation and propagation of pitting corrosion of duplex stainless steel. *Corrosion*, 61(1):76–83, 2005.

[55] T Mathiesen and J V Hansen. Consequences of sigma phase on pitting corrosion resistance of duplex stainless steel. *8th Duplex Stainless Steels conference*, (October), 2010.

[56] Marcelo Martins and Luiz Carlos Casteletti. Microstructural characteristics and corrosion behavior of a super duplex stainless steel casting. *Materials Characterization*, 60(2):150–155, 2009.

[57] Soon Hyeok Jeon, Soon Tae Kim, In Sung Lee, Ji Soo Kim, Kwang Tae Kim, and Yong Soo Park. Effects of W substitution on the precipitation of secondary phases and the associated pitting corrosion in hyper duplex stainless steels. *Journal of Alloys and Compounds*, 544:166–172, 2012.

[58] G.H. Aylward. *SI chemical data*. 6th editio edition, 2008.

Appendix A

Material Data Sheet

016F-No.6734

May, 2016
NIPPON STEEL & SUMITOMO METAL CORPORATION
AMAGASAKI WORKS

Description of DP3W test sample

1. Description of test sample

Table 1 Description of test sample

Material	UNS No.	Size
DP3W	S39274	219.3mmOD x 30.0mmWT x 150mmL x 3pcs.

Table 2 Chemical composition (mass%)

	C	Si	Mn	P	S	Cu	Ni	Cr	Mo	W	N
Test sample	0.018	0.25	0.72	0.019	0.0002	0.47	6.3	24.9	3.1	2.08	0.29
S39274 Spec.	0.030 Max.	0.8 Max.	1.0 Max.	0.030 Max.	0.010 Max.	0.20 -0.80	6.0 -8.0	24.0 -26.0	2.5 -3.5	1.50 -2.50	0.24 -0.32

2. Result of test sample

(1) Mechanical Property

Table 3 Tensile properties

Position	Yield strength (MPa)	Tensile strength (MPa)	Elongation (%)
End	577	802	42
Mid	607	808	41
S39274 Spec.	550 Min.	800 Min.	15 Min.

Table 4 Hardness (HRC)

Position	Hardness (HRC)			
	1	2	3	Ave.
End	23.5	23.1	23.7	23.4
Mid	24.6	23.9	23.8	24.1
S39274 Spec.	-	-	-	Max.30

This document contains information proprietary to NSSMC and shall not be disclosed without written authorization of NSSMC .

NIPPON STEEL & SUMITOMO METAL CORPORATION

© 2016 NIPPON STEEL & SUMITOMO METAL CORPORATION All Rights Reserved

The microstructure is free from detrimental intermetallic phases and precipitations.

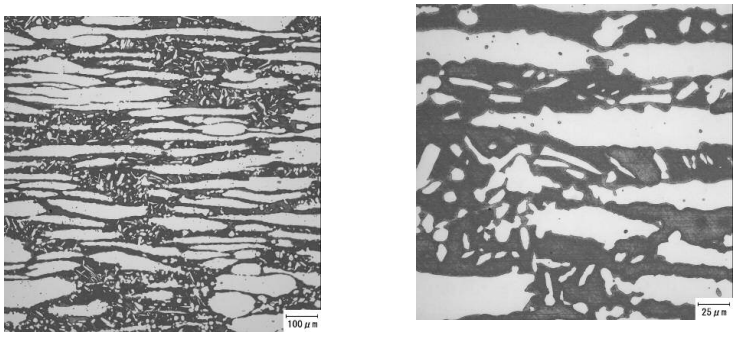

(×100) (×400)

End portion

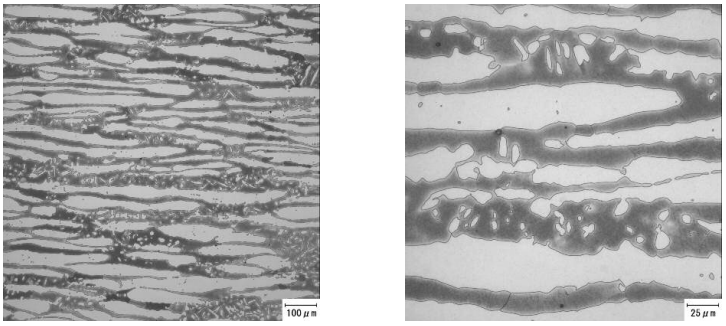

(×100) (×400)

Mid-length portion

Figure 2 Microstructure of test sample (Mid-thickness, , Etchant; 20% NaOH electrolyte)

Notes	・Technical information contained in this document describes only some representative properties or performance of products and does not necessarily mean assured values. Further, as such information may be subject to change without notice, you are requested to ask the latest information when you order a product. ・We do not take the responsibility for any damage caused by erroneous or misappropriate use of information in this document. ・No part of this document can be reproduced or copied without permission.

This document contains information proprietary to NSSMC and shall not be disclosed without written authorization of NSSMC .

NIPPON STEEL & SUMITOMO METAL CORPORATION

© 2016 NIPPON STEEL & SUMITOMO METAL CORPORATION All Rights Reserved

Appendix B

Critical pitting temperature measurements

CPT was determined as described in Section 3.3.2 based on a modified method of ASTM G48. Figure B.2a - B.3d present OCP and temperature measurements of sample 1.1 - 1.2 and 1.11 - 1.26 in the test matrix in Table 3.4.

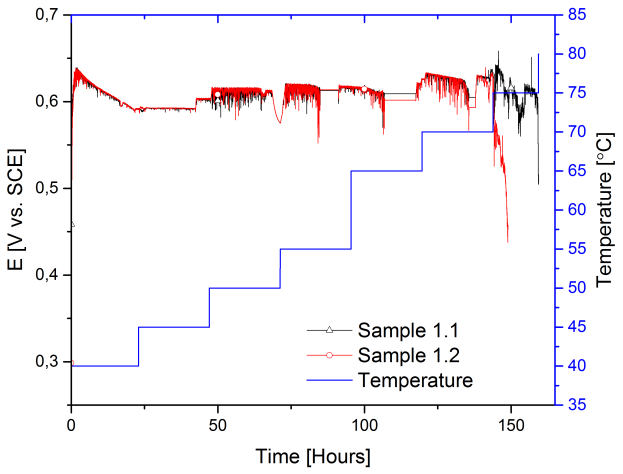

Figure B.1: CPT measurement of sample 1.1 - 1.2.

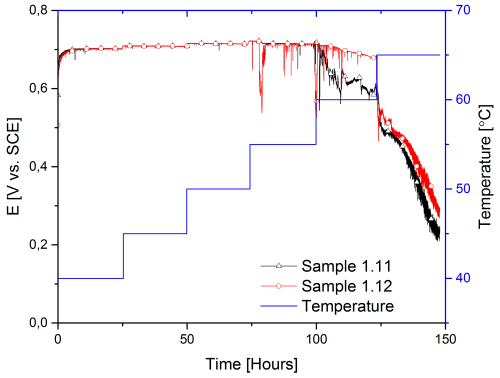

(a) Sample 1.11 and 1.12.

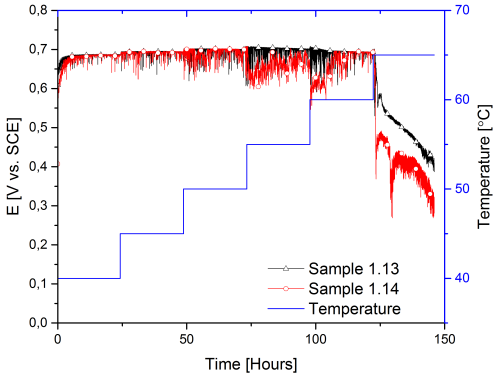

(b) Sample 1.13 and 1.14.

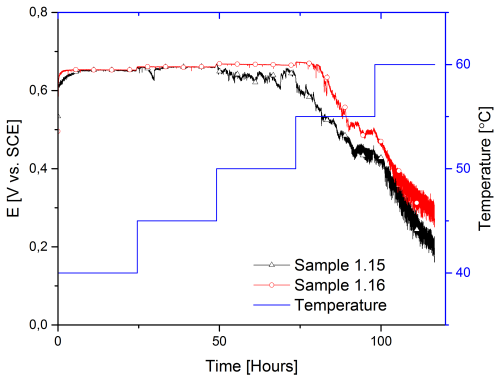

(c) Sample 1.15 and 1.16.

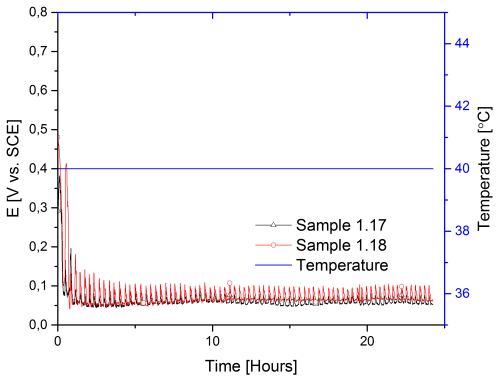

(d) Sample 1.17 and 1.18.

Figure B.2: CPT measurements of sample 1.11 - 1.18.

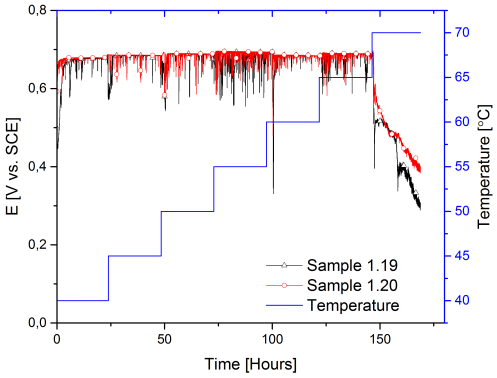

(a) Sample 1.19 and 1.20.

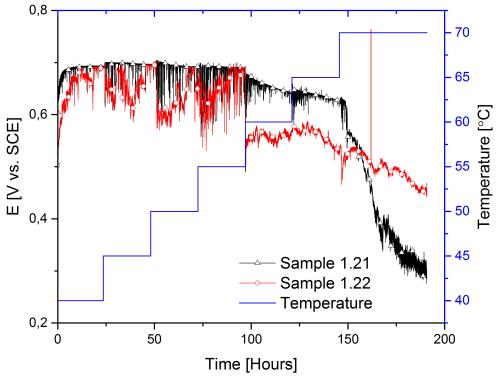

(b) Sample 1.21 and 1.22.

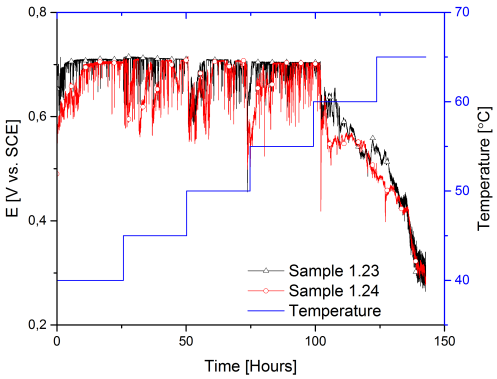

(c) Sample 1.23 and 1.24.

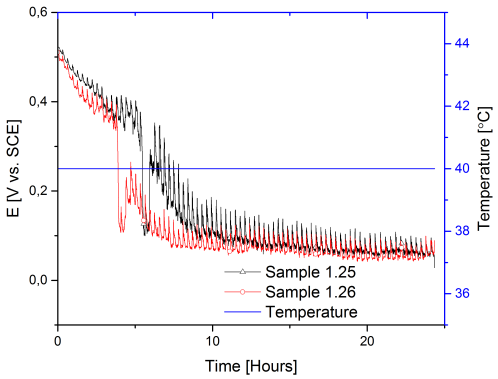

(d) Sample 1.25 and 1.26.

Figure B.3: CPT measurements of sample 1.19 - 1.26.

Appendix B. Critical pitting temperature measurements

Appendix C

Surface characterization after critical pitting temperature measurements

Surface characterization by 3D OM with a magnification of 2,5X of sample 1.3 - 1.8, 1.9-1.11 and 1.18 - 1.26, in the test matrix in Table 3.4, are shown in Figure C.1 and C.2.

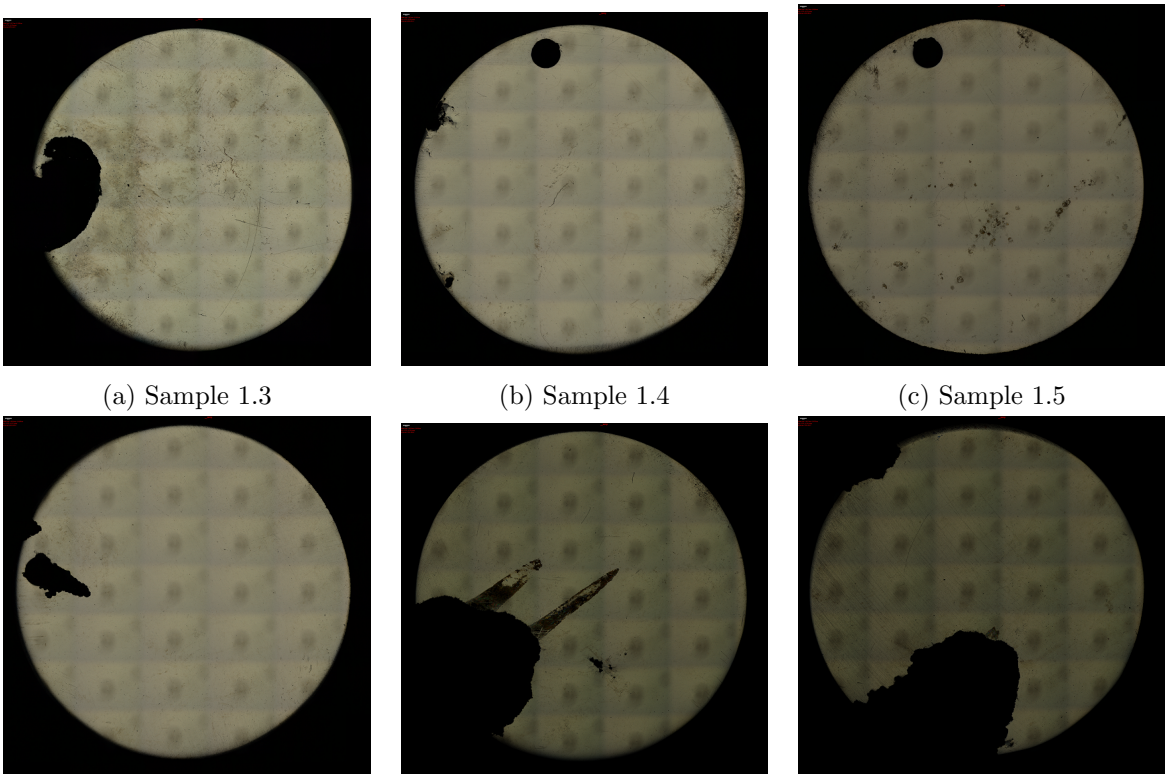

(a) Sample 1.3 (b) Sample 1.4 (c) Sample 1.5

(d) Sample 1.6 (e) Sample 1.7 (f) Sample 1.8

Figure C.1: Surface characterization by 3D OM, with a magnification of 2,5X.

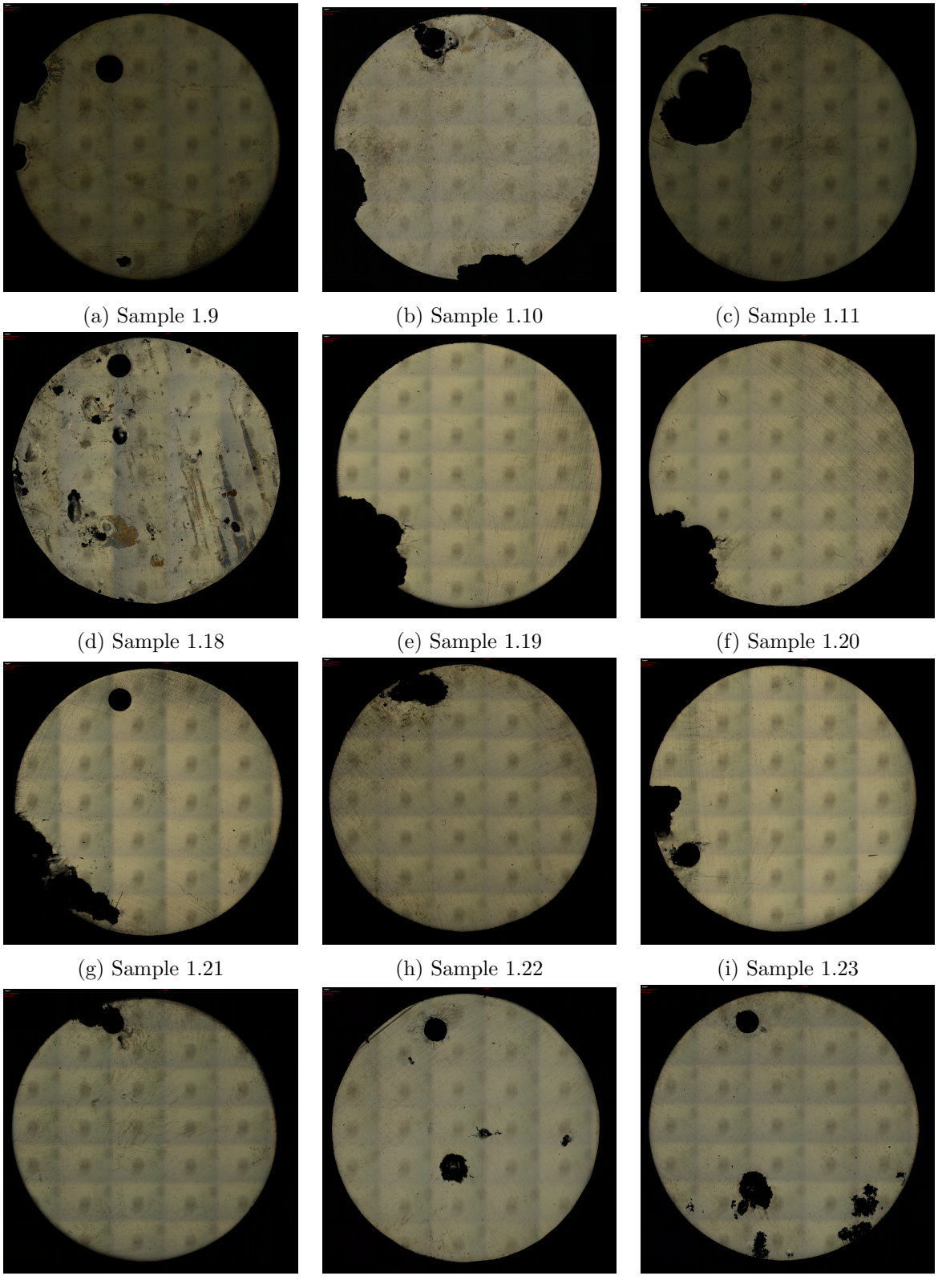

(a) Sample 1.9 (b) Sample 1.10 (c) Sample 1.11

(d) Sample 1.18 (e) Sample 1.19 (f) Sample 1.20

(g) Sample 1.21 (h) Sample 1.22 (i) Sample 1.23

(j) Sample 1.24 (k) Sample 1.25 (l) Sample 1.26

Figure C.2: Surface characterization by 3D optical microscope, with a magnification of 2,5X.

Appendix D

Open circuit potential measurements

OCP was measured prior to anodic cyclic potentiodynamic polarization. The OCP measurements for sample 2.1 - 1.8, 2.9 - 2.20 and 2.21 - 2.36 from the test matrix in Table 3.6, are shown in Figure D.1 - D.4.

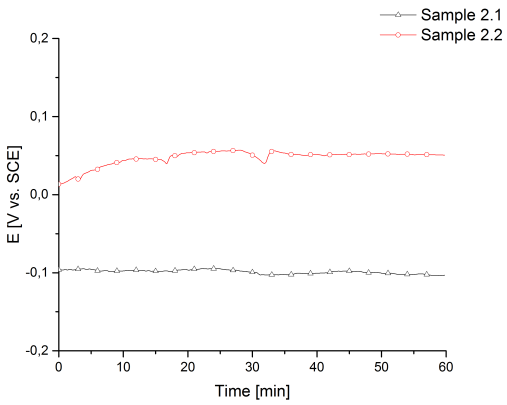

(a) Sample 2.1 and 2.2

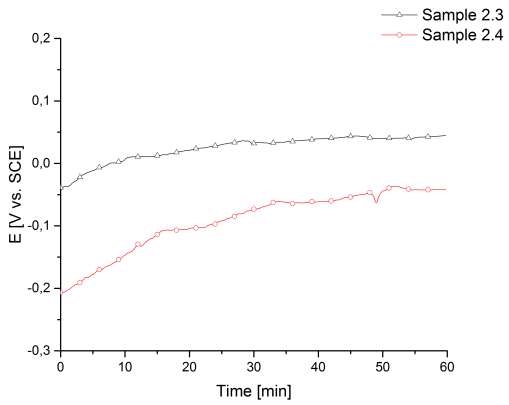

(b) Sample 2.3 and 2.4

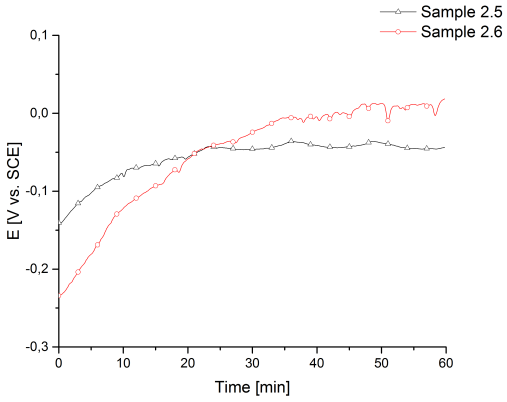

(c) Sample 2.5 and 2.6

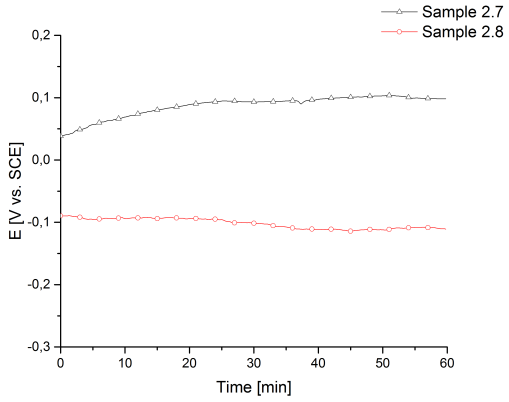

(d) Sample 2.7 and 2.8

Figure D.1: OCP of sample 2.1 - 2.8 measured prior to anodic potentiodynamic polarization.

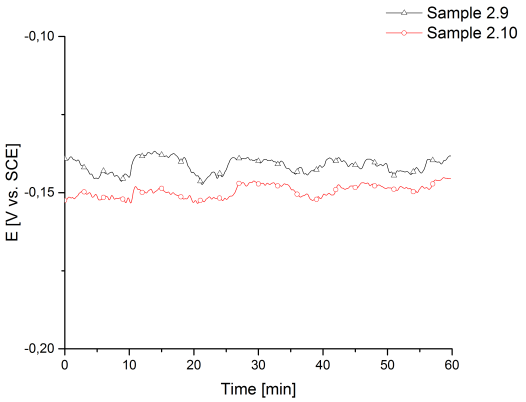

(a) Sample 2.9 and 2.10

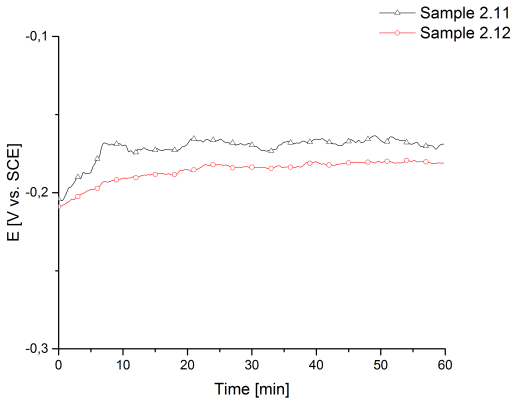

(b) Sample 2.11 and 2.12

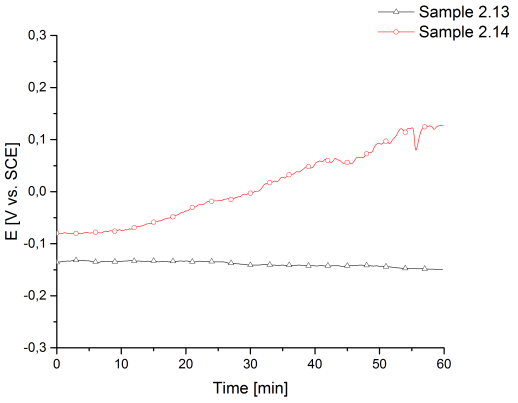

(c) Sample 2.13 and 2.14

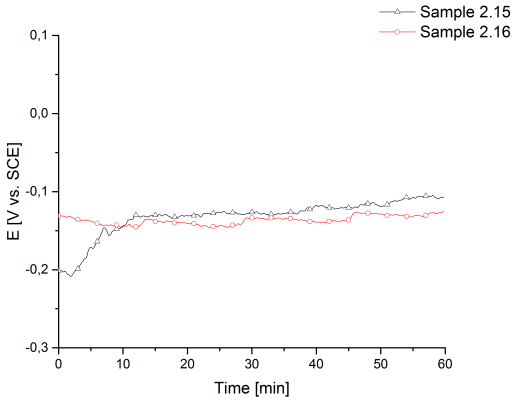

(d) Sample 2.15 and 2.16

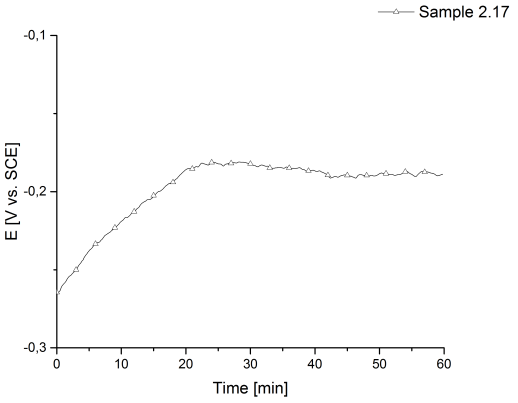

(e) Sample 2.17

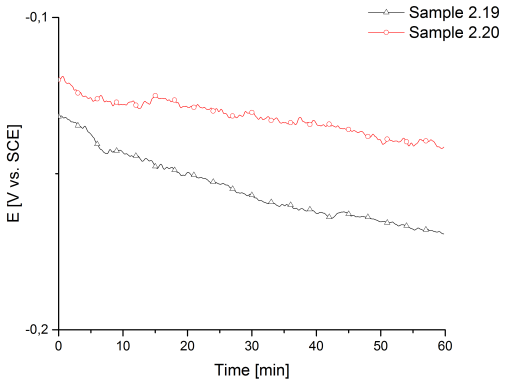

(f) Sample 2.19 and 2.20

Figure D.2: OCP of sample 2.9 - 2.20 measured prior to anodic potentiodynamic polarization.

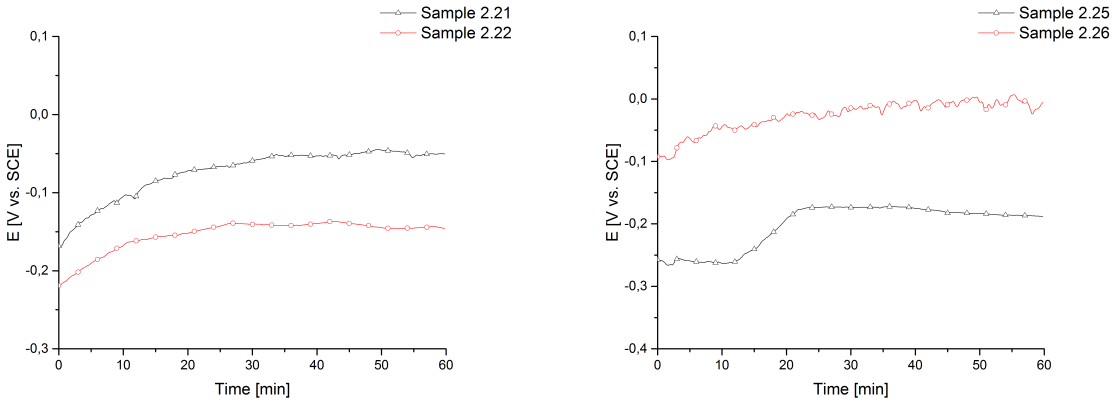

(a) Sample 2.21 and 2.22

(b) Sample 2.25 and 2.26

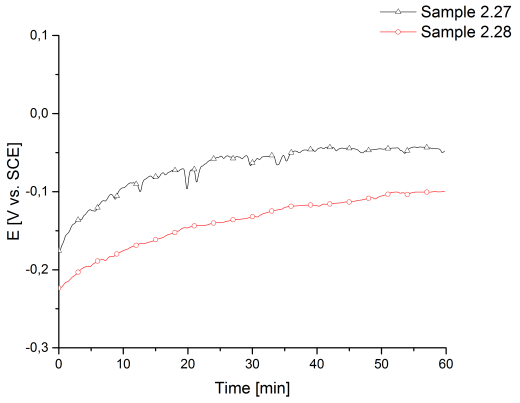

(c) Sample 2.27 and 2.28

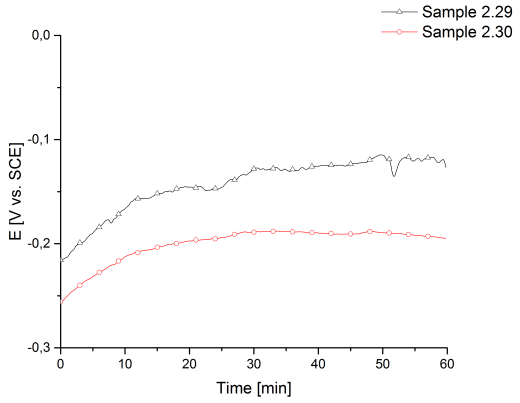

(d) Sample 2.29 and 2.30

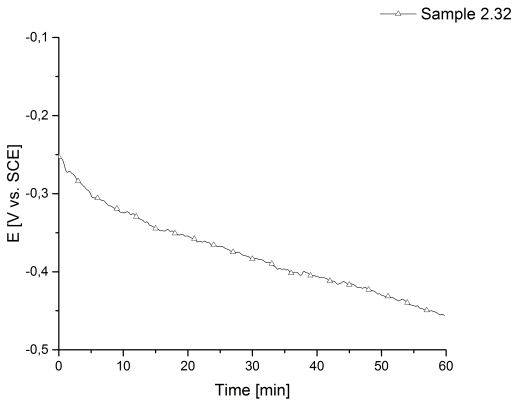

(e) Sample 2.32

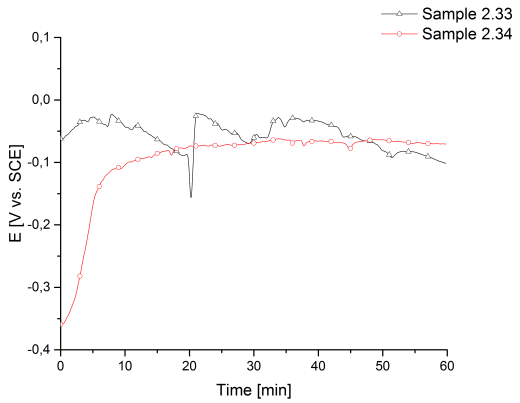

(f) Sample 2.33 and 2.34

Figure D.3: OCP of sample 2.21 - 2.34 measured prior to anodic potentiodynamic polarization.

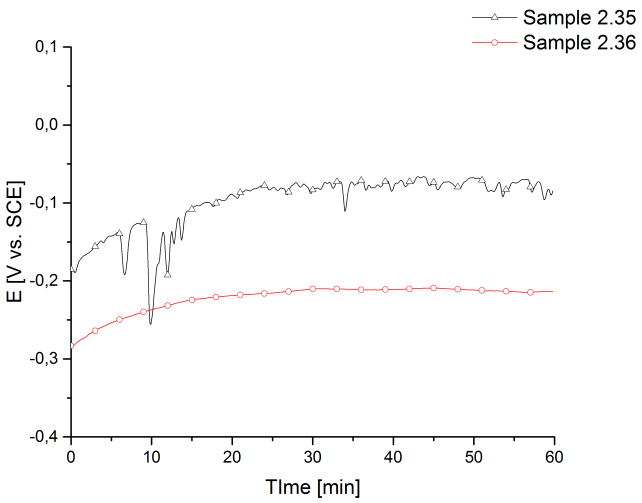

Figure D.4: OCP of sample 2.35 and 2.36 measured prior to anodic potentiodynamic polarization.

Appendix E

Anodic potentiodynamic polarization curves

Anodic CPP curves of sample 2.1 - 2.8 and 2.15 - 2.30, from the test matrix in Table 3.6, are given in Figure E.1 - E.12.

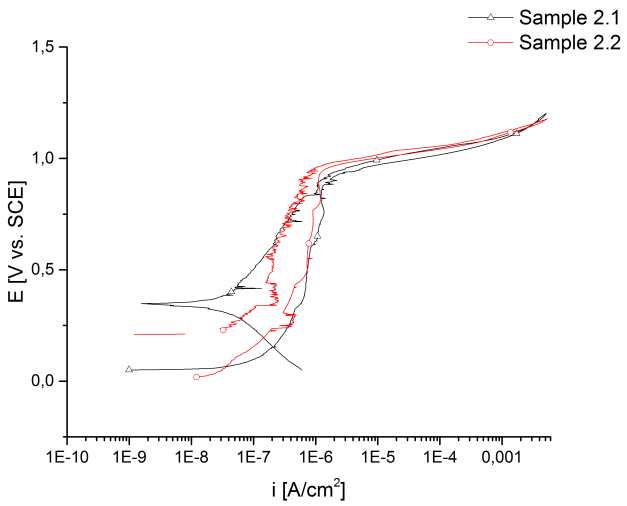

Figure E.1: Anodic CPP curves of sample 2.1 and 2.1, solution annealed at 1110°C for 15 minutes. The curves were recorded with an electrolyte temperature of 40 °C.

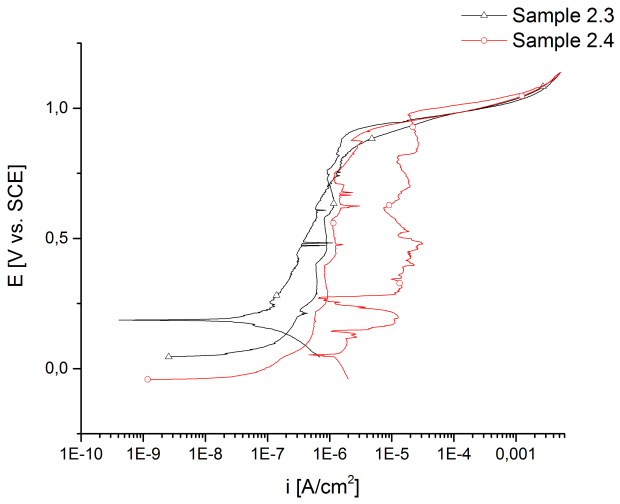

Figure E.2: Anodic CPP curves of sample 2.3 and 2.4, solution annealed at 1110°C for 15 minutes. The curves were recorded with an electrolyte temperature of 60 °C.

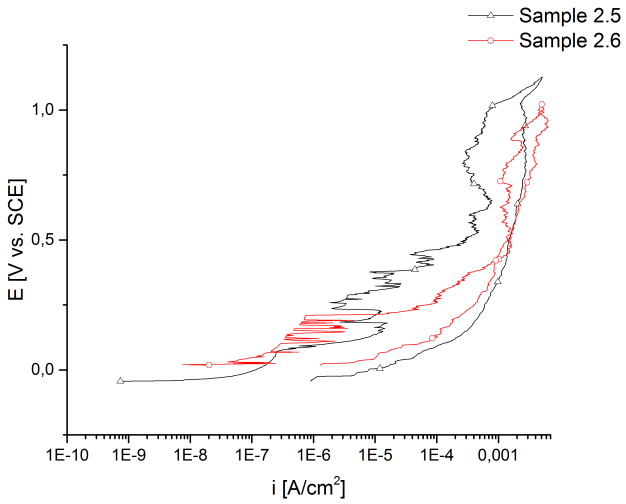

Figure E.3: Anodic CPP curves of sample 2.5 and 2.6, solution annealed at 1110°C for 15 minutes. The curves were recorded with an electrolyte temperature of 80 °C.

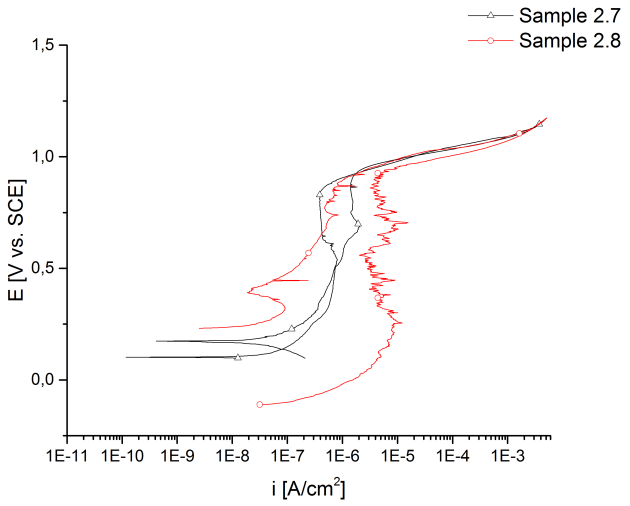

Figure E.4: Anodic CPP curves of sample 2.7 and 2.8, heat treated at 870°C for 1 minute. The curves were recorded with an electrolyte temperature of 40 °C.

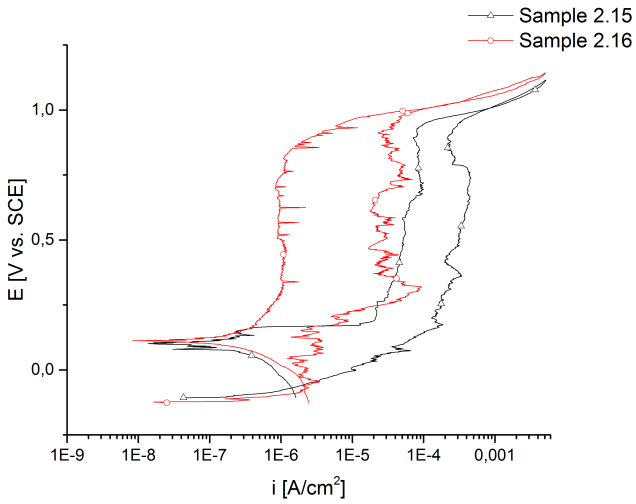

Figure E.5: Anodic CPP curves of sample 2.15 and 2.16, heat treated at 870°C for 1,5 minutes. The curves were recorded with an electrolyte temperature of 60 °C.

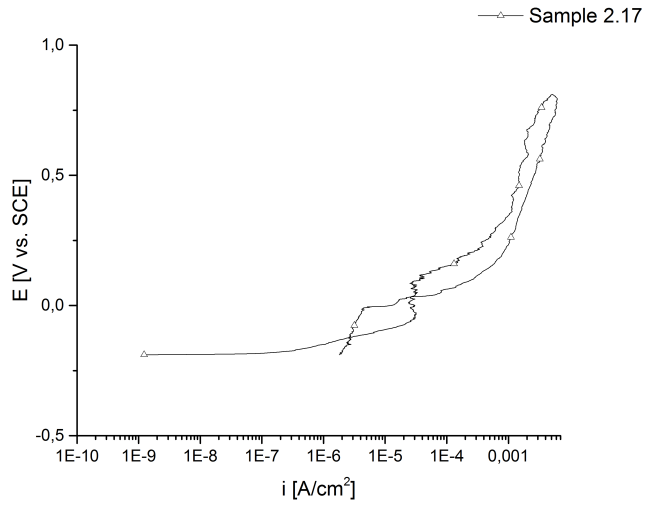

Figure E.6: Anodic CPP curves of sample 2.17, heat treated at 870°C for 1,5 minutes. The curves were recorded with an electrolyte temperature of 80 °C.

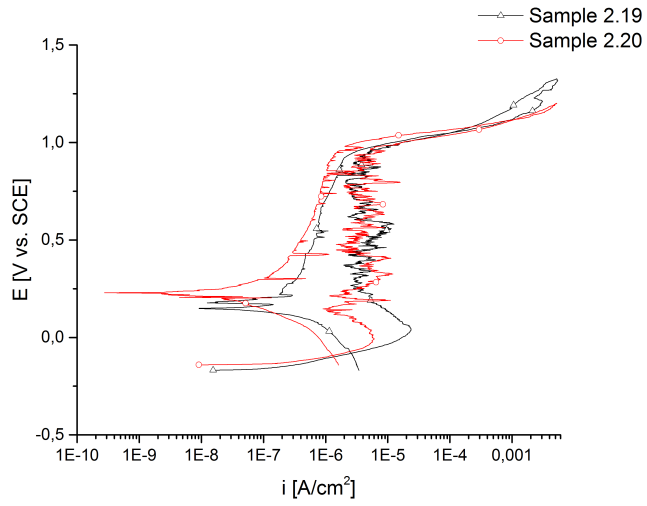

Figure E.7: Anodic CPP curves of sample 2.19 and 2.20, heat treated at 870°C for 2 minutes. The curves were recorded with an electrolyte temperature of 40 °C.

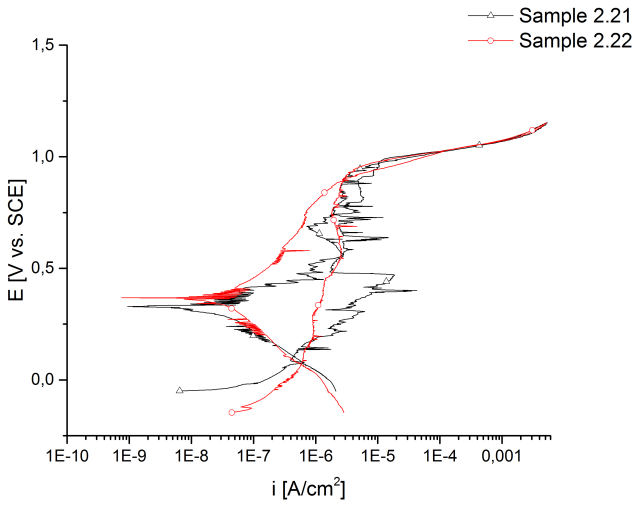

Figure E.8: Anodic CPP curves of sample 2.21 and 2.22, heat treated at 870°C for 2 minutes. The curves were recorded with an electrolyte temperature of 60 °C.

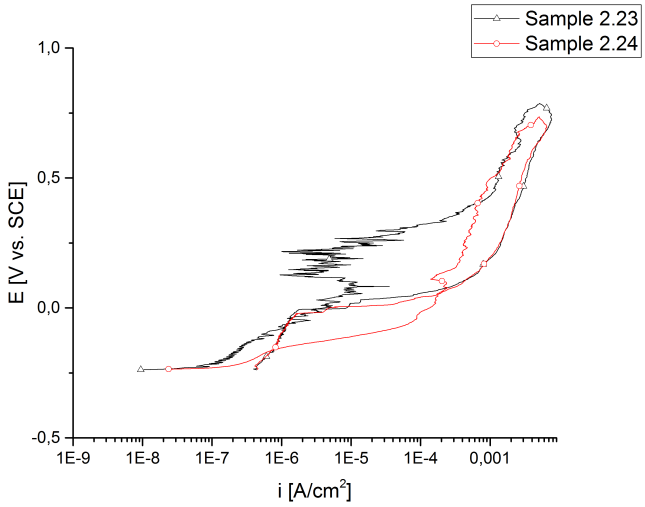

Figure E.9: Anodic CPP curves of sample 2.23 and 2.24, heat treated at 870°C for 2 minutes. The curves were recorded with an electrolyte temperature of 80 °C.

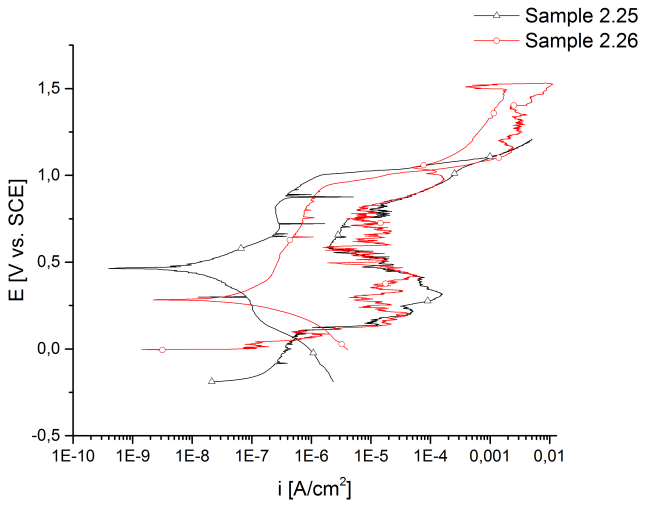

Figure E.10: Anodic CPP curves of sample 2.25 and 2.26, heat treated at 820°C for 4 minutes. The curves were recorded with an electrolyte temperature of 40 °C.

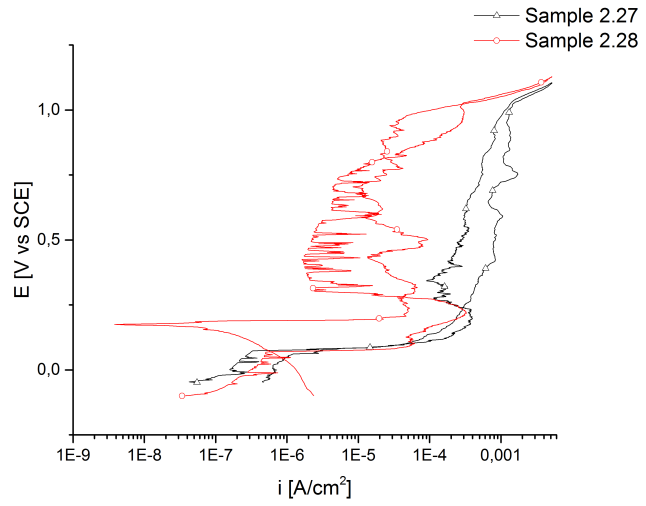

Figure E.11: Anodic CPP curves of sample 2.27 and 2.28, heat treated at 820°C for 4 minutes. The curves were recorded with an electrolyte temperature of 60 °C.

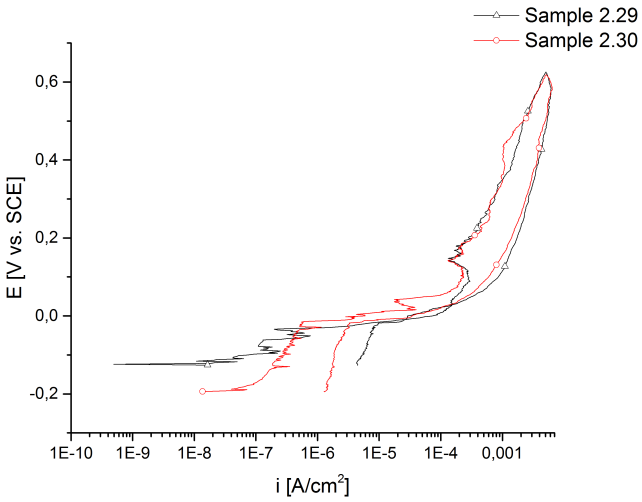

Figure E.12: Anodic CPP curves of sample 2.29 and 2.30, heat treated at 820°C for 4 minutes. The curves were recorded with an electrolyte temperature of 80 °C.

Appendix F

Surface characterization after anodic potentiodynamic polarization

Depth and width measurements of three pits on sample 2.5, 2.29 and 2.30, from the test matrix in Table 3.6, are given in Figure F.1 - F.17.

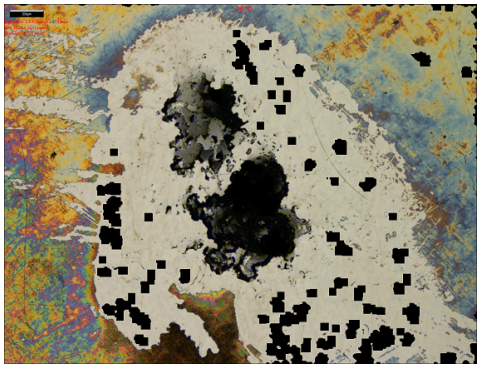

Figure F.1: Surface characterization of two pits on sample 2.5 by 3D OM after anodic CPP, with a magnification of 5X.

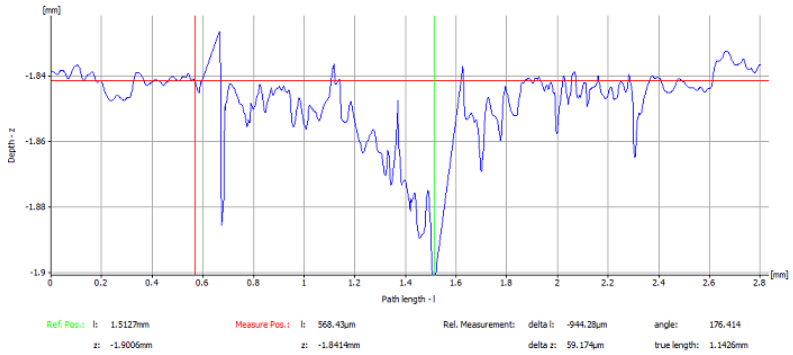

Figure F.2: Depth and width of the lower pit on sample 2.5 in Figure F.1.

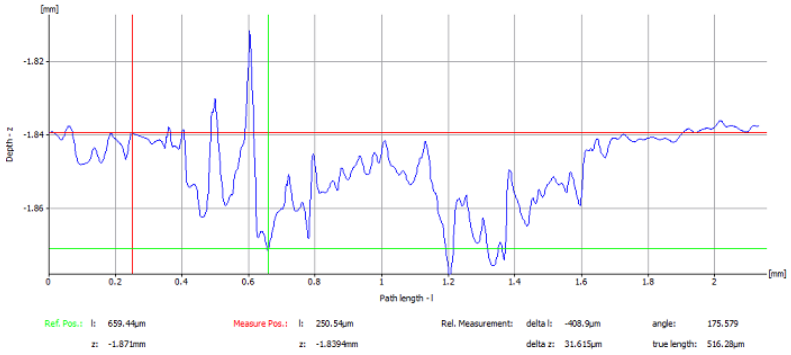

Figure F.3: Depth and width of the upper pit on sample 2.5 in Figure F.1.

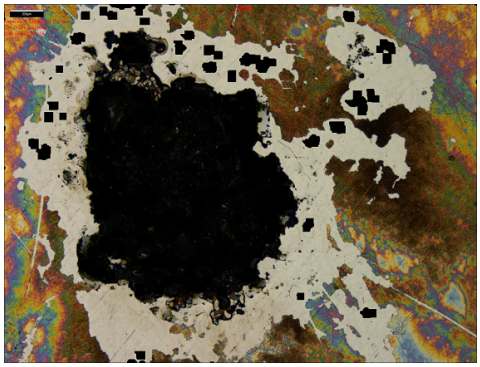

Figure F.4: Surface characterization of a pit on sample 2.5 by 3D OM after anodic CPP, with a magnification of 5X.

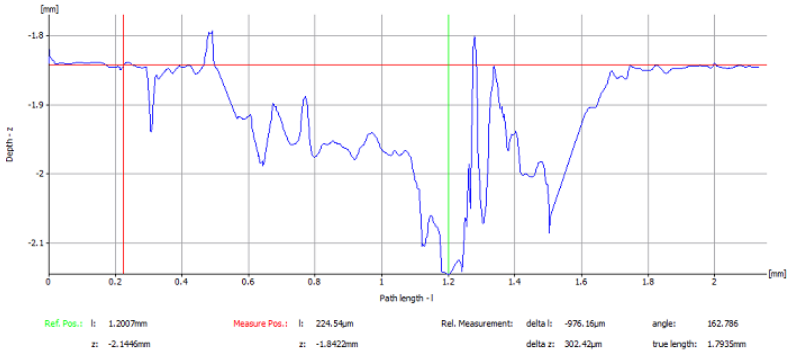

Figure F.5: Depth and width of the pit on sample 2.5 in Figure F.4.

Figure F.6: Surface characterization of pit on sample 2.29 by 3D OM after anodic CPP, with a magnification of 20X.

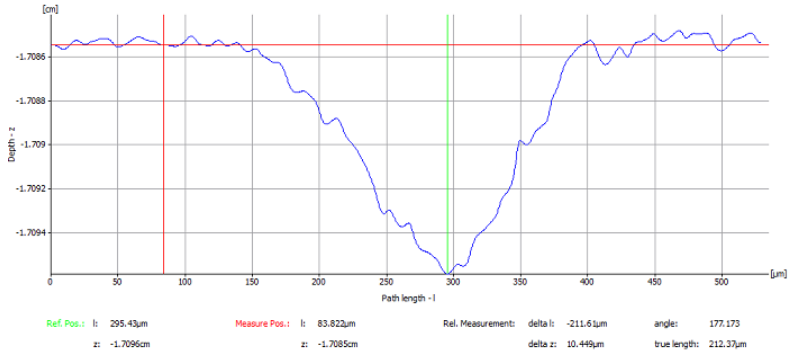

Figure F.7: Depth and width of the pit on sample 2.29 in Figure F.6.

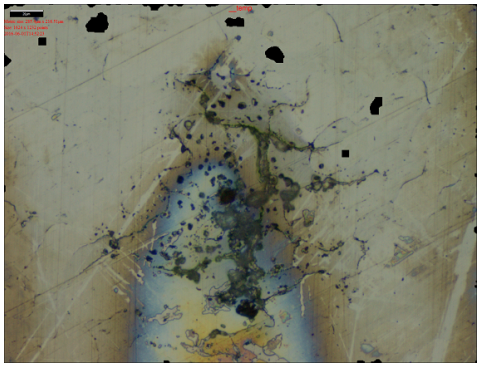

Figure F.8: Surface characterization of a pit on sample 2.29 by 3D OM after anodic CPP, with a magnification of 50X.

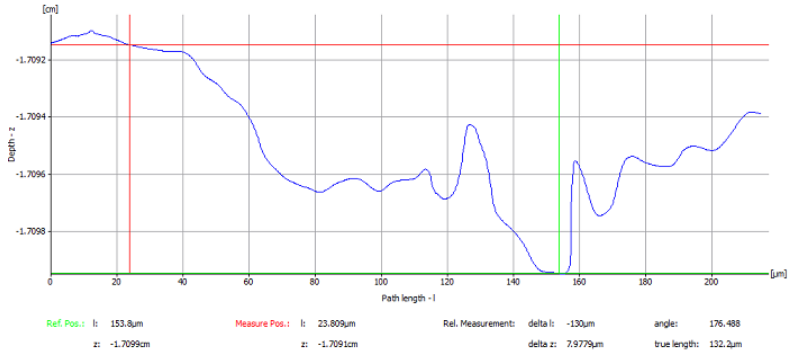

Figure F.9: Depth and width of the pit on sample 2.29 in Figure F.8.

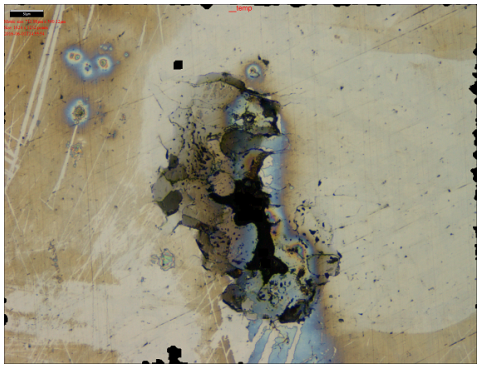

Figure F.10: Surface characterization of a pit on sample 2.29 by 3D OM after anodic CPP, with a magnification of 50X.

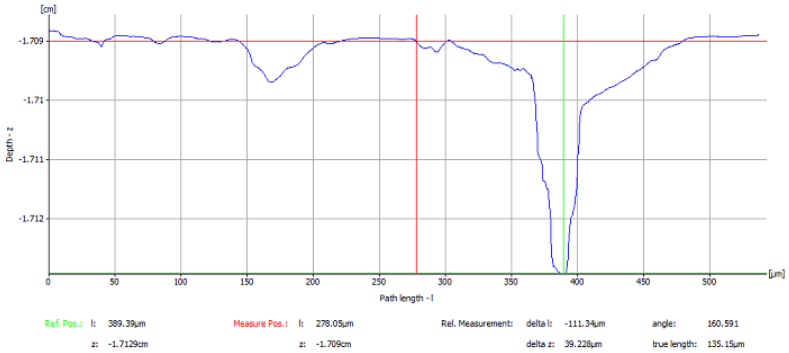

Figure F.11: Depth and width of the pit on sample 2.29 in Figure F.10.

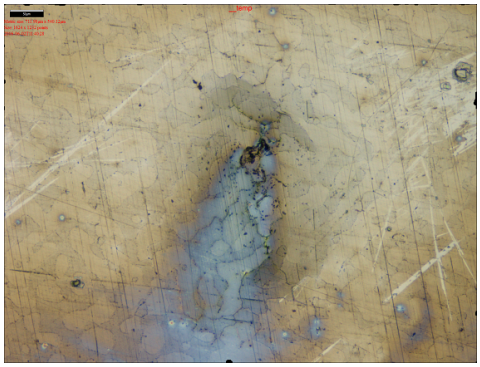

Figure F.12: Surface characterization of a pit on sample 2.35 by 3D OM after anodic CPP, with a magnification of 20X.

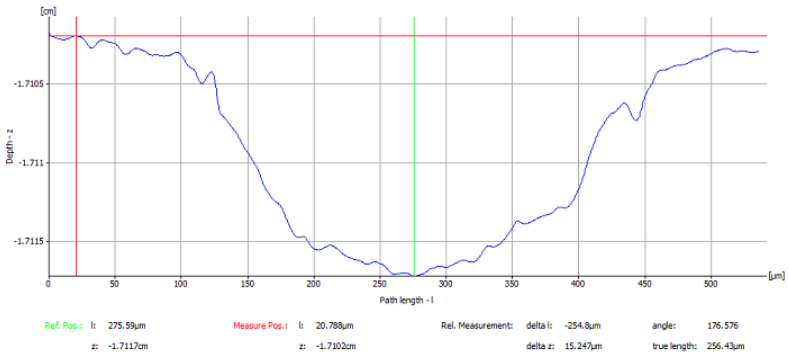

Figure F.13: Depth and width of the pit on sample 2.35 in Figure F.12.

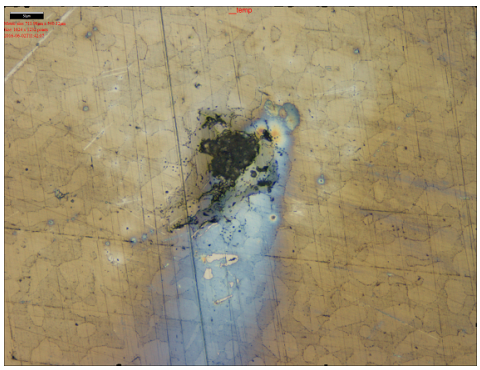

Figure F.14: Surface characterization of a pit on sample 2.35 by 3D OM after anodic CPP, with a magnification of 20X.

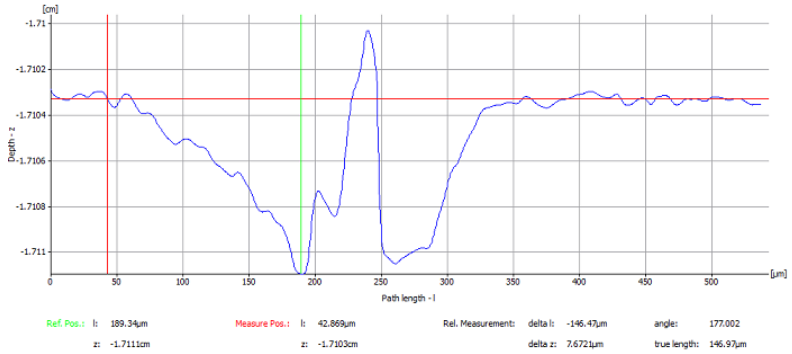

Figure F.15: Depth and width of the pit on sample 2.35 in Figure F.14.

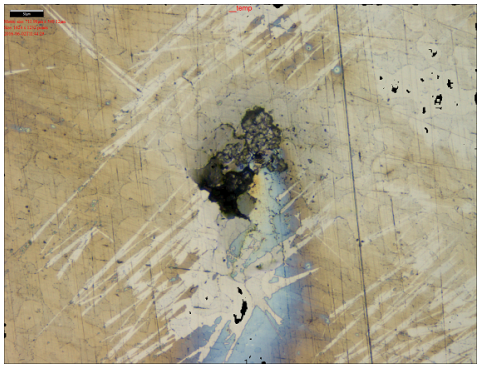

Figure F.16: Surface characterization of a pit on sample 2.35 by 3D OM after anodic CPP, with a magnification of 20X.

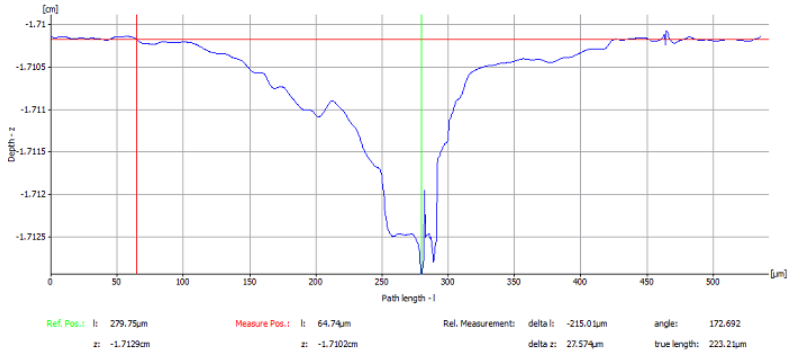

Figure F.17: Depth and width of the pit on sample 2.35 in Figure F.16.

Surface characterization by 3D OM, with a magnification of 2,5X, of sample 2.1 - 2.4, 2.6 - 2.11, 2.13 - 2.16, 2.19 - 2.22, 2.24 - 2.28, 2.30 - 2.34 and 2.36, in test matrix 3.6, are given in Figure F.18 - F.21.

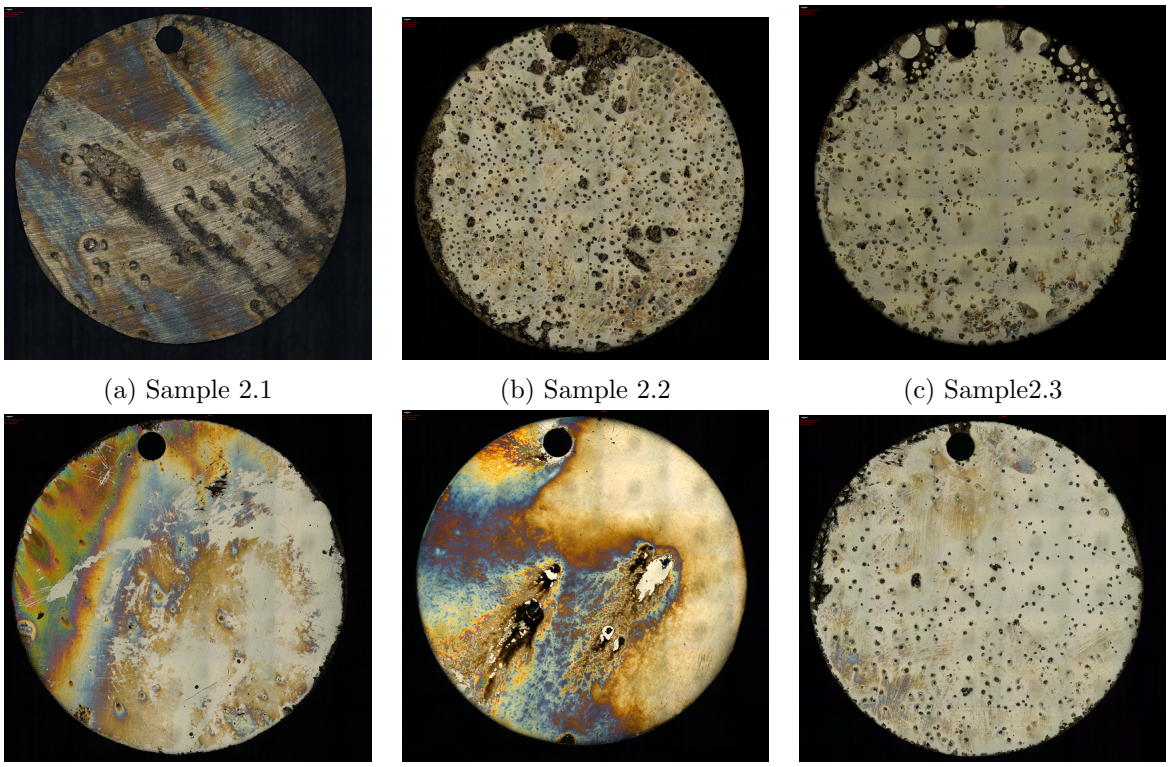

(a) Sample 2.1 (b) Sample 2.2 (c) Sample2.3

(d) Sample 2.4 (e) Sample 2.6 (f) Sample 2.7

Figure F.18: Surface characterization by 3D OM, with a magnification of 2,5X, of sample 2.1 - 2.4 and 2.6 - 2.7, after anodic CPP.

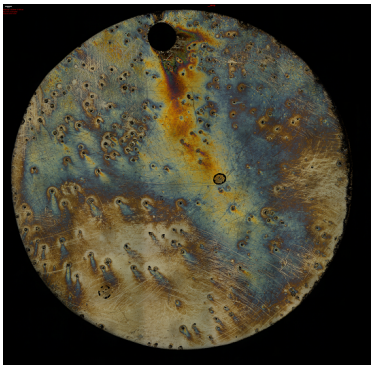

(a) Sample 2.8

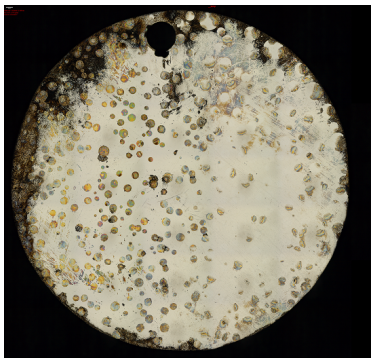

(b) Sample 2.9

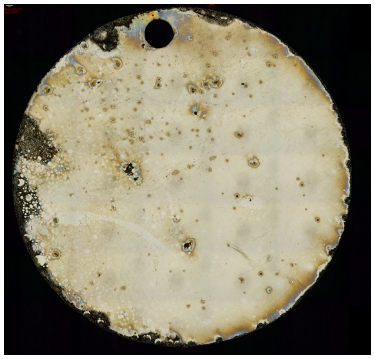

(c) Sample 2.10

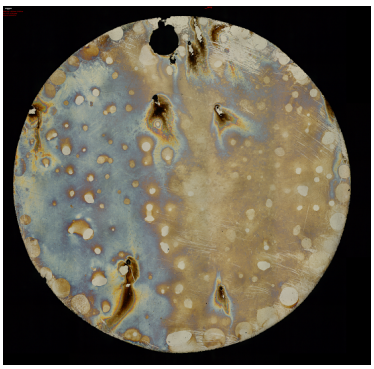

(d) Sample 2.11

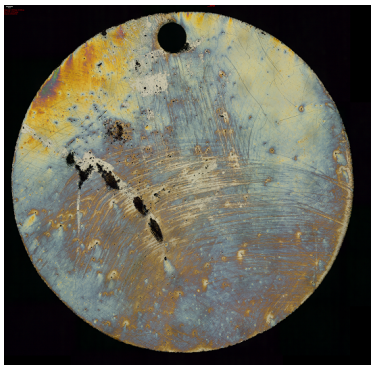

(e) Sample 2.13

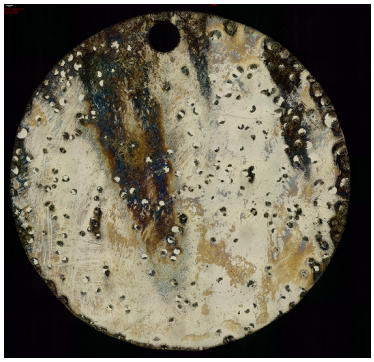

(f) Sample 2.14

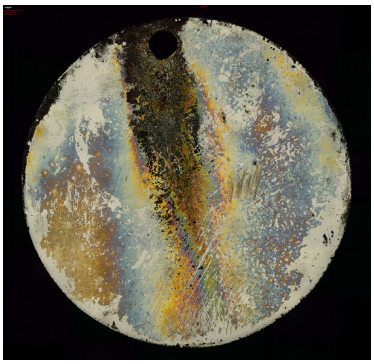

(g) Sample 2.15

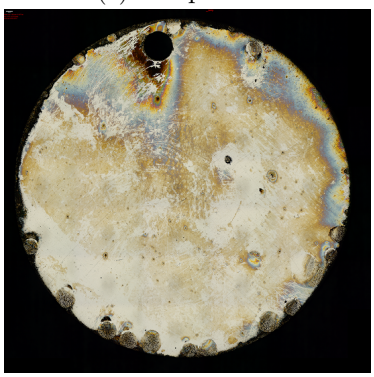

(h) Sample 2.16

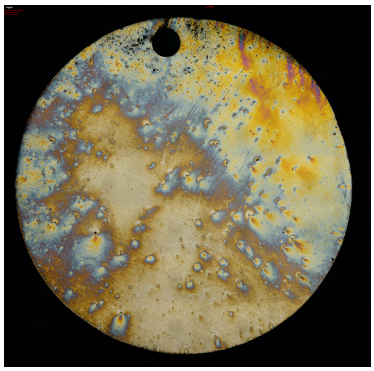

(i) Sample 2.19

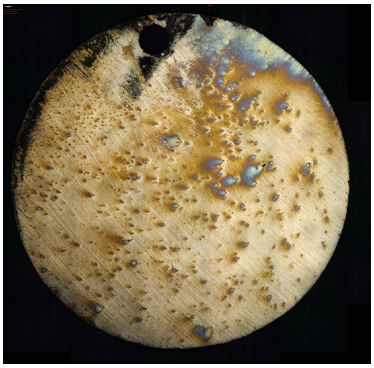

(j) Sample 2.20

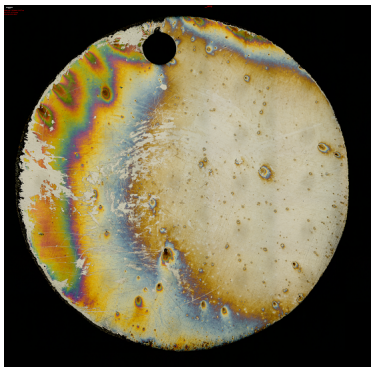

(k) Sample 2.21

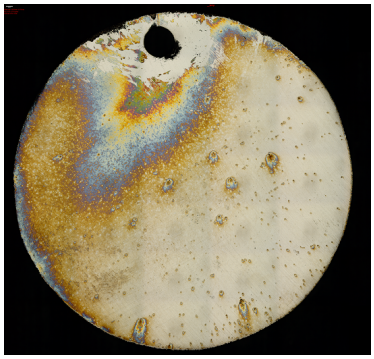

(l) Sample 2.22

Figure F.19: Surface characterization by 3D OM, with a magnification of 2,5X, after anodic CPP.

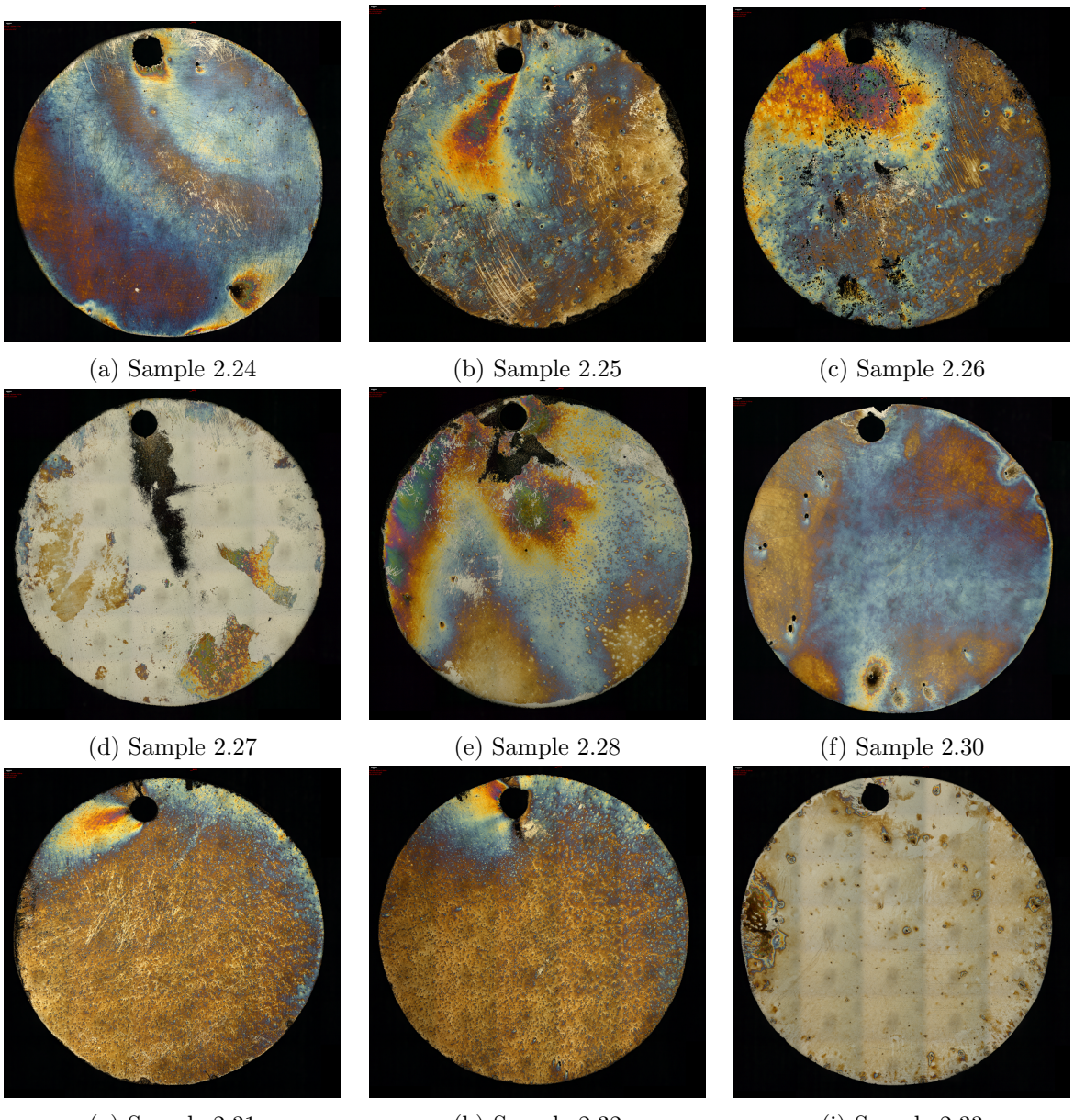

(a) Sample 2.24 (b) Sample 2.25 (c) Sample 2.26

(d) Sample 2.27 (e) Sample 2.28 (f) Sample 2.30

(g) Sample 2.31 (h) Sample 2.32 (i) Sample 2.33

Figure F.20: Surface characterization by 3D OM, with a magnificiation of 2,5X, after anodic CPP.

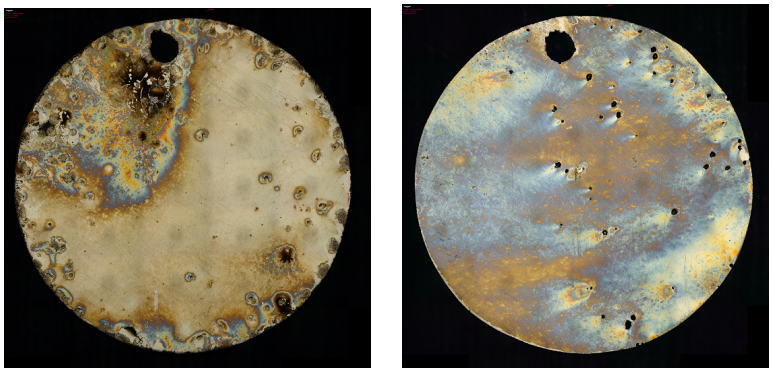

(a) Sample2.34 (b) Sample 2.36

Figure F.21: Surface characterization by 3D OM, with a magnification of 2,5X, after anodic CPP.